UNIVERSITY OF CALIFORNIA SAN DIEGO

Harnessing $FeCl_3$-PEO Photoreactions for Precision Photolithographic Patterning of Conductive PEDOT and Biocompatible PDMS

A dissertation submitted in partial satisfaction of the
requirements for the degree
Doctor of Philosophy

in

Electrical Engineering (Applied Physics)

by

Samuel J. Edmunds

Committee in charge:

Professor Darren Lipomi, Chair
Professor Tse Nga Ng, Co-Chair
Professor Yu-Hwa Lo
Professor Donald Sirbuly

2024

The dissertation of Samuel J. Edmunds is approved, and it is acceptable in quality and form for publication on microfilm and electronically.

University of California San Diego

2024

DEDICATION

To my family, Margaret, Jay, and Patrick: For supporting me wholeheartedly through this journey. Your unwavering belief and encouragement gave me strength when I needed it most. This work is as much yours as it is mine.

EPIGRAPH

An expert is a person who has found out by his own painful experience all the mistakes that one can make in a very narrow field.

—Niels Bohr

TABLE OF CONTENTS

LIST OF FIGURES

ACKNOWLEDGEMENTS

I would like to express my deepest gratitude to my advisor, Professor Darren Lipomi, who has supported me from the early years of my undergraduate studies through the five years of my Ph.D. His mentorship, encouragement, and guidance have been invaluable throughout this journey. I am incredibly grateful to my co-advisor, Professor Tse Nga Ng, for believing in my potential when others did not and for her unwavering support and insight.

I extend my heartfelt thanks to my undergraduate research assistants, Emerson Chin, Rafael Montalvo, Kristopher Ngo, Hannah Fishman, Marc Levy, Fiona Liang, and Sebastien Mallari. Your dedication, teamwork, and enthusiasm have enabled my work in countless ways, and I could not have asked for a better team. I also wish to thank all my lab colleagues and mentors who contributed to a collaborative and stimulating research environment that made this work possible.

Chapter 1 of this dissertation includes material as it appears in ”Photography-Inspired Patterned Vapor Phase Polymerization of Conductive PEDOT on Rigid and Stretchable Substrates,” published in ACS Materials Letters, 2024. This work was co-authored with Armando D. Urbina, Hannah E. Fishman, Yi Qie, Rafael A. Montalvo, Noel Sebastien D. Mallari, Marc N. Levy, Rachel Blau, Abdulhameed Abdal, Andrea M. Armani, Tse Nga Ng, Nathan A. Romero, and Darren J. Lipomi, and I was the primary investigator and author of this material.

Chapter 2 is submitted for publication in Advanced Materials as ”A Simple Method for Photopatterning Commercial PDMS Using an Off-the-Shelf Photodeactivated Hydrosilylation Inhibitor,” co-authored with Noel Sebastien D. Mallari, Qinyu Liang, Leah Sadr, Dhivya Pushpa Meganathan, Anum Tahir, Lisa Tang, Jacqueline Lampert, Marc Levy, Wade Shipley, Hannah E. Fishman, Tarek Rafeedi, Rafael A. Montalvo, Abdulhameed Abdal, Tse Nga Ng, Jinhye Bae, Andrea Tao, Nathan Romero, Zeinab Jahed, and Darren J. Lipomi. I was the primary investigator and author of this material.

VITA

2019	B. S. in Electrical Engineering, University of California San Diego
2021	M. S. in Electrical Engineering, University of California San Diego
2024	Ph. D. in Electrical Engineering, University of California San Diego

PUBLICATIONS

Samuel J. Edmunds, Armando D. Urbina, Hannah E. Fishman, Yi Qie, Rafael A. Montalvo, Noel Sebastien D. Mallari, Marc N. Levy, Rachel Blau, Abdulhameed Abdal, Andrea M. Armani, Tse Nga Ng, Nathan A. Romero, and Darren J. Lipomi "Photography-Inspired Patterned Vapor Phase Polymerization of Conductive PEDOT on Rigid and Stretchable Substrates", *ACS Materials Letters*, 6, 2738-2747, 2024.

Samuel J. Edmunds, Noel Sebastien D. Mallari, Qinyu Liang, Leah Sadr, Dhivya Meganathan, Anum Tahir, Lisa Tang, Jacqueline Lampert, Marc Levy, Wade Shipley, Hannah E. Fishman, Tarek Rafeedi, Rafael A. Montalvo, Abdulhameed Abdal, Tse Nga Ng, Jinhye Bae, Andrea Tao, Nathan Romero, Zeinab Jahed, and Darren J. Lipomi. "A Simple Method for Photopatterning Commercial PDMS Using an Off-the-Shelf Photodeactivated Hydrosilylation Inhibitor", Submitted to *Advanced Materials*

ABSTRACT OF THE DISSERTATION

Harnessing $FeCl_3$-PEO Photoreactions for Precision Photolithographic Patterning of Conductive PEDOT and Biocompatible PDMS

by

Samuel J. Edmunds

Doctor of Philosophy in Electrical Engineering (Applied Physics)

University of California San Diego, 2024

Professor Darren Lipomi, Chair
Professor Tse Nga Ng, Co-Chair

This dissertation explores the development and application of $FeCl_3$-PEO photoreactions for precision photolithographic patterning in both conductive polymer and silicone elastomer systems. Conductive polymers such as poly(3,4-ethylenedioxythiophene) (PEDOT) are integral to advancements in optoelectronics, sensors, and bioelectronics, but current patterning methods suffer from trade-offs in adhesion, resolution, and scalability. We present a novel vapor-phase polymerization (VPP) approach that utilizes $FeCl_3$-PEO photoreactions to pattern PEDOT films with feature sizes as small as 15 μm and conductivities over 1000 S cm^{-1}. This process employs

a photosensitive initiating film, where UV light selectively deactivates polymerization, achieving high-contrast patterns on diverse substrates. Mechanistic studies reveal that this behavior is governed by photoinitiated ligand-to-metal charge transfer between $FeCl_3$ and the polyether component.

Building on this work, we extend the utility of the $FeCl_3$-PEO photoreaction to pattern biocompatible silicone elastomers, such as Sylgard 184 and Dragonskin, which are crucial materials for microfluidic devices, wearable sensors, and soft bio-MEMS. Incorporating the $FeCl_3$-PEO complex into platinum-catalyzed silicone formulations enables UV-mediated control over hydrosilylation crosslinking, allowing rapid, full-thickness patterning with low doses of 365 nm light. This approach preserves the mechanical tunability and transparency of commercial silicone formulations, offering a straightforward and reproducible method for creating microstructures. To demonstrate the versatility of the silicone photopatterning process, we fabricated microfluidic devices and cardiac microphysiological systems, showcasing the potential of this technique for advanced biomedical device engineering.

Chapter 1

Photography-Inspired Patterned Vapor Phase Polymerization of Conductive PEDOT on Rigid and Stretchable Substrates

1.1 Introduction

The ionically doped conductive polymer poly(3,4-ethylenedioxythiophene) (PEDOT) has played a pivotal role in recent advancements in optoelectronics [1], sensors [2], and bioelectronic devices [3]. The usefulness of PEDOT can be attributed to its combination of electrical and ionic conductivity, semi-transparency, and ability to be deposited from solution [4]. However, two related aspects of conventionally processed PEDOT have hindered its use outside the context of the research laboratory: its adhesion to substrates and difficulty in patterning.

Current approaches to patterning PEDOT have relied on printers (which require bespoke tools and formulations) [5, 6, 7, 8], subtractive processes based on lift-off [9] or etching [10] (which can lead to delamination and high line-edge roughness) or photopatterning. Photopatterning stands out among these techniques due to its potential for high precision, easy implementation between facilities, and scalability. When these advantages are coupled with readily available materials and simple processing conditions, industrial-scale device fabrication becomes possible.

With few exceptions, there are currently three approaches to photopatterning PEDOT. All of these techniques present tradeoffs between stability, minimum feature size, conductivity, mechanical properties, and ease of processing. The first method relies on chain-scission by high-energy UV [11]. This results in lower film conductivity in the exposed regions. Only a shortwave UV source (254 nm) and a photomask are required to achieve patterning. However, large exposure doses are necessary, and high-intensity shortwave UV sources are currently difficult to obtain.

The second set of photopatterning methods introduces light-sensitive functional groups to the PEDOT chain [12, 13]. Upon UV exposure, these functional groups crosslink, resulting in the exposed regions possessing lower conductivity. These methods require the chemical modification of the monomers before the PEDOT film is created, resulting in more complex processing and significantly lower overall PEDOT film conductivity. The films also tend to be unstable because the conductive PEDOT remains uncrosslinked.

The third set of methods incorporates additives into suspensions of PEDOT that form crosslinked networks upon UV light exposure [14, 15, 16, 17, 18, 19, 20]. These methods typically present the smallest trade-offs, with some achieving high conductivity, and others remarkable stretchability. However, the best methods require the use of advanced synthetic techniques that may be out of reach for many users.

Here, we present a fourth method that achieves high conductivity and at most a 15 μm minimum feature size while exhibiting improved adhesion and abrasion resistance on a variety of substrates. Furthermore, this method relies on easy-to-obtain reagents, ubiquitous equipment, and is compatible with substrates possessing various interfacial properties. To achieve this, we use an in-situ polymerization method known by the term ”vapor-phase polymerization” (VPP). In VPP, a polymer is synthesized directly on a substrate coated with a thin film that initiates polymerization after exposure to vapor containing the monomer [21]. This technique has been used extensively to produce highly conductive PEDOT and polypyrrole thin films and patterns using printing techniques [22, 23].

Recently, it has been demonstrated that if a VPP initiating film is exposed to UV light before vapor exposure, the polymer formed during VPP is not cohesive. This property was utilized to pattern the films by exposing the samples through a photomask. The material formed in the exposed regions was then removed by aggressive solvent washing [24]. This method has two significant limitations. First, since there is some form of PEDOT in both the exposed and unexposed regions, high contrast is difficult to obtain. Conductive traces produced in this manner may be poorly defined. Second, to achieve selective removal in the exposed regions, the polymer formed must adhere poorly to the substrate.

Iron(III) complexes are known to be highly photoactive [25, 26]. $FeCl_3$ has been used extensively as a generator of chlorine radicals in photochemical reactions [27, 28, 29, 30, 31, 32, 33, 34]. We hypothesized that the patterning observed in previous VPP studies was the result of a similar photochemical process. Therefore, the patterning could be enhanced by incorporating

highly active $FeCl_3$. We expected this addition to reduce the necessary exposure dose of UV light and lead to observable oxidative decomposition of the PEO-PPO-PEO binder [35]. These changes would precede faster PEDOT polymerization kinetics in the exposed regions of the VPP initiating film. Unexpectedly, we observed *slower* polymerization kinetics in the exposed regions. This suppression of polymerization led to enhanced contrast and the opportunity to enhance the adhesion and stability of these films.

Enhancing the stability and adhesion of PEDOT films is a continuing goal in the production of electrochemical devices and biointerfaces [36, 37]. Most methods to improve the adhesion of PEDOT films rely on roughening substrates [38], introducing a polymer 'glue' [39, 40, 41], or by covalently 'grafting through' functional groups present on the surface of substrates [42, 43, 44, 45]. It has been demonstrated that covalent grafting provides more robust adhesion than other methods [46]. To covalently graft PEDOT to a surface during the VPP process, we functionalized the substrate surface using an organosilane which features an aromatic moiety. This group can then can become enchained to the PEDOT backbone during oxidative polymerization, as shown in Figure 4a. We found that this method delivered enhanced adhesion of PEDOT to both rigid and stretchable substrates.

1.2 Experimental Design

A schematic summary of our proposed photopatterning process is shown in Figure 1.1a. It begins with the preparation of the initiating film, which is deposited from a solution containing a solvent, an oxidant, a coordinating ligand, and a photoactive species. Like in previous studies, our initiating film primarily consists of iron(III) p-toluenesulfonate ($Fe(OTs)_3$), along with with Pluronic P-123 (a triblock copolymer consisting of poly(ethylene oxide) alternating with poly(propylene oxide)). It is thought that p-toluenesulfonate self-assembles with the Pluronic P-123 to form ordered scaffolds for the polymerization [47]. This "scaffolding" effect leads to a

morphology which encourages high conductivity.

In processes containing only $Fe(OTs)_3$ as the oxidant, photopatterning has been attributed to photophysical changes in the iron(III) coordination shell[24]. These changes lead to activation of the oxidant and increased rate of polymerization in the exposed regions and thus a poor morphology which is the basis of the decreased cohesion in the conductive polymer films. In our process containing $FeCl_3$, we believe that the UV light is causing the formation of chlorine radicals by a ligand-to-metal charge transfer (LMCT) process[48]. In a LMCT process, a photon is adsorbed and an excited state is formed where an electron previously donated to the ligand is transferred to the metal center. Chlorine radicals generated by LMCT $FeCl_3$ are known to react with polyethers via a hydrogen atom transfer (HAT) process in solution phase [49] and in solids [35]. However, it is unclear how this process results in the suppression of PEDOT polymerization.

In the vapor-phase polymerization of EDOT to PEDOT, oxidative polymerization is thought to occur at the initiating film. This process results in a PEDOT thin film doped with the anion of the oxidant[50, 51]. We thus hypothesized that oxidative polymerization could be inhibited either by (1) preventing the oxidation of the monomer or (2) terminating the radical cation formed after oxidation. We hypothesised that the chlorine radical generation and reduction of the iron salt may be capable of achieving one of these outcomes. We confirmed the role of the LMCT radical generation process by attempting to inhibit PEDOT polymerization by incorporating other iron salts. We then used spectroscopic techniques to investigate the evolution of the LMCT adsorption peaks, the oxidation state of the iron salts, and the introduction of new functional groups to the polyethers.

This information is used to optimize the photopatterning process for contrast, conductivity, and processing characteristics. We then engineered a process by which the films could be covalently bonded to the substrate, in situ, by adding N-[3-(trimethoxysilyl)propyl]aniline (AnPTMS) to the surface of glass and silicone substrates. This aniline derivative has an aromatic functional group that would be activated for electrophilic substitution by its pendant amine; this

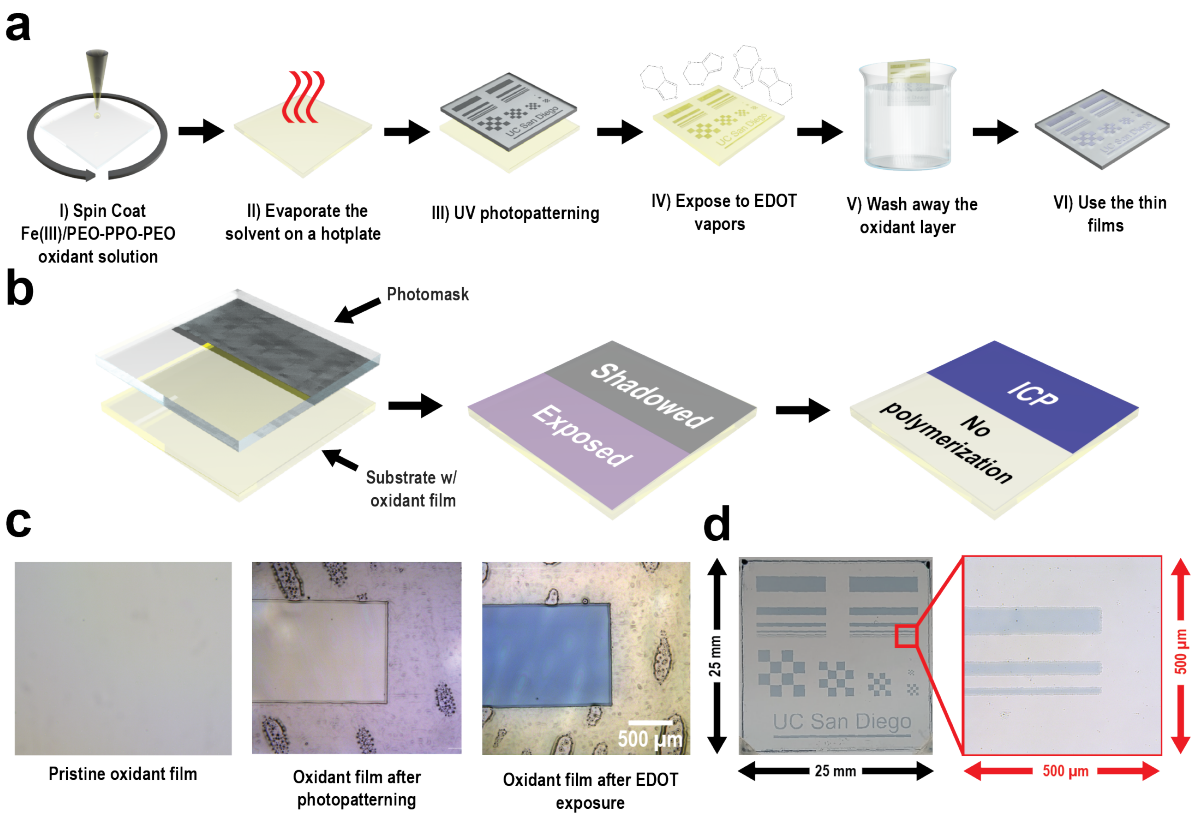

Figure 1.1: a) This schematic summarizes the process of creating PEDOT microstructures using the photo activated ligand-to-metal charge transfer process of iron(III) chloride and vapor-phase polymerization. (I) A film of Fe(III) and PEO-PPO-PEO is spin-coated onto a substrate. (II) The film is then heated on a hotplate to remove the solvent. (III) The film is photopatterned using 365 nm UV light and a photomask. (IIII) The sample is exposed to ICP vapors in a vacuum chamber, leading to spontaneous polymerization. (V) After polymerization is complete, the Fe(III) and PEO-PPO-PEO film is removed by washing it off in an ethanol bath, (VI) leaving behind the PEDOT films ready for use. b) This schematic illustrates the photo-patterning process: the prepared initiating film is exposed to UV light through a transparent photomask. c) These photos demonstrate the changes observed in the initiating thin film after exposure to 365 nm UV light and subsequent EDOT vapors. Logo adapted with permission from UC San Diego. d) The photopatterning process is shown to be effective down to 15 μm.

means that it is possible for oxidized EDOT monomers to react with it. We believed that these aniline functional groups could be incorporated into the PEDOT and serve as anchor sites for the film.

1.3 Results and Discussion

Our experimental design emphasised achieving a large difference in the amount of PEDOT observed in the exposed and unexposed regions. This difference was assessed by examining the films by optical microscopy after EDOT vapor exposure and determining if polymerization had occurred in the exposed regions (Figure 1.1c). If PEDOT was present in the exposed regions, the "contrast" was deemed insufficient. In general, we found that the deactivation of the initiating film, and thus high contrast, was only possible when three conditions had been met. First, enough $FeCl_3$ needed to be present in the film. Second, the film needed to adsorb an adequate amount of 365 nm light. Third, a barrier against the ingress of oxygen needed to be present during the photopatterning process.

Optimization of the initiating film composition and processing was carried out with these factors in mind. We sought to create a user-friendly methodology and achieve high resolution patterning while maintaining the high conductivity of the VPP process. In refining these properties, we discovered a complex interplay among many variables. For our purposes, the most effective oxidant solution comprised the following components by mass: 5 parts of 2-methoxyethanol, 1 part of Pluronic P-123, 0.85 parts of $Fe(OTs)_3$, and 0.15 parts of $FeCl_3$. This solution was spin coated at 1500 RPM for 30 s and baked at 80 °C on a hotplate for two minutes. Initiating films were patterned by placing a photomask in direct contact with the samples and exposed to ten seconds of 11.7 mW/cm^2 365 nm UV light. VPP was carried out by placing liquid EDOT and the samples in a vacuum oven at a pressure of 10 Torr and a temperature of 35 °C for 30 minutes. The excess initiating film was removed by soaking in a bath of ethanol while agitating the sample.

With this solution composition and processing conditions, we were able to prepare PEDOT films doped with p-toluenesulfonate and chloride possessing conductivities of approximately 1000 S/cm (Figure 1.2b). We achieve consistent patterning down to a lateral resolution of 15 μm (the smallest linewidth tested) (Figure 1.1d). We believe that the conductivity can be enhanced with dopant exchange [45, 52], while the patterning resolution can be improved with higher quality lithography equipment and techniques.

1.3.1 Exploration of the Photopatterning Mechanism

Photopatterning was only possible when the PEO-PPO-PEO block copolymer was present and the ratio of $Fe(OTs)_3$:$FeCl_3$ was greater than 8.5:1.5 (Figure 1.2a). In most situations, the radicals that are generated by $FeCl_3$ are unable to escape the coordination shell and attack other molecules. In our system, the PEO-PPO-PEO block copolymer disperses the $FeCl_3$. Under these conditions, it is possible for these free radicals to react with the PEO-PPO-PEO block co-polymer via hydrogen atom transfer (HAT) processes [53]. We believe that this is the primary mechanism of the photochemical modifications to the oxidant film. Recent studies leveraging the LMCT radical generation process to modify PEO have shown that using $FeCl_3$ provides the highest product yields compared to other iron(III) salts [49]. This is due to the higher efficiency radical generation. To verify that a similar radical generation process was occuring in our samples, we attempted photopatterning with initiating films consisting of PEO-PPO-PEO and a single type of iron(III) salt. We tried $FeCl_3$, iron(III) nitrate, iron(III) bromide, iron(III) methanesulfonate, and $Fe(OTs)_3$.

The only samples showing inhibition of polymerization in the exposed regions were those that contained $FeCl_3$. Samples containing $Fe(OTs)_3$ did show a reduction in conductivity and faster polymerization rate with increasing exposure doses. However, upon removal of chloride impurities with silver nitrate, the exposed and unexposed regions became indistinguishable by optical microscopy. Based on these results, we believe that LMCT radical generation is responsible

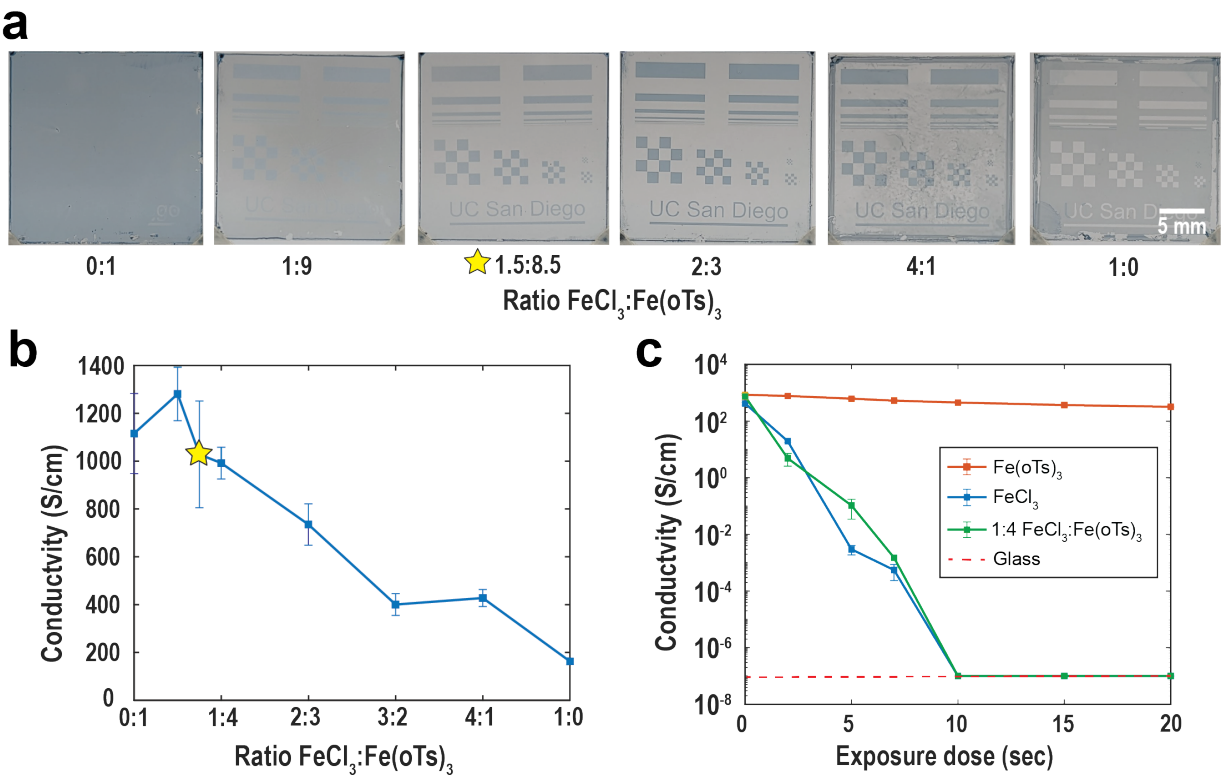

Figure 1.2: a) These photos demonstrate that the photo-patterning process yields optimal results when using a combination of $FeCl_3$ and $Fe(OTs)_3$. Logo adapted with permission from UC San Diego. b) This plot illustrates our ability to easily regulate the film's conductivity by adjusting the ratio of $FeCl_3$ to $Fe(OTs)_3$. By employing a blend of 1.5 parts $FeCl_3$ and 8.5 parts $Fe(OTs)_3$, we achieved a conductivity of approximately 1000 S/cm, meeting the established benchmark for PEDOT formulations. c) This plot indicates that even a small quantity of $FeCl_3$ can be added to the initiating thin film while still achieving the desired photo-patterning results. It also suggests that the exposure dosage can be employed to control the final film's conductivity.

for the inhibition of the polymerization in the exposed regions of the samples containing $FeCl_3$. However, films consisting of pure $FeCl_3$ only had conductivities of approximately 185 S/cm.

The ratio of $Fe(OTs)_3$:$FeCl_3$ also determined the conductivity of the final PEDOT films (Figure 1.2b). It has been shown that Pluronic P-123 and $Fe(OTs)_3$ have a special relationship when combined in the vapor-phase polymerization process. Together they create PEDOT films with remarkably high conductivity without any post-treatment; however, $FeCl_3$ has not been shown to participate in this effect. Therefore, we expect that the larger $Fe(OTs)_3/FeCl_3$ ratio will have higher conductivity. However, at ratios greater than 8.5:1.5 $Fe(OTs)_3/FeCl_3$, the

photodefinability decreased rapidly regardless of the exposure dose.

In various polymer thin films containing $FeCl_3$, a photo-induced bleaching effect and accelerated oxidative decomposition have been observed [35, 54, 55]. Our spectroscopic investigation of the photopatterning mechanism began with UV-vis spectroscopy. UV-vis spectroscopy is often used to investigate the coordination state of $FeCl_3$ [56]. Before exposure, UV-vis absorption peaks are present at 320 nm and 360 nm. After exposure, these peaks disappear. We observe this same effect in our films (Figure 1.3d). The photo bleaching effect appears to be closely correlated with the inhibition of VPP in the exposed regions (Figure B1). When the films were left under normal atmosphere without light exposure, the peaks did not fully reappear.

It has been suggested that the bleaching corresponds to the photo-reduction of the iron salts due to the LMCT process occurring in the film [57]. We used X-ray photoelectron spectroscopy (XPS) to check if a persistent change in the oxidation state of the salts was responsible for the inhibition of the polymerization in the exposed regions. Our XPS results did not indicate a change in the ratio of $FeCl_3$ and $FeCl_2$ in our films before and after exposure (Figure 1.3c and Figure B4).

Despite the lack of iron salt reduction, we did observe clear signs of oxidative decomposition in the VPP initiating films after UV exposure. Figure 3d outlines the radical generation by $FeCl_3$ and the radical transfer process to the polyethers. Once these radicals have been transferred to a PEO block, they can then participate in a wide variety of reactions [35, 58]. Oxidative cleavage of the polyether chains requires the presence of molecular oxygen and results in the decomposition of the PEO-PPO-PEO block copolymer. This process results in two macroscopic effects. First, the viscosity of the films in the exposed regions dramatically decreased. Second, the oxidant film in the exposed regions dewetted from the substrate and formed droplets. These effects are consistent with a significant reduction in the molecular weight of the PEO-PPO-PEO polymer. Based on these observations, we believe that when UV exposure is performed in open air, it results in rapid oxidative cleavage of the PEO-PPO-PEO polymer [35].

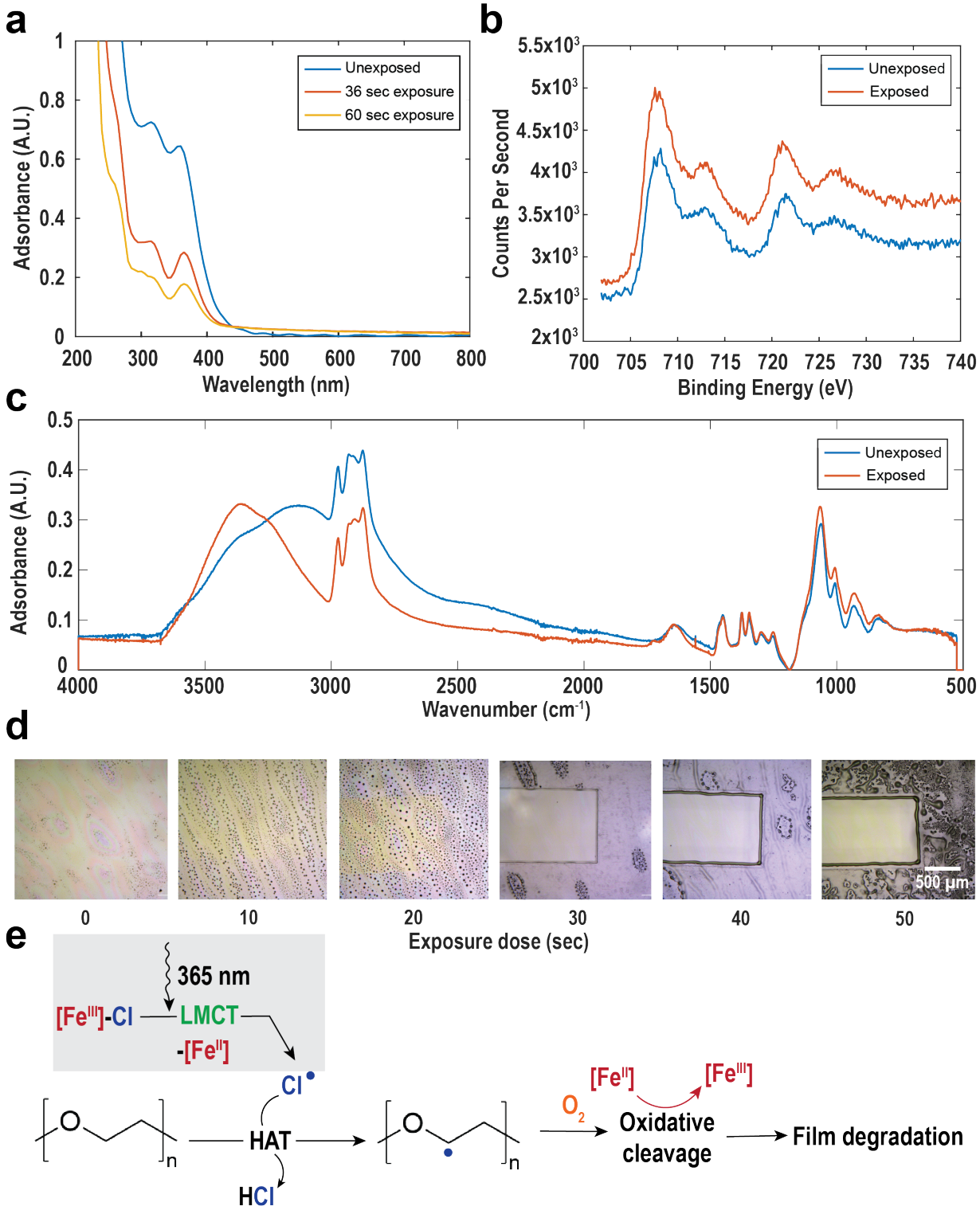

Figure 1.3: a) UV-vis spectroscopy data illustrating the photochromic properties of the $FeCl_3$ and PEO-PPO-PEO film. The attenuation of peaks at 320 nm and 360 nm suggests a decrease in higher-order $FeCl_4^-$ complexes. b) XPS spectra focused on Fe 2p peaks indicate no significant changes in the oxidation state of iron ions before and after UV exposure.

We used Fourier transform infrared spectroscopy (FTIR) to identify chemical changes in the polyether backbone. After exposure, a clear peak appears at 3400 cm^{-1}. This peak is associated with the formation of OOH/OH groups [35]. Other work has shown that the intensity of this peak increases with the addition of ethylene glycol to a mixture of polyether[59]. Ethylene glycol is one of several products possible in the oxidative degradation process of polyethers[58]. These data, along with our macroscopic observations, confirm the photooxidative reactions accelerated by chlorine radical formation due to the $FeCl_3$ LMCT process. However, the suppression of PEDOT polymerization in the exposed regions remains mysterious.

A barrier to oxygen diffusion was necessary to obtain consistent inhibition of EDOT polymerization in the exposed regions. This blockage was achieved by placing the substrate in direct contact with the photomask or by coating the oxidant film with a thin layer of silicone oil. Abundant oxygen is necessary to sustain the diffusion of free radical chain carriers in photooxidative decomposition processes [58]. It has been suggested that oxidative reactions between polymer alkyl radicals/polymer alkyloxy radicals/polymer alkylperoxy radicals and Fe(II) may influence the photochromic mechanism and decrease reversibility of the optical bleaching [35, 60]. We conjecture that a similar process may be responsible for the suppression of PEDOT polymerization in the exposed regions of the VPP-initiating film.

1.3.2 Exposure Conditions Optimization

Patterning was only achieved with a sufficient UV exposure dose. For our oxidant solution blend, we found that this threshold was achieved with only ten seconds of exposure from our 11.7 mW/cm^2 365 nm UV LED (Figure 1.2c). This is ca. 1% of the exposure dose of previous studies[24]. In figure 1.3d, it can be seen that as the exposure dose increased, the boundaries of the unexposed regions start to blend into the exposed regions. This blending results in reduced PEDOT feature size compared to the mask. We suspect that this is a result of scattering and reflection at the substrate or the diffusion of free radical chain carriers. The excess radicals cause

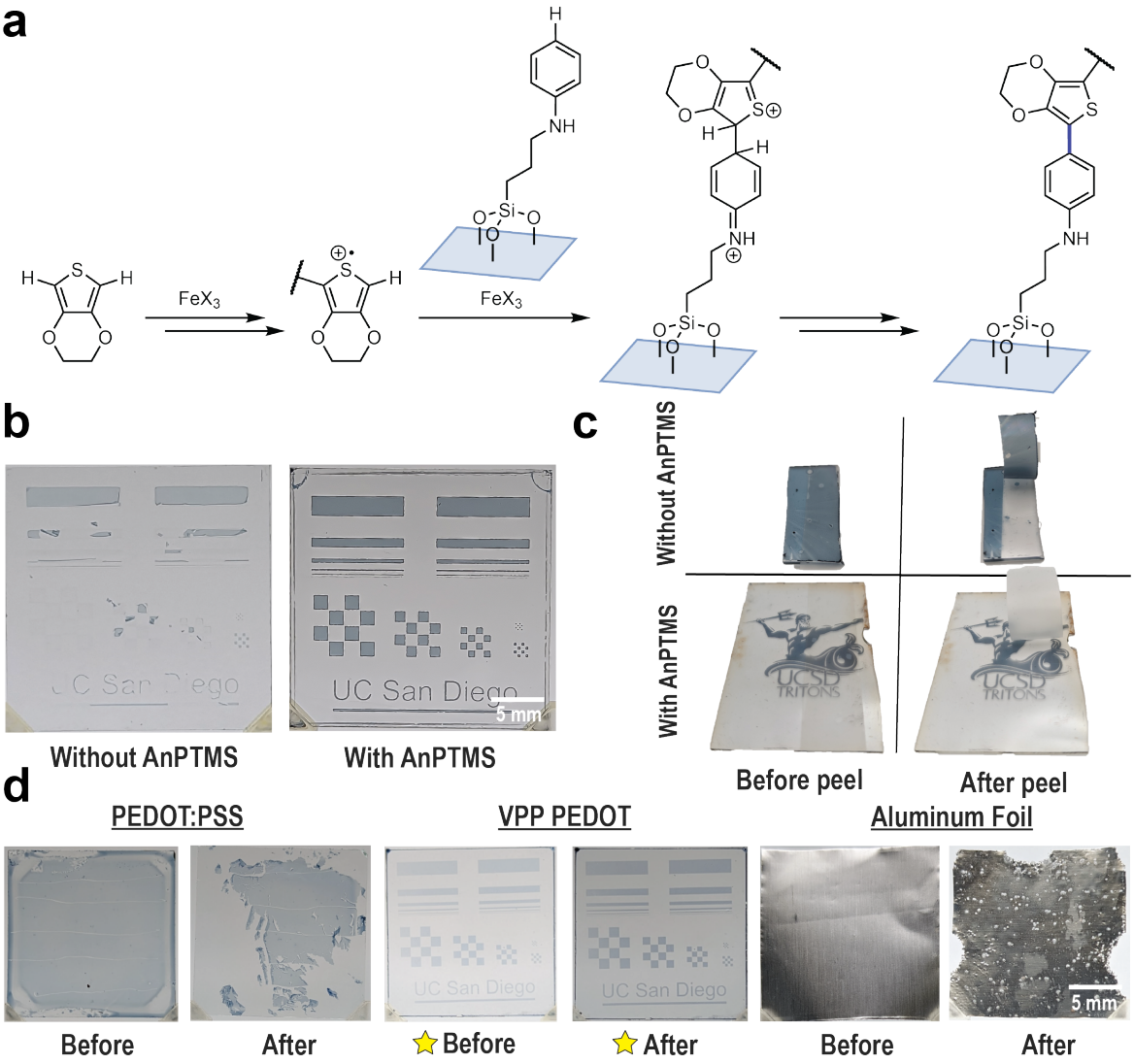

Figure 1.4: a) By applying N-[3-(Trimethoxysilyl)propyl]aniline (AnPTMS) to glass or silicone substrates, we successfully grafted the PEDOT films onto these substrates, resulting in a significant enhancement in the adhesion of the films compared to substrates without the AnPTMS. b) We observed that the patterned films did not withstand the final washing step unless AnPTMS was used. Logo adapted with permission from UC San Diego. c) We conducted a scotch tape test to showcase the adhesion quality of of the PEDOT film to PDMS (Sylgard 184) functionalized with AnPTMS. Logo adapted with permission from UC San Diego. d) To assess the abrasion resistance of the grafted films, we subjected them to four hours of sonication in PBS. For comparison, we included spin-coated PEDOT:PSS and aluminum foil squares in the test. Notably, only the grafted VPP-PEDOT films remained intact. Logo adapted with permission from UC San Diego.

the the films to degrade too much when they are exposed to open air after the patterning process.

The adhesion between the initiating thin films and the photomask was determined by the Fe(III):PEO-PPO-PEO ratio. We selected a 1:1 mass ratio to produce a film that did not stick to the photomask. This choice prevented damage to the oxidant film during the patterning process. While a higher PEO-PPO-PEO content theoretically enhances conductivity, non-uniformity in the initiating film substantially reduced sample yield.

1.3.3 Spincoating Uniformity Optimization

Another source of non-uniformity in the initiating film was spin-coating induced striations. These defects caused thickness variations in the initiating films. To prevent these defects, anhydrous 2-methoxyethanol was selected as the solvent for the intiating film complex. 2-methoxyethanol possesses a high surface tension and a relatively low vapor pressure. These properties enabled spin-coating of high-quality films of the initiating complex[61].

1.3.4 Adhesion Improvement via Grafting-Through an Aniline Functional Silane

The final barrier to device applications was a lack of adhesion between the patterned PEDOT films and the substrates. As can be seen in figure 1.4b, the patterned PEDOT films did not adhere to soda-lime glass well enough to survive the final washing step. Previous studies have compensated for this lack of adhesion by over-polymerizing the films with a post-CVD pre-wash bake step [62]. During this bake step, EDOT dissolved in the initiating film continues to polymerize. The additional cross-linking oligomer growth improves film robustness at the cost of conductivity[63]. To improve the consistency of our patterning, we took advantage of the interaction between the growing conductive polymer film and other species incorporated into the initiating film[64]. By functionalizing our substrates with AnPTMS, we introduced aniline at the

interface between the initiating film and the substrate (Figure 1.4a).

The addition of these anchor sites dramatically improved the adhesion of the films. This resulted in greater abrasion resistance, as evidenced by the improvement in film survival after sonication (Figure 1.4d). To test the limits of this process, we wanted to investigate the increase in the adhesion of the films to notoriously difficult, low surface energy substrates like PDMS. As with the glass, we functionalized the surface of the PDMS with AnPTMS and synthesized PEDOT on the surface. Using this process, we were able to create flexible and stretchable composites of PDMS and patterned PEDOT that are capable of surviving a Scotch tape peel test. The films without AnPTMS were removed easily by the tape (Figure 1.4c).

1.3.5 Applications of the Photopatterned Vapor-Phase Polymerized Materials

Finally, we explored some simple applications to inspire future projects and demonstrate the versatility of the patterning and adhesion improvements. Electrochromic displays are a ubiquitous application of the VPP process. Multi-color electrochromic displays have been realized by serially depositing two or more different conductive polymers using the VPP process [65]. PEDOT and polypyrrole are common examples due to the ease with which they are deposited and the vibrant navy blue and yellow that can be obtained by electrochemically reducing the complexes. However, previous attempts at patterning polypyrrole using UV have been unable to prevent polymerization[66]. We successfully adapted our patterning process to pyrrole and demonstrated a blue and yellow electrochromic display (Figure 1.5d).

It is well known that the stretchability of materials can be increased when they are well adhered to another stretchable substrate [67]. We compared the resistance vs. strain for our PEDOT on PDMS to spray coated PEDOT:PSS on PDMS and our results were consistent with this hypothesis (Figure 1.5b). We then created a conformal sticker with our PEDOT on PDMS system to highlight future wearable applications(Figure 1.5c).

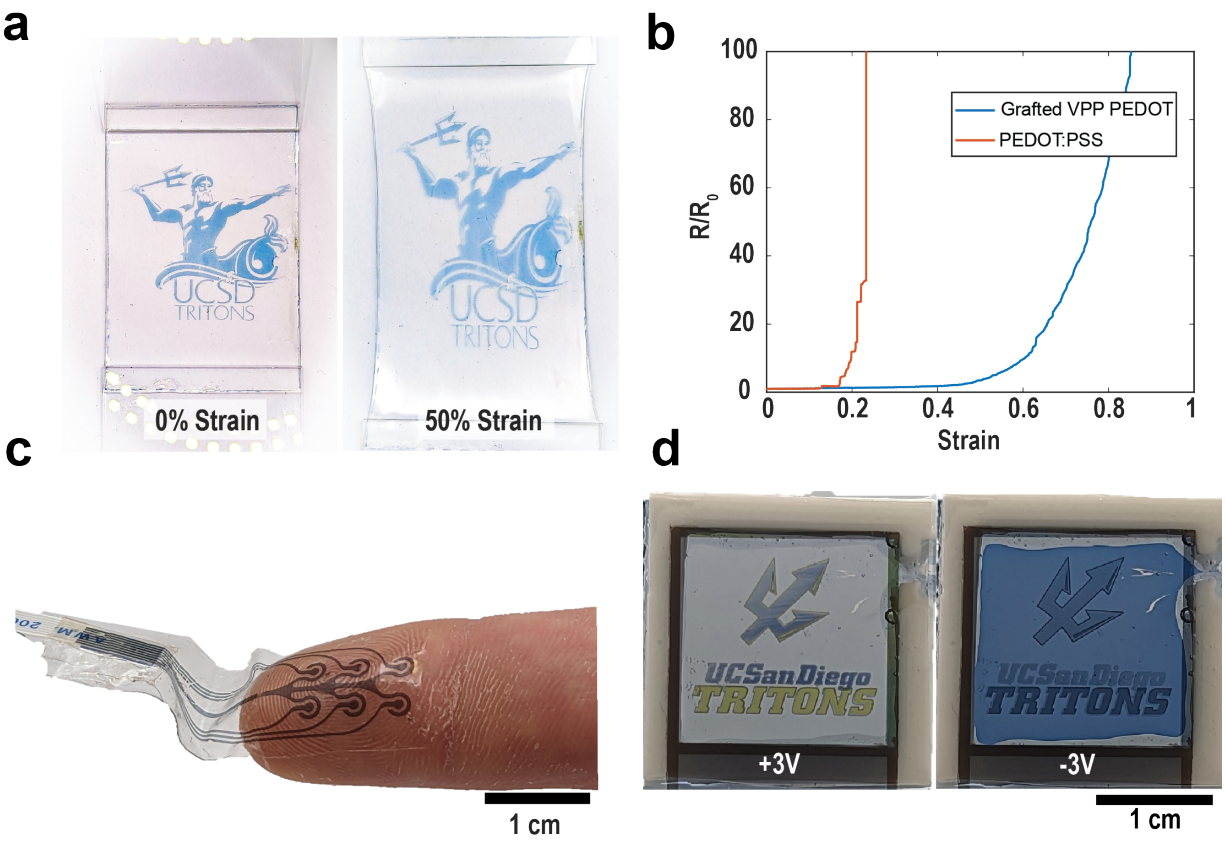

Figure 1.5: a) These photos depict an unstretched and stretched logo made from PEDOT patterned onto PDMS. Logo adapted with permission from UC San Diego. b) We compared the resistance versus strain for grafted VPP-PEDOT and spray-coated PEDOT:PSS on PDMS functionalized with AnPTMS. Our findings revealed that the grafted sample effectively distributed the strain, experiencing minimal delamination and cracking as it was stretched. Consequently, the grafting process significantly improves the stretchability of the composites. c) A PEDOT on PDMS conformal sticker. d) An electrochromic display demonstrating that our process is capable of patterning both PEDOT and poly pyrrole. Logo adapted with permission from UC San Diego.

1.4 Conclusion

We have presented a versatile approach for achieving high-contrast images of PEDOT and polypyrrole using a vapor phase polymerization process. Key attributes of the process include (1) its photodefinability and (2) its adhesion to rigid and stretchable substrates. Photodefinability was achieved by selective deactivation of a gel-like initiating film using $FeCl_3$ as the photoactive species. Critically, oxygen had to be excluded from the film to achieve deactivation of polymerization in the exposed regions. Adhesion was promoted by modifying the substrate with N-[3-(trimethoxysilyl)propyl]aniline (AnPTMS). Resulting patterns of PEDOT were highly conductive, and amenable even to PDMS substrates. The ability to pattern different conductive polymers opened the door to multicolored electrochromic displays.

The process we describe, in particular its reliance on ligand-to-metal charge transfer and the photogeneration of atomic chlorine, is reminiscent to the chemistry of classical black-and-white photography. Given that the extent of deactivation can be controlled by the exposure dose, it should be possible to generate gradient patterns and optoelectronically active films of greater complexity than those demonstrated here. For example, gradients of conductive, electrochromic, or biologically active materials using shaded transparency masks analogous to photographic negatives.

1.5 Acknowledgments

This chapter of this dissertation includes material as it appears in ”Photography-Inspired Patterned Vapor Phase Polymerization of Conductive PEDOT on Rigid and Stretchable Substrates,” published in ACS Materials Letters, 2024. This work was co-authored with Armando D. Urbina, Hannah E. Fishman, Yi Qie, Rafael A. Montalvo, Noel Sebastien D. Mallari, Marc N. Levy, Rachel Blau, Abdulhameed Abdal, Andrea M. Armani, Tse Nga Ng, Nathan A. Romero, and Darren J. Lipomi, and I was the primary investigator and author of this material.

Chapter 2

A Simple Method for Photopatterning Commercial PDMS Using an Off-the-Shelf Photodeactivated Hydrosilylation Inhibitor

2.1 Introduction

Silicone elastomers, e.g. polydimethylsiloxane (PDMS), are widely used and essential materials in various scientific settings and commercial applications. Properties such as high breakdown voltage, optical clarity, tunable mechanical properties, and adjustable surface energies make them ideal for use as potting materials for high-voltage circuitry, protective coatings, adhesives, and fillers in large 3D structures, such as cosmetic implants and prosthetics. Additionally, the ability to create relief structures in PDMS makes it valuable for applications in stretchable electronics[68], microfluidic channels in wearable devices[69], and soft structures in biological microelectromechanical systems (bio-MEMS)[70]. These advanced applications often require precise patterning of freestanding microstructures with well-defined mechanical properties.

Current patterning techniques capable of generating apertures in PDMS films—i.e., "full-thickness" patterning—such as cutting with knives, laser cutting, embossing, or photopatterning, have limitations in resolution, accuracy of alignment, preservation of mechanical properties, and ease of use. Cutting films of silicone with blades or stencils (e.g., cookie cutters) is challenging due to the limitations in sharpness of cutting instruments. Moreover, sharp, custom tools can be difficult to acquire and often produce deformed edges. Laser cutters can produce features as small as 100 μm[71]; however, the heat generated typically alters the mechanical properties around the burned edges and causes line-edge roughness that is difficult to control[72].

Using pre-patterned molds and stamps to emboss features into silicone elastomers—i.e., soft lithography[73]—has been used to create arrays of holes and other features in films[74]. This approach can produce very small features, such as arrays of 20 μm holes in films. However, using these structures requires transferring the stamps or films, which can easily damage the features during the transfer process.

Directly photopatternable silicone elastomers can achieve high-resolution features with good alignment accuracy between multiple layers. However, a straightforward method for produc-

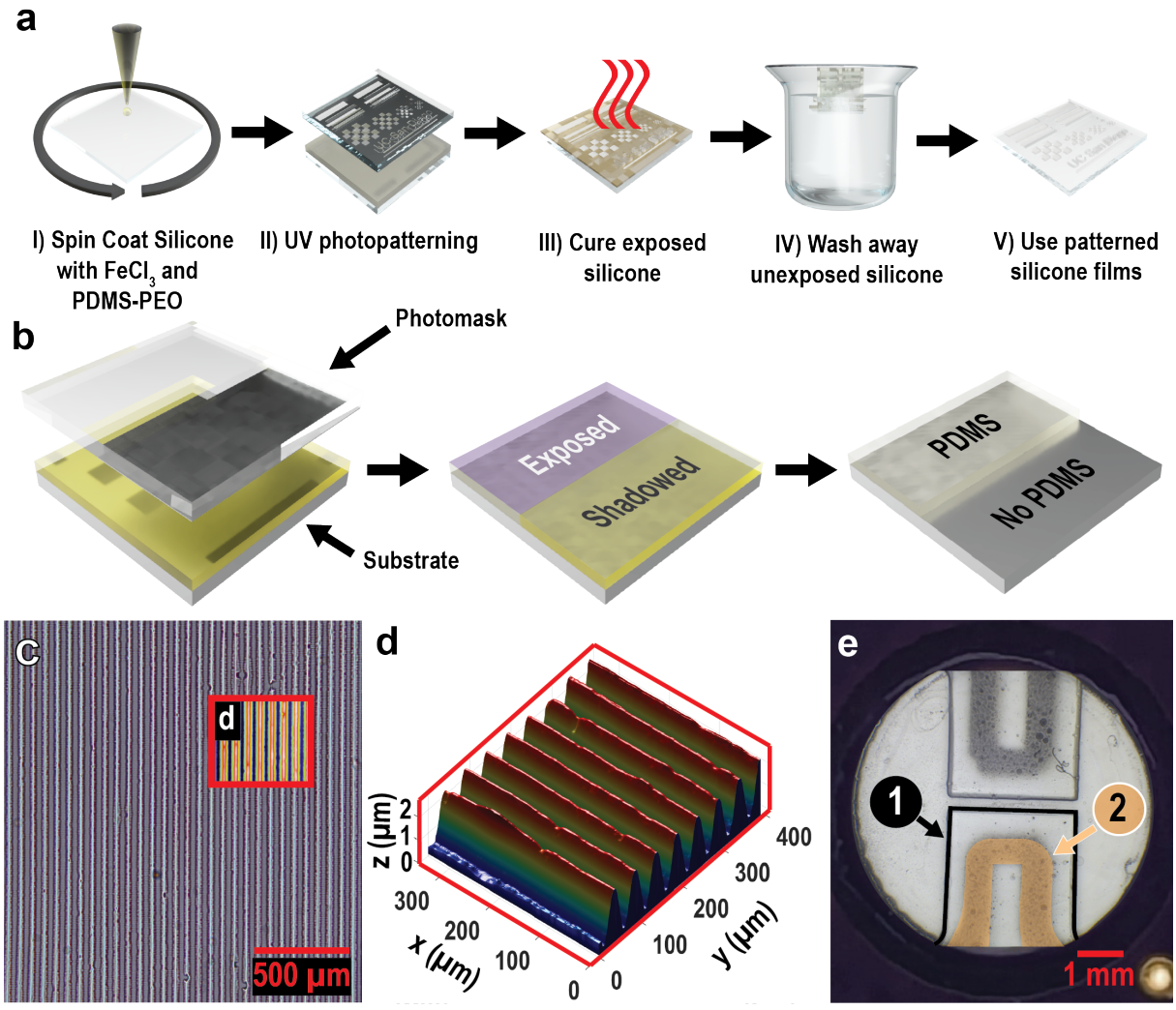

Figure 2.1: (a) Schematic illustrating the process of patterning silicone elastomers using $FeCl_3$ and PEO-PDMS photoreactions: (I) A film consisting of liquid silicone elastomer mixed with the $FeCl_3$ and PEO-PDMS "photopatterning agent" is spin-coated onto a substrate. (II) The film is exposed to 365 nm UV light through a photomask. (III) The exposed silicone is solidified at 90°C on a hotplate. (IV) The unexposed silicone is washed away with a solvent such as ethyl acetate. (V) The remaining PDMS microstructures are ready for use. (b) The addition of $FeCl_3$ and the PEO-PDMS copolymer enables the silicone elastomer to behave like a negative photoresist. (c) Optical microscope image of Sylgard 184 patterned into 20 μm lines spaced 30 μm apart. (d) 3D profile of the Sylgard 184 lines from panel (c). (e) A bioMEMS device for measuring the contractile force of human-induced pluripotent stem cell (hIPSC)-derived cardiomyocytes. The device consists of two (1) 15 μm thick silicone cantilevers with (2) embedded gold-plated silver nanowire strain gauges.

ing photopatternable films of biocompatible silicone elastomers with good optical transparency and widely tunable mechanical properties has yet to be developed. Additionally, the formulations described in research often rely on precursors that need to be custom synthesized or sourced from suppliers with inconsistent product availability or quality. Commercially available formulations are typically tailored for specific applications, with proprietary constituents, and are not characterized for properties relevant to the fabrication of biocompatible devices.

Three crosslinking processes dominate the chemistry of commercially available silicone elastomers[75]: radical-initiated curing, platinum-catalyzed hydrosilylation, and moisture curing (i.e., room temperature vulcanization). Because of their low viscosities, radical-curing and platinum-catalyzed hydrosilylation-based silicones are commonly used in research to produce films. Two main radical-mediated processes are used to crosslink silicone elastomers: vinyl-vinyl reactions[76] and thiol-ene reactions[77, 78, 79, 80].

Both vinyl-vinyl and thiol-ene based silicones can use a UV-activated radical generator to initiate crosslinking[81]. Under certain conditions, photolithography can be used to create microstructures with these elastomers. However, vinyl-vinyl based methodologies are sensitive to oxygen, making it challenging to accurately reproduce structures under atmospheric conditions. Additionally, commercial formulations using these processes do not allow for easy tuning of mechanical properties because they are sold as proprietary, premixed single-part resins.

In contrast, two-part formulations based on platinum-catalyzed hydrosilylation-based crosslinking typically enable easy tuning of mechanical properties. These formulations consist of five main components: a vinyl-functional PDMS, a hydrosilane-functional PDMS, a platinum catalyst (often Karstedt's catalyst), a curing inhibitor (to allow for uniform mixing and control of solidification time), and fumed silica (to enhance mechanical robustness)[82]. The mechanical properties of these formulations can be adjusted by varying the ratio of vinyl-functional to hydrosilane-functional PDMS in the silicone liquid mixture before crosslinking. However, current methods of photopatterning hydrosilylation-based silicone elastomers require large doses of

shortwave UV, photosensitive platinum catalysts, or custom-synthesized inhibitors. None of these approaches utilize widely available processing conditions or commercially available silicone formulations.

When Karstedt's catalyst is mixed with an aromatic molecule (e.g., benzophenone[83] or xylenes[84]) and exposed to shortwave UV ($<$365 nm), it is known to degrade slowly into inert colloidal platinum[85]. This property has been used to photopattern commercially available silicone elastomers[84, 68, 76, 83, 86]. However, effectively degrading the catalyst requires large exposure doses. While this technique has proven useful in research contexts, it is limited to patterning features down to approximately 100 μm, and the long exposure times (typically 10+ minutes with a standard source) make scaling difficult.

Extensive commercial research has been conducted on the development of photo-activated platinum catalysts [87, 88, 89, 90, 91, 92, 93, 94]. Some scientific publications have also examined these catalysts [95, 96, 97, 98, 99, 100, 94]. Generally, these studies found that silicone formulations using photo-activated platinum catalysts exhibited significant differences in solidification time depending on whether the samples were exposed to UV light. However, the use of these catalysts for patterning silicone films or as additives in non-photoactive formulations has not been explored.

Recently, we observed that oxidative polymerization of poly(3,4-ethylenedioxythiophene) is suppressed by exposure to UV light in films composed of $FeCl_3$ and polyethers[101]. Our laboratory used this property to deposit patterned films of conductive polymers. Building on these findings, we hypothesized that the apparent reduction in the reactivity of $FeCl_3$ due to its photoreaction with polyethers could be exploited to achieve photopatterning in other systems.

When $FeCl_3$ is added to hydrosilylation-based silicone elastomers, it inhibits the crosslinking process and thus increases the time needed for curing. We hypothesized that combining $FeCl_3$ with a commercially available polyethylene oxide (PEO)-co-PDMS copolymer (PEO-PDMS) could allow control over this inhibition through UV light exposure. Our experiments showed that

incorporating the $FeCl_3$-PEO-PDMS complex into commercially available platinum-catalyzed hydrosilylation-based silicone elastomers results in faster curing of regions exposed to UV light compared to unexposed regions.

By exposing films of the silicone liquid mixed with the $FeCl_3$-PEO-PDMS complex to UV light through a photomask, reliable photopatterning can be achieved. Using this method, films of Sylgard 184, Sylgard 527, Dragon Skin, and Ecoflex were successfully patterned. The technique allows for full-thickness patterning using small doses of 365 nm UV light, while preserving the tunability of mechanical properties, optical transparency in low silica formulations, and exceptional biocompatibility. To demonstrate the capabilities of this process, we fabricated microfluidic devices and cardiac microphysiological devices with integrated sensors.

2.2 Results and Discussion

A schematic summary of our photopatterning process is presented in Figure 2.1a. To begin, the liquid precursors of a two-part platinum-catalyzed hydrosilylation-based silicone elastomer are mixed according to the manufacturer's instructions. These liquid precursors are then combined with our "photopatterning agent," which consists of a solution of $FeCl_3 \cdot (H_2O)_6$ and a PEO-PDMS copolymer (Gelest DBE-712). Films of the silicone elastomer are prepared by spin coating. Photopatterning is achieved by exposing the films to UV light through a photomask. The samples are then transferred to a hotplate, where the exposed regions solidify, while the unexposed regions are washed away in a solvent bath. This process was effective for all platinum-catalyzed hydrosilylation-based silicone elastomers tested (Figure 2.1b-e) but was ineffective for other types of silicone.

The goal of this process was to create high-resolution features while maintaining the optical transparency, biocompatibility, and mechanical tunability of the base elastomers. We found that patterning small features required a significant difference in the solidification time

between exposed and unexposed regions. Solidification time was determined as the point when the films could no longer be smeared with a swab. We refer to this difference in solidification time as the "contrast" of the process. Therefore, our optimization efforts focused on maximizing contrast while minimizing changes to the optical and mechanical properties of the formulations.

Since Sylgard 184 is the most commonly used silicone formulation in both our research group and others, we focused our optimization efforts on this material. To demonstrate the versatility of our photopatterning approach, we adapted the process (though not fully optimized) for use with other silicone formulations such as Sylgard 527, Dragon Skin, and Ecoflex. Optimal photopatterning results were achieved with Sylgard 184 when the photopatterning agent consisted of 4 parts methanol, 0.5 parts $FeCl_3$, and 0.5 parts PEO-PDMS copolymer by mass. For most commercial formulations, this solution was added at a ratio of 0.1 ml per gram of silicone liquid. However, for very soft formulations like Sylgard 527, a reduced ratio of 0.025 ml per gram of silicone liquid was required. See the supplementary information for example processing conditions for each type of silicone tested.

2.2.1 Exploration of the Photodeactivated Inhibition Mechanism

In all formulations of silicone elastomers tested, the addition of $FeCl_3$ to the liquid precursors resulted in longer solidification times (Figure 2.2a), indicating that the $FeCl_3$ complex inhibits Pt-catalyzed hydrosilylation reactions. Moreover, significantly shorter solidification times were observed in UV-exposed samples compared to unexposed controls, although accelerated curing was only seen in samples containing PEO-PDMS (Figure 2.3b). These findings suggest that $FeCl_3$ acts as an inhibitor that is deactivated upon UV irradiation.

To rationalize the extended solidification times in samples with $FeCl_3$, we propose that Fe(III) inhibits the hydrosilylation reaction by oxidizing Pt(0) to higher-valent Pt(II) or Pt(IV) species. Based on the reported redox potentials for $FeCl_3$ ($E(Fe^{3+/2+}$ = +0.8 V vs. SCE)[102] and molecular Pt(0) complexes ($E(Pt^{1+/0}$ = –0.1 V vs. FC)[103, 104], estimated at +0.3 V

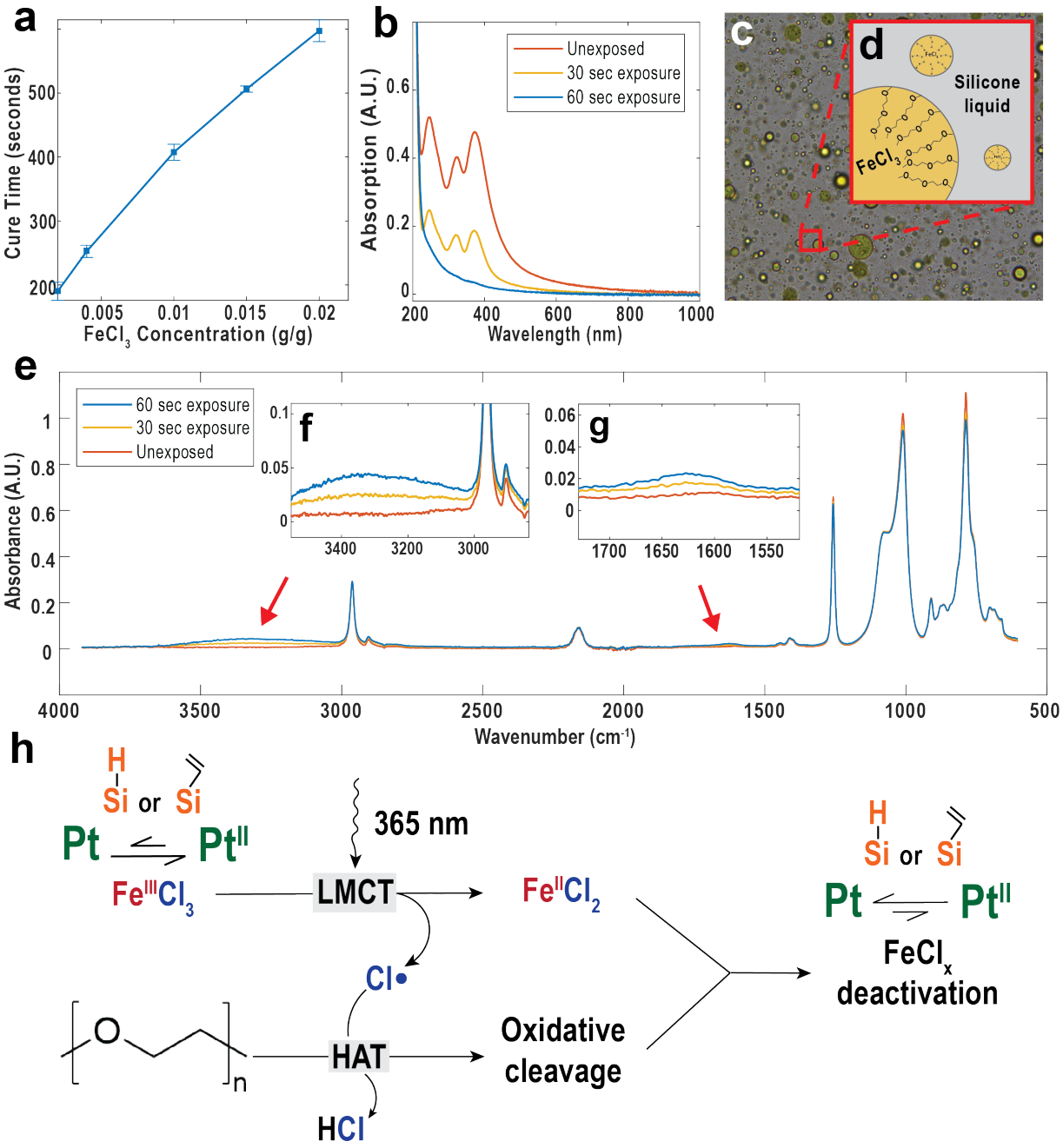

Figure 2.2: (a) The cure time of the silicone elastomers increases with the addition of $FeCl_3$ to the formulation. (b) UV-vis spectroscopy data showing the photochromic properties of the film. The disappearance of absorption peaks at 245 nm, 325 nm, and 374 nm suggests a reduction in higher-order $FeCl_4^-$ complexes in the film. (c) A photograph of the $FeCl_3$ and PEO-PDMS emulsion present in the film. The image was taken from a sample with large droplet sizes due to microscope resolution limitations. See SI for images of properly mixed emulsions. (d) An illustration depicting the $FeCl_3$ and PEO-PDMS emulsion, with PEO chains interacting with the emulsion interior. (e) Fourier transform infrared spectroscopy (FTIR) data of the custom silicone formulation with the photopatterning agent. The appearance of new peaks at 3400 cm^{-1} and 1630 cm^{-1} indicates the formation of PEO oxidation products.

vs. SCE [105], oxidation of Pt(0) by $FeCl_3$ is predicted to be thermodynamically favorable by approximately 0.5 V or 12 kcal/mol. This oxidation produces $FeCl_2$ and Pt(2+) (or Pt(4+)) as products[103]. These higher-valent platinum oxidation states cannot enter the catalytic hydrosilylation manifold without being reduced to Pt(0). However, both the vinylsiloxane and hydrosilane components of the silicone elastomer formulations are known to reduce Pt(2+) (or Pt(4+)) to catalytically active Pt(0)[106, 107]. This reduction process is responsible for the relatively long induction periods observed when H_2PtCl_6 is used as a hydrosilylation catalyst[108]. We propose that the oxidation of Pt(0) to Pt(2+) is reversible in the presence of $FeCl_3$ and hydrosilanes/vinylsiloxanes, with the equilibrium favoring catalytically inactive Pt(2+) as long as $FeCl_3$ remains in excess. As $FeCl_3$ is depleted, the equilibrium shifts towards Pt(0), allowing hydrosilylation to initiate.

In a separate system, we[101] and others[35, 55] observed the rapid photochemical conversion of $FeCl_3$ in the presence of PEO-containing polymers, likely yielding $FeCl_2$ (or other Fe(2+) complexes) as photoproducts via ligand-to-metal charge transfer (LMCT)-mediated generation of Cl• radicals from $FeCl_3$[27, 28, 29, 30, 31, 32, 33, 34]. In this mechanism, the polyether serves as a terminal reductant by quenching the oxidizing Cl• radicals. Consistent with this mechanism, UV-Vis spectra of our silicone formulations containing $FeCl_3$ and PEO-PDMS, collected after UV irradiation, show nearly complete conversion of Fe(3+) to Fe(2+), as indicated by the disappearance of the characteristic absorption bands of Fe(3+)-chloride complexes between 300-400 nm (Figure 2.2c)[34, 109]. This rapid depletion of $FeCl_3$ upon UV exposure accelerates the reduction of Pt(2+) to Pt(0), leading to faster curing compared to unexposed samples. The requirement of PEO-PDMS for significant cure time contrast aligns with this proposed mechanism.

Seeking systematic insight into this photo-deinhibition mechanism, we conducted further experiments using custom-formulated silicone elastomer samples, excluding the proprietary additives typically found in commercial formulations. These elastomers consisted of two crosslinking

components: vinyl-terminated PDMS and a PDMS-co-methylhydrosiloxane copolymer. In this simplified system, we confirmed that the $FeCl_3$-PEO-PDMS complex acts as an inhibitor by mixing the photopatterning agent with the silicone, but without any platinum catalyst. No curing occurred after UV exposure and heating, confirming that the $FeCl_3$-PEO-PDMS complex does not generate a reduced iron species capable of catalyzing hydrosilylation[110, 111, 112, 113].

Next, we tested the effect of the photopatterning agent in the presence of a platinum catalyst. We prepared a custom silicone mixture containing vinyl-terminated PDMS, Karstedt's catalyst (90 ppm), and PDMS-co-methylhydrosiloxane copolymer mixed with the photopatterning agent. For comparison, we prepared another mixture with the same components but without the photopatterning agent. The results showed that the sample containing the photopatterning agent solidified in 88 minutes, while the sample without the agent solidified in 105 seconds, consistent with our initial experiments on commercial formulations.

To investigate whether UV exposure dose modulates the degree of inhibition, we prepared films containing both the photopatterning agent and the platinum catalyst. Half of the films were exposed to UV light before being placed on a hotplate at 90°C. The UV-exposed films solidified in 40 ± 11.5 seconds, while the unexposed films solidified in 112.5 ± 26.3 seconds. These results demonstrate that UV exposure significantly accelerates the solidification process by deactivating the inhibitory effect of the $FeCl_3$-PEO-PDMS complex.

We further explored the chemical changes in the silicone film using Fourier transform infrared spectroscopy (FTIR). After UV exposure, peaks appeared at 3400 cm^{-1} and 1630 cm^{-1}(Figure 2.2e). The peak at 3400 cm^{-1} is associated with the formation of OOH/OH groups[35]. Previous studies have shown that the intensity of this peak increases with the addition of ethylene glycol to polyether mixtures[59]. The peak at 1630 cm^{-1} has been associated with the formation of additional C-O bonds[35]. The presence of these peaks strongly suggests the presence of PEO oxidative degradation products. No other new peaks or spectral shifts were observed.

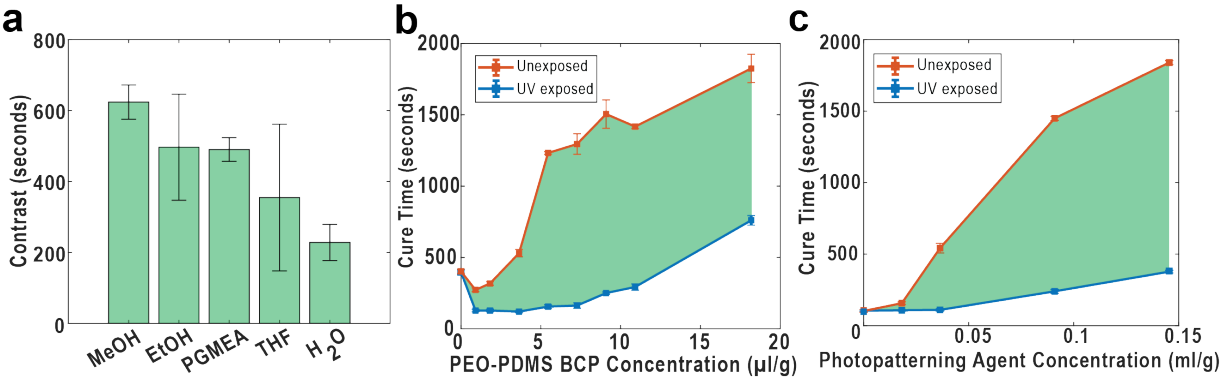

Figure 2.3: Characteristics of the photopatterning process using Sylgard 184. All ratios are measured relative to the mass of silicone liquid used to prepare the elastomer. (a) The contrast (contrast = unexposed solidification time - exposed solidification time, highlighted in green) was highly dependent on the solvent used to prepare the photopatterning agent. Methanol provided the greatest contrast. (b) A difference in cure time between exposed and unexposed samples was only observed when a fixed amount of $FeCl_3$ was added along with a variable amount of polyethylene oxide (PEO) polydimethylsiloxane (PDMS) copolymer (BCP). (c) As the concentration of the photopatterning agent increased, contrast improved. However, at concentrations greater than 0.15 ml/g, the silicone liquid thickened, making it difficult to uniformly mix in additional photopatterning agent.

Based on these results, we propose that UV exposure induces the reduction of Fe^{3+} to Fe^{2+} and the generation of chlorine radicals, which are quenched by hydrogen atom transfer with the PEO-PDMS copolymer. This reaction leads to the oxidative decomposition of PEO and decreases the ability of $FeCl_3$ to oxidize the Pt catalyst. This process explains the differential solidification rates observed between UV-exposed and unexposed regions of the silicone elastomer.

2.2.2 Photopatterning Agent Composition and Mixing Conditions Optimization

The composition of the photopatterning agent, the amount added to the silicone liquid precursors, and the method of mixing the agent with the silicone liquid are crucial factors that determine the contrast and, ultimately, the quality of the photopatterning. The photopatterning agent must contain both $FeCl_3 \cdot (H_2O)_6$ (to oxidize the platinum and initiate the photoreaction) and ethylene oxide (to neutralize the chlorine radicals). When $FeCl_3 \cdot (H_2O)_6$ and ethylene oxide

are added to a silicone liquid, they form an emulsion, as neither is soluble in silicone. The PEO-PDMS copolymer, dimethylsiloxane (60-70% ethylene oxide), was chosen for its ability to stabilize emulsions of polar compounds in silicone liquids [114] while also providing the necessary ethylene oxide. The interior of these emulsion droplets is yellow and contains the solvent and $FeCl_3$, while the PEO-PDMS copolymer concentrates at the interface between the silicone liquid and the droplet interior (Figure 2.2c-d).

The droplet size distribution of the $FeCl_3$-PEO-PDMS emulsion is a key factor in determining the contrast and resolution of the photopatterning process. However, accurately measuring the droplet size distribution was challenging due to the lack of a suitable dynamic light scattering system and the resolution limitations of our microscope. Consequently, our discussion of droplet size distribution is based on microscope observations, supplemented by conjectures related to the photopatterning agent's composition and mixing conditions. In general, emulsions with smaller droplets produced higher contrast and improved photopatterning resolution. We suggest that this is because the oxidation of Pt(0) by $FeCl_3$, as well as the photoreaction between $FeCl_3$ and PEO, occur at the droplet surface. A higher surface area-to-volume ratio (achieved with smaller droplets) would result in more interactions between $FeCl_3$, Pt(0), and PEO at the droplet surface, leading to greater contrast.

The size distribution of the photopatterning agent emulsion is influenced by both the composition of the photopatterning agent and the shear forces generated during mixing [115]. Higher shear forces lead to smaller droplet sizes [116]. Achieving the necessary shear forces required an apparatus capable of providing sufficient torque for high-speed mixing, especially given the relatively high viscosity of the silicone liquid precursors. To address this, we built an overhead mixing apparatus using a immersion blending tool (Figure D.1). We found that short mixing times (less than 30 seconds) at high speeds were critical for achieving good contrast and resolution. Longer mixing durations occasionally resulted in extended cure times and poor contrast. Although mixing with a hotplate and magnetic stir bar was possible, it required over 10

minutes and produced inconsistent, lower-quality photopatterning results due to the slow speed.

The optimization of the photopatterning agent composition involved four key parameters: first, the choice of solvent; second, the concentration of $FeCl_3$ in the solvent; third, the concentration of PEO-PDMS in the solvent; and fourth, the ratio between PEO-PDMS and $FeCl_3$. To simplify the optimization process, the total concentration of $FeCl_3$ in the solvent was fixed at approximately 0.1 g/ml. This concentration was chosen because it significantly extended the solidification time. Based on our droplet hypothesis discussed earlier, the ratio of $FeCl_3$ to PEO-PDMS and the droplet size distribution were considered the most critical factors in determining the contrast of the process.

Initially, tetrahydrofuran (THF) was selected as the solvent for the photopatterning agent. The THF-based agent was optimized for PEO-PDMS concentration (Figure D.3b) and the total amount of photopatterning agent added to the silicone liquid precursors (Figure D.3c). However, it was later discovered that THF also acted as an inhibitor in the solidification process. To test whether the choice of solvent influenced the contrast of the photopatterning process, THF was replaced with water (H_2O), methanol (MeOH), ethanol (EtOH), and propylene glycol methyl ether acetate (PGMEA) (Figure 2.2e). It was found that the contrast of the process was highly dependent on the solvent, with THF producing variable and ultimately inferior contrast compared to MeOH, EtOH, and PGMEA.

The contrast of the process likely depends on the solvent's effects on emulsion stability, reactivity, and the solidification mechanism. Solvent polarity directly influences the solubility of $FeCl_3$ and PEO-PDMS in the silicone precursor, while solvent surface tension affects the ability to form stable emulsions and uniform droplets. More polar solvents like methanol, ethanol, and water are less soluble in silicone liquid precursors than less polar solvents such as THF and PGMEA, which leads to more stable emulsions. However, the exceptionally high surface tension of water counteracts this effect, possibly resulting in larger droplet sizes. Additionally, the solvent's interaction with the metal salts is crucial. Water is known to strongly coordinate

with $FeCl_3$, and this interaction could interfere with the generation of chlorine radicals or the subsequent charge transfer chain they initiate[117].

Methanol was found to be the optimal solvent for the Sylgard 184 and Sylgard 527 photopatterning processes (Figure 2.3a). However, THF was still useful for its inhibitory effect in faster-curing silicones such as Ecoflex and Dragon Skin. The MeOH-based photopatterning agent was further optimized for PEO-PDMS concentration (Figure 2.3b) and the total amount of photopatterning agent added to the silicone liquid precursors (Figure 2.3c). These experiments determined that the optimal photopatterning agent composition was 4 parts methanol, 0.5 parts $FeCl_3$, and 0.5 parts PEO-PDMS copolymer by mass.

2.2.3 UV Exposure Process and Optimization

We found that the quality of the photomask image projected onto the silicone film, the exposure dose, and the thickness of the silicone film played a crucial role in determining the minimum feature sizes we could achieve. Most silicone liquids are not viscous enough to tolerate direct contact with a photomask, so patterning requires either a laser exposure system, projection lithography, or a method to reliably create a small separation between the substrate and the photomask. We opted for an inexpensive approach using transparency photomasks taped to a glass slide. To reliably create a small separation, we 3D-printed blocks with slots of varying depths for our substrates (Figure D.11). The substrates were placed in these slots, with the photomask positioned on top (Figure D.12). This method allowed us to reasonably control the distance between the substrate and the photomask. However, due to variations in the thickness of our glass substrates, there was substantial variation in the distance between the photomask and the substrate from sample to sample. The typical separation between the slide and the photomask was 100 μm ± 70 μm.

Reducing the gap between the photomask and the substrate, as well as using thinner silicone films, resulted in higher-quality features with better sidewall angles and more consistent

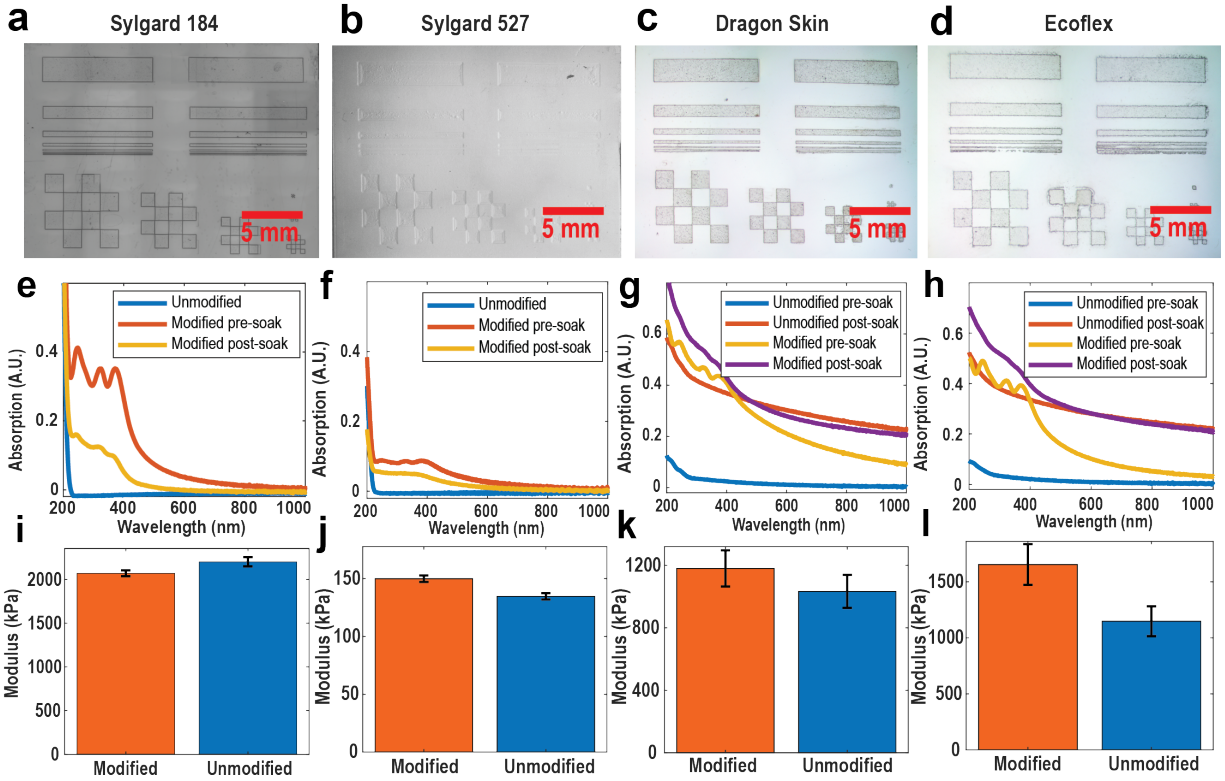

Figure 2.4: (a-d) Stitched optical microscopy images of patterned films, (e-h) optical transparency (UV-Vis), (i-l) and mechanical property (nanoindentation) data for each type of silicone. Unmodified samples are films of silicone elastomer without any added photopatterning agent. Modified (photopatternable) samples are films of silicone elastomer with the photopatterning agent. (a) Photopatterned Sylgard 184. (b) Photopatterned Sylgard 527. (c) Photopatterned Dragon Skin-10 Medium. (d) Photopatterned Ecoflex 00-30. (e) Sylgard 184 UV-Vis: No changes were observed in the unmodified samples after the IPA soak. (f) Sylgard 527 UV-Vis: No changes were observed in the unmodified samples after the IPA soak. (g) Dragon Skin 10 Medium UV-Vis: A significant change in optical transparency was observed after soaking in IPA. The samples became cloudy as excess silica in the formulation washed away. (h) Ecoflex 00-30 UV-Vis: A significant change in optical transparency was observed after soaking in IPA. The samples became cloudy as excess silica in the formulation washed away. (i) Sylgard 184 mechanical data: Nanoindentation showed a small difference in the modulus between the modified and unmodified samples. (j) Sylgard 527 mechanical data: Nanoindentation showed a small difference in the modulus between the modified and unmodified samples. (k) Dragon Skin 10 Medium mechanical data: Nanoindentation showed a small difference in the modulus between the modified and unmodified samples. (l) Ecoflex 00-30 mechanical data: Nanoindentation showed a more significant difference between these samples, likely due to uncrosslinked material washing out.

thicknesses (Figure D.4-10). These improvements are likely due to reduced diffraction effects and the lack of spatial coherence in our UV source, which caused the beam to diverge from the photomask windows. It is likely that a laser or projection lithography system could further improve the resolution.

The exposure dose also played a significant role in determining feature quality. Underexposure led to insufficient contrast, while overexposure resulted in oversized features and poor sidewall angles. We found that an exposure dose of 10 seconds with our 11.7 mW/cm² UV LED was sufficient for highly transparent silicones such as Sylgard 184 and Sylgard 527. This is approximately 1.6% of the exposure time used in previous studies, utilizing a more accessible wavelength of 365 nm[84, 68, 76, 83, 86]. The exceptional sensitivity of the films to UV makes this process suitable for use with maskless exposure systems and in high volume production. For more translucent silicones, such as Ecoflex and Dragon Skin, a dose of 30-40 seconds was necessary.

2.2.4 Post-Exposure Curing and Development Optimization

After optimizing the photopatternable silicone formulation and exposure conditions, we refined the curing process and the removal of uncrosslinked silicone liquid. Previous studies on silicone photopatterning have shown that diffuse heat and a selective solvent for the uncrosslinked silicone liquid are crucial for achieving high patterning resolution and steep sidewall angles[86]. Our findings were consistent with these results. Similar to other studies, using an oven to cure the samples and then methyl isobutyl ketone (MIBK) diluted in 2-propanol (IPA) to remove the uncrosslinked silicone produced good outcomes, but the results were inconsistent due to significant temperature variability in the oven and long development times with MIBK/IPA.

We found that, for most applications, samples could be solidified on a hotplate at 90°C, using an aluminum foil-covered glass petri dish as a cover. Depending on the thickness, the typical solidification times of exposed Sylgard 184 were from 40 seconds to two minutes and 30

seconds. The uncrosslinked silicone was then removed in a bath containing 50% ethyl acetate (EtAC) and 50% IPA. After the exposed silicone is solidified on the hotplate, samples were immediately submerged in the EtAC/IPA bath and agitated for at least 30 seconds. Two developer baths were used: the first to remove the bulk of the uncrosslinked silicone, and the second to remove any remaining residue and polish the surface. Finally, the samples were rinsed with IPA and dried with compressed air. This method, which used widely available processing tools and a fast-developing solvent, allowed us to produce better samples more consistently, as the shorter iteration times improved overall efficiency compared to the oven-based method.

2.2.5 Optical Properties

Many silicone formulations are highly valued for their optical transparency. However, incorporating the photopatterning agent leads to both yellowing and clouding of the elastomer. The yellowing is due to the added $FeCl_3$, while the clouding results from scattering by the droplets formed by the PEO-PDMS copolymer[118]. To minimize these effects, we sought to identify the lowest concentration of photopatterning agent that would still provide sufficient contrast for patterning. We found this threshold to be approximately 0.1 ml of photopatterning agent per gram of silicone liquid. Films produced at this concentration exhibited a slight yellow hue (Figure 2.4e-h). For dielectric gels such as Sylgard 184 and 527, this issue was mostly resolved by soaking the films in 2-propanol to remove excess $FeCl_3$ and PEO-PDMS (Figure 2.4e-h). However, this soak caused clouding in Dragon Skin and Ecoflex, regardless of whether the photopatterning agent was present (Figure 2.4g-h). The clouding is likely due to the high fraction of fumed silica used in these formulations, which compromises their solvent resistance.

2.2.6 Mechanical Properties

Hydrosilylation-based silicone elastomers are known for their remarkable tunability in mechanical properties, a critical feature in biological applications. It is well-established that the mechanical environment profoundly influences cell behavior, including survival, proliferation, adhesion, differentiation, and metabolism[119]. For example, studies have shown that cell migration and focal adhesion formation are regulated by substrate stiffness[120], while later research demonstrated that stem cell differentiation is directed by substrate stiffness, aligning with the elastic modulus of target tissues[121].

One of our primary goals in developing this photopatterning process was to maintain the simple and versatile tunability of silicone elastomer mechanical properties. Blends of Sylgard 184 and Sylgard 527 are known to cover a broad Young's modulus range, from 5 kPa to 1.27 MPa, matching the elastic moduli of many soft tissues, including neuronal and skeletal muscle tissues[122]. This tunability is essential for understanding how substrate mechanics influence various cellular processes, as cells in tissues such as the extracellular matrix (ECM) or arterial walls experience a wide range of stiffness.

We found that the local mechanical properties, as measured by nanoindentation, of our photopatternable formulations closely matched those of the unmodified silicones when processed under the same conditions (Figure 2.4e-h). This was particularly true for the clear dielectric gels, Sylgard 184 and 527, which retained their desirable mechanical characteristics after photopatterning. These results suggest that our process preserves the local elastic properties critical for biological applications, enabling researchers to probe the effects of the mechanical environment on cell behavior. In contrast, silica-heavy formulations such as Dragon Skin and Ecoflex exhibited greater variation in mechanical properties, likely due to the additional silica and uncrosslinked PDMS being washed out during the 2-propanol soak, leading to regions of increased stiffness.

To evaluate the global tensile properties of the formulations, films were prepared, and

water-assisted tensile testing was conducted (Figure D.13)[123]. All tested formulations became significantly softer after incorporating the photopatterning agent. Unmodified Sylgard 184 (10:1) exhibited an average elastic modulus of 748 kPa, while samples mixed with the photopatterning agent had an average modulus of 205 kPa. For modified Sylgard 184, the (5:1) ratio had an elastic modulus of 233 kPa, while the (20:1) ratio had an elastic modulus of 104 kPa. Dragon Skin's unmodified elastic modulus was 410 kPa, compared to 138 kPa for the modified formulation. Similarly, Ecoflex's unmodified modulus was 117 kPa, whereas the modified version measured 69.8 kPa. Both Sylgard 527 and Sylgard 184 (30:1) were too soft to be evaluated with our tensile testing apparatus. The reduction in elastic modulus suggests a lower crosslinking density in samples mixed with the photopatterning agent, potentially due to partial inhibition of the platinum catalyst or the formation of voids from the emulsion.

2.2.7 Microfluidic Applications

Embossing methods have made it easy to pattern silicone elastomers for microfluidic devices, leading to their widespread adoption in the field. However, as devices have become more complex, simple embossing methods are no longer sufficient. To demonstrate the applicability of our photopatterning process for microfluidics, we fabricated a single-layer device with lateral critical dimensions as small as 50 μm (Figure 2.5d). Our design was a flow-focusing device, commonly used in applications such as flow cytometry[124], pharmaceutical synthesis[125], and even computing[126]. The device generates a continuous stream of bubbles by using converging channels of air and water (Figure 2.4a).

The microfluidic chip was fabricated by photopatterning a 30 μm thick layer of Sylgard 184 onto a 25 mm x 75 mm glass slide (Figure 2.5a), followed by bonding an unmodified piece of Sylgard 184 on top. The device operated as expected, supporting high flow rates and air pressures (up to 1 ml/min of water and 15 psi of nitrogen) to produce a high-frequency stream of bubbles in the outlet channel (Figure 2.5e).

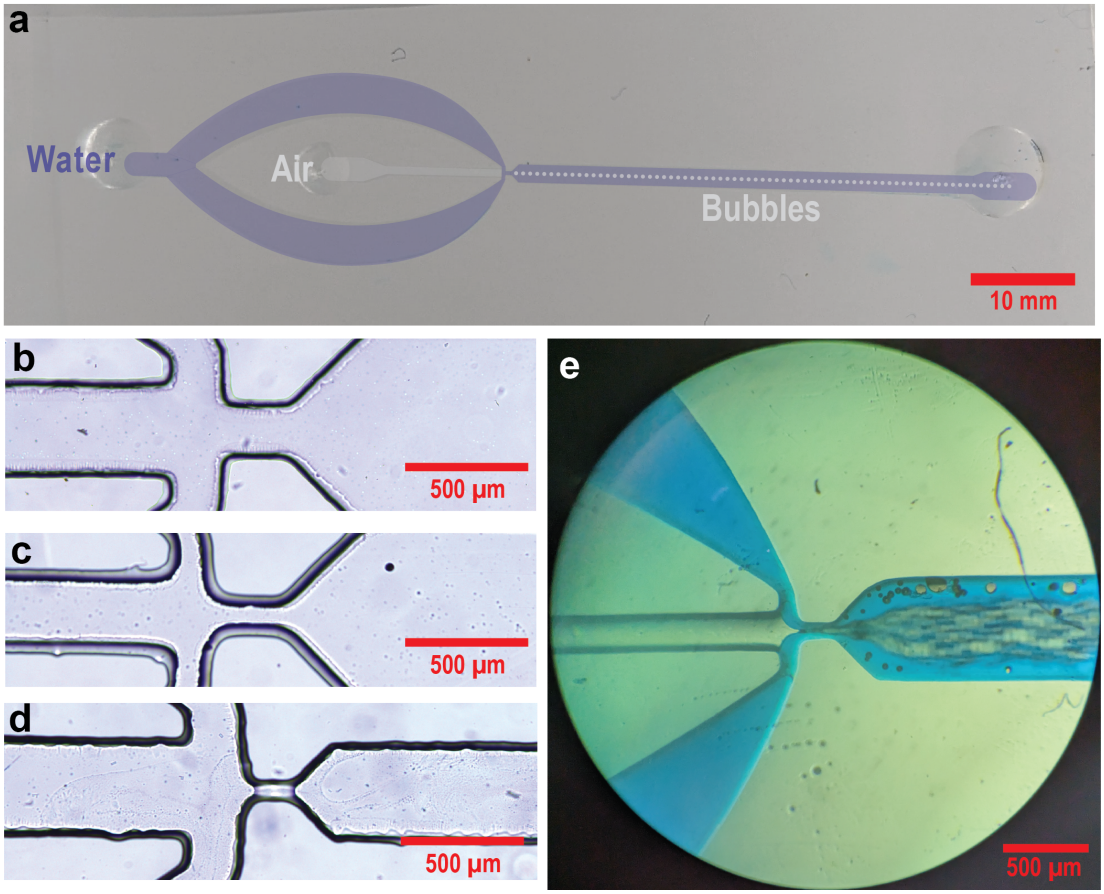

Figure 2.5: (a) Photograph of a microfluidic flow-focusing device fabricated using Sylgard 184 and our photopatterning agent. The liquid (blue) and gas (white) inlets, as well as the droplet formation region, are highlighted with a covered overlay. (b-d) Optical microscopy images of the flow-focusing junction with varying channel widths: (b) 200 μm, (c) 100 μm, and (d) 50 μm. (e) Optical microscopy image of the 100 μm channel generating an extremely high-frequency stream of bubbles.

2.2.8 Biocompatiblity

To evaluate the biocompatibility of Sylgard 184 modified with the $FeCl_3$-PEO photopatterning agent, we cultured U2OS cells on both modified and unmodified substrates and analyzed cell morphology, adhesion, and proliferation[127]. Prior to cell culture, both substrates were soaked in 2-propanol to remove any uncrosslinked silicone components and residual $FeCl_3$-PEO photopatterning agent. Key indicators of cell health, including cell shape, spreading, and colony formation, were used to determine whether the modification introduced any cytotoxic effects or altered cellular behavior. Healthy cells typically display a flattened, elongated morphology characteristic of adherent cells, with well-defined actin filaments and intact nuclei.

Fluorescence microscopy with DAPI and Phalloidin (A594) staining revealed no discernible differences between cells grown on the modified and unmodified Sylgard 184 substrates (Figure D 14). The presence of intact nuclei, indicated by uniform DAPI staining (blue), along with robust fluorescent signals from the actin filaments (red) in both conditions, suggests that the cells retained their structural integrity and were not adversely affected by the modification. Confluence, defined as the percentage of the surface area covered by adherent cells, reached 70-80% on both modified and unmodified substrates, indicating healthy cell proliferation and substrate compatibility.

Additionally, no signs of cell detachment or rounding -— both common indicators of cytotoxicity -— were observed on the modified samples. Taken together, these findings suggest that the incorporation of the $FeCl_3$-PEO photopatterning agent does not compromise the substrate's ability to support healthy cell attachment, proliferation, and morphology, making it suitable for biological applications that require patterned silicone elastomers with precise photodefinable features.

2.2.9 Cardiac Microphysiological Device Applications

With the high prevalence of heart disease and the pressing need for efficient preclinical evaluation of cardiac therapies[128], there is a strong demand for microphysiological systems that can support high-throughput assessment of drug efficacy and cardiotoxicity[129, 130]. Given the excellent biocompatibility of the $FeCl_3$-PEO photopatterning agent-modified Sylgard 184, we applied our photopatterning technique to fabricate a proof-of-concept cardiac microphysiological systems (MPS) based on muscular thin films. Traditional models, such as animal studies or large-scale tissue constructs, are often labor-intensive, costly, and fail to capture human-specific cardiac responses[131]. Cardiac MPS based on muscular thin films have emerged as a promising alternative, offering a platform for real-time evaluation of contractility, tissue health, and response to pharmacological agents[131]. To maximize the utility of these platforms, it is critical to develop scalable devices that allow parallelized measurements across multiple samples, thereby increasing throughput and statistical power in preclinical testing. This application of our photopatternable PDMS formulation aims to demonstrate its versatility in creating high-resolution, functional structures for bioengineering applications. Inspired by existing MPS systems[132, 133, 134, 135, 136, 137, 138], we designed a multi-well platform that integrates strain sensors for real-time measurements of contractile stress in engineered cardiac tissues.

Most current instrumented MPS devices are constructed using SU-8[139], a photoresist with high stiffness, or thick layers of PDMS[135]. These materials pose significant challenges for real-time contractility measurements because they require highly sensitive strain gauges or laser vibrometers to detect the low-magnitude deformations generated by muscle contractions. The need for these sensitive strain gauges not only complicates device fabrication but also limits scalability and increases production costs. In contrast, our photopatternable PDMS offers tunable, reliable mechanical properties that can be adjusted to match the stiffness and compliance of native cardiac tissues, making it an ideal choice for applications where mechanical mimicry is crucial[129, 130]. By carefully selecting the formulation and processing conditions, PDMS can be engineered to

provide precise, reproducible deformation profiles while maintaining biocompatibility.

A primary challenge in implementing PDMS-based cardiac MPS devices is achieving scalable and precise cantilever definition. Traditional methods, such as laser cutting or embossing, often suffer from poor resolution, thermal damage, or edge roughness that compromise the mechanical integrity and consistency of the cantilevers. These drawbacks can introduce unwanted variability in device performance, making it difficult to standardize experiments. Our photopatterning approach addresses these issues by providing a non-contact method to define cantilever geometries with high precision and reproducibility. This process enables the creation of complex, high-resolution features without the need for specialized equipment or post-processing, thus making it well-suited for scaling to high-density device arrays.

In our design, the device was constructed using a three-layer PDMS structure to form cantilevers capable of supporting contractile tissues while maintaining the mechanical properties required for accurate stress measurements(Figure 6a). The wells were defined by photopatterning a thin PDMS film to create four apertures matching the dimensions of a standard 96-well plate, which were then filled with a 3.5% dextran in water solution to serve as a water-soluble sacrificial layer for subsequent PDMS release. The first PDMS layer (2.5 μm thick) formed the base of the cantilever and served as the foundation for the integrated strain gauges. Gold-plated silver nanowires were spray-coated onto this base layer due to their biocompatibility and chemical stability, ensuring consistent performance in culture conditions[140, 141]. Silver epoxy was then applied to create conductive contacts at the ends of the strain gauges, enabling precise electrical readout of the bending strain during muscle contraction.

The final structural layer of PDMS (12.5 μm thick) was photodefined to encapsulate the strain gauges and complete the cantilever structure. The entire assembly, supported on a glass slide, was adhered to a custom-designed printed circuit board (PCB) using silver epoxy to establish electrical connections, and NOA 81 optical adhesive to seal the device. The 3D-printed and SU8 encapsulated culture wells were then mounted on the top of the PCB using NOA 81,

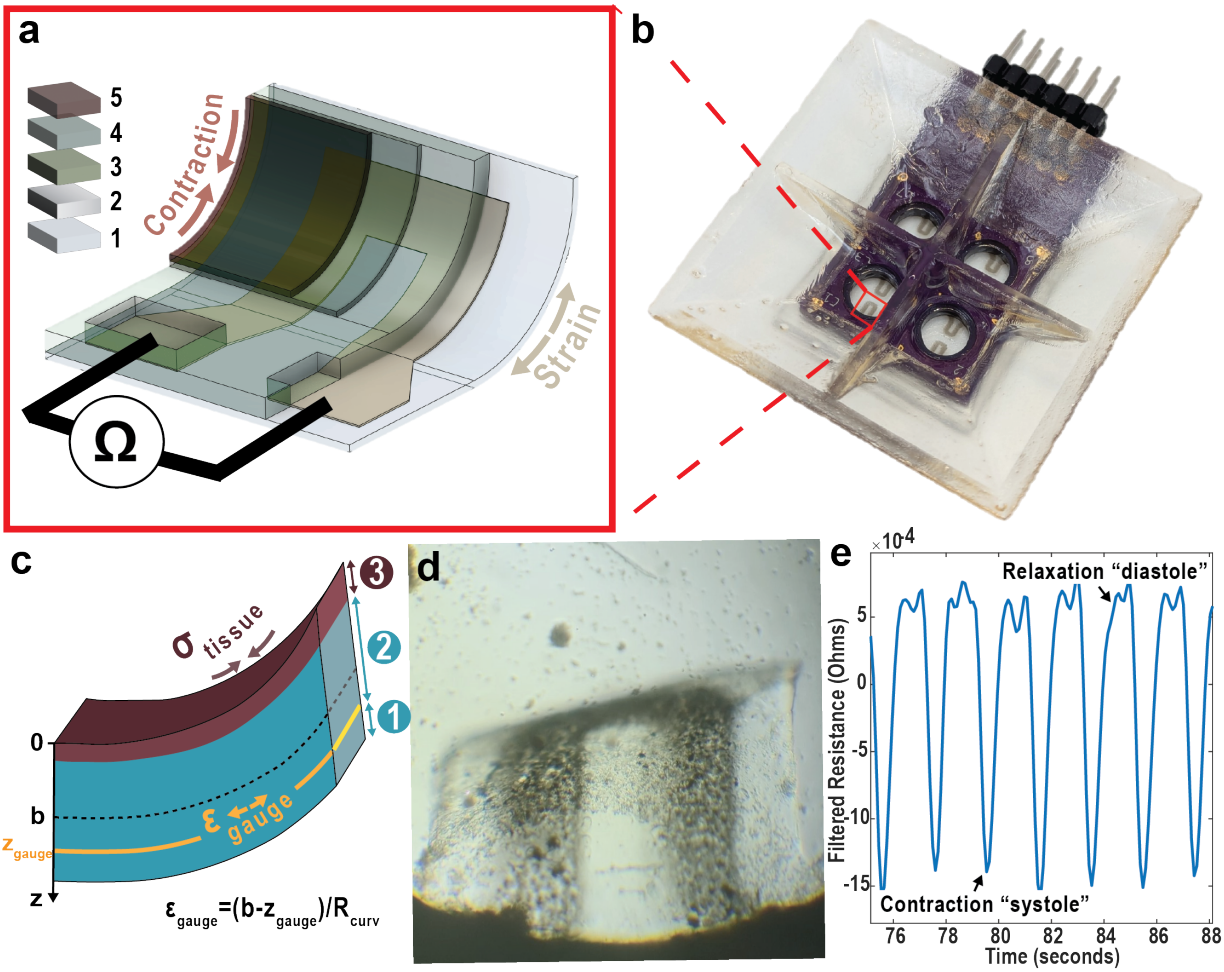

Figure 2.6: (a) Cross-sectional schematic of the photopatterned silicone cantilever used to measure the contractility of hIPSC-derived cardiomyocytes. The device consists of: (1) an initial 2.5 μm thick layer of photopatterned silicone, (2) a strain gauge formed by spray-coating gold-plated silver nanowires, (3) a second 12.5 μm thick layer of photopatterned silicone, (4) a fibronectin layer to facilitate cell adhesion, and (5) a monolayer of hIPSC-derived cardiomyocytes. (b) Photograph of the complete device. (c) Schematic cross-section of a mechanical model of the cantilever, showing (1) the initial 2.5 μm thick PDMS layer, (2) the second 12.5 μm thick PDMS layer, and (3) the hIPSC-derived cardiomyocyte microtissue. The strain gauge, depicted in gold, experiences a strain described by Stoney's equation, where b is the position of the neutral axis, and R_{curv} is the radius of curvature of the neutral axis. (d) Optical microscopy image of the moving cantilever with the hIPSC-derived cardiomyocyte microtissue (see Supplementary Video 1). (e) Processed resistance versus time data from the gold-plated silver nanowire strain gauge during cardiomyocyte contraction. Raw data and processing details are provided in the Supplementary Information.

providing a stable environment for cell culture and experimental testing. See Figure D.13 for photos of the fabrication process.

Prior to cell seeding, the assembled devices were soaked in 2-propanol to remove any uncrosslinked PDMS or residual $FeCl_3$-PEO photopatterning agent. After drying, the surfaces underwent brief air plasma exposure to improve cell adhesion. The devices were then incubated with fibronectin, a key extracellular matrix protein, to further enhance cell attachment and support a healthy microenvironment for cardiac tissue formation. Human induced pluripotent stem cell-derived cardiomyocytes (hIPSC-CMs) purchased from Celogics were cultured at a density of 468,750 cells/cm^2 (150,000 cells per well) and subsequently seeded onto the cantilevers to adhere and mature.

Cell viability and contractile activity were assessed one, two, five, and nine days post-seeding. Resistance readings from the cantilevers were taken on days two and five. Viable cells were observed in all 22 wells used. By day two, several wells displayed beating cells, and by day three, some wells had developed vigorously beating monolayers, producing visible cantilever movement. One cantilever with a robust culture and functioning sensor was monitored on day three (Supplementary Video 1), and resistance vs. time data was recorded (Figure 6e). By day five, all 22 wells had beating cardiomyocyte monolayers. However, by day nine, the fraction of beating wells had reduced to 36%, with a notable decline in contractility.

This platform demonstrates that our photopatternable PDMS process can be successfully adapted to create complex, functional cardiac MPS constructs. With some optimization, the approach could be scaled up to fabricate high-density MPS arrays, significantly increasing throughput and statistical power for drug screening and disease modeling applications. The integration of strain gauges provides a unique advantage, eliminating the need for traditional optical tracking and enabling real-time electrical readouts that are better suited for high-throughput studies. However, we were unable to extract the shear stress generated by the contraction of cells on the surface of the cantilever, as the current design does not incorporate alignment structures

needed to guide cell orientation and alignment. This limitation can be addressed by adding surface topographies or chemical patterning to direct cellular organization. Future studies will focus on optimizing the photopatterning process to create such alignment structures, enabling a more complete assessment of the mechanical forces generated by cardiac tissues. Despite this limitation, our results position PDMS as a superior material for constructing cardiac microphysiological systems with tunable mechanical properties and reproducible results.

2.3 Conclusion

The photopatternable PDMS formulation presented here enables reliable, high-resolution patterning of silicone elastomers using accessible processing conditions and commercially available components. This technique is readily applicable to a broad range of biomedical devices, including wearable sensors, complex microfluidic systems, and instrumented tissue platforms. The capability for scalable, precise patterning of PDMS structures with integrated strain gauges and biocompatible interfaces makes this approach especially valuable for high-throughput screening platforms, where real-time, non-optical readouts are essential.

Further refinements could extend this method to more advanced tissue engineering applications. Achieving precise control over droplet size distributions in the photopatterning agent emulsion—potentially through high-shear dispersers—and optimizing the selection of PEO-PDMS emulsifiers and solvents could enhance contrast and enable the fabrication of complex patterning geometries, such as cell alignment structures. These improvements could facilitate the creation of sophisticated microphysiological systems that promote directed cell growth, better replicating native tissue architecture and enhancing the fidelity of in vitro models. Ultimately, these advancements would position this method as a transformative tool in the development of organ-on-chip platforms and engineered tissue constructs.

2.4 Acknowledgments

This chapter is submitted for publication in Advanced Materials as ”A Simple Method for Photopatterning Commercial PDMS Using an Off-the-Shelf Photodeactivated Hydrosilylation Inhibitor,” co-authored with Noel Sebastien D. Mallari, Qinyu Liang, Leah Sadr, Dhivya Meganathan, Anum Tahir, Lisa Tang, Jacqueline Lampert, Marc Levy, Wade Shipley, Hannah E. Fishman, Tarek Rafeedi, Rafael A. Montalvo, Abdulhameed Abdal, Tse Nga Ng, Jinhye Bae, Andrea Tao, Nathan Romero, Zeinab Jahed, and Darren J. Lipomi. I was the primary investigator and author of this material.

Appendix A

Materials and Methods for Photography-Inspired Patterned Vapor Phase Polymerization of Conductive PEDOT on Rigid and Stretchable Substrates

A.1 Materials

N-[3-(trimethoxysilyl)propyl]aniline (AnPTMS), iron(III) chloride, 3,4-Ethylenedioxythiophene (EDOT), poly(ethylene oxide)-block-poly(propylene oxide)-block-poly(ethylene oxide) MW 5800 (PEO-PPO-PEO, Pluronic P-123), benzophenone, Irgacure 2959, anhydrous 2-methoxyethanol, isopropanol, 1-Ethyl-3-methylimidazolium ethyl sulfate (EMIM-ES), 2-hydroxyethyl cellulose, polypyrrole, and phosphate-buffered saline (Gibco pH 7.4 1x) were acquired from Sigma-Aldrich at ACS grade or higher purity.

Iron(III) p-toluenesulfonate was purchased from AK Scientific at 98% purity due to issues arising from the lower purity of the initially purchased technical grade material from Sigma-Aldrich. Iron(III) nitrate, iron(III) bromide, and silver nitrate were sourced from Fisher Scientific at ACS purity. Poly(3,4-ethylenedioxythiophene) polystyrene sulfonate (PEDOT:PSS) was obtained from Heraeus as Clevios PH:1000. Sodium hydroxide and methane sulfonic acid were sourced from Acros Organic, also at ACS Purity. Cyclohexanone was purchased from Tokyo Chemical Industries at 99

Polyethylene terephthalate (PET) sheets were purchased from CalPalmy, with indium tin oxide (ITO) coated PET obtained from Qunguan. The thermoplastic polyurethane (TPU) filament was purchased from Overture, and NOA 81 was purchased from Norland Products. 25 mm x 25 mm quartz slides (185 - 2500 nm, 90+% transmission) were acquired from Cuvet.co, and 25 mm x 25 mm soda lime glass slides were purchased from Biotain. Photomasks were obtained from Fineline Imaging, and laser temporary tattoo paper was purchased from Papilio. Silicone Oil (DMS-T03) was purchased from Gelest, and Sylgard 184 polydimethylsiloxane (PDMS) was acquired from Dow Chemical Company. Scotch Magic Tape was obtained from Scotch. Unless otherwise stated, all materials were used without further purification.

A.2 Methods

A.2.1 Iron(III) Methanesulfonate Synthesis

The synthesis of iron(III) methanesulfonate involved the substitution of chlorine in iron(III) chloride with methanesulfonate. Silver chloride was precipitated through the reaction between silver methanesulfonate and iron(III) chloride. The detailed procedure is as follows:

To prepare silver methanesulfonate, 10 g of silver nitrate was dissolved in deionized water, combined with 1 M sodium hydroxide, leading to the precipitation of silver oxide. The solution underwent titration with sodium hydroxide until no further precipitate was observed. The resulting silver oxide precipitate was then filtered, thoroughly washed with water, and dried.

Following this, the dried silver oxide was introduced into a reaction vessel with water, and drops of pure methanesulfonic acid were added until complete conversion to silver methanesulfonate. Subsequently, a solution of 1 M iron(III) chloride in water was prepared. This iron(III) chloride solution was then added dropwise to the silver methanesulfonate solution until no additional white precipitate was observed.

The precipitate was separated through filtration, and the product solution was concentrated with rotary evaporation. The remaining iron(III) methanesulfonate solution was frozen with dry ice and further processed in a Labconco Freezone lyophilizer to eliminate the remaining solvent. For the final purification step, samples of the dried iron(III) methanesulfonate were dissolved in 2-methoxyethanol and filtered to ensure the removal of any residual precipitate or impurities.

A.2.2 Iron(III) P-toluenesulfonate Chloride Impurity Removal

To eliminate chloride impurities from iron(III) p-toluenesulfonate, 3 g of the compound was dissolved in 50 ml of water. Subsequently, a 0.1 M solution of silver nitrate was employed to titrate the iron(III) p-toluenesulfonate solution. As silver chloride precipitates as a white solid in the solution, silver nitrate was added dropwise until no further white precipitate was observed.

The resulting precipitate was then filtered off, and the residual solution underwent rotovapping to remove the majority of the water. The remaining iron(III) p-toluenesulfonate solution was further processed by freezing with dry ice and subjected to a Labconco Freezone lyophilizer to eliminate the remaining solvent.

A.2.3 Standard Substrate Cleaning Procedure

Substrates underwent a cleaning process involving a 10-minute immersion sonication in deionized water with the surfactant Alconox, followed by a rinse in DI water. Subsequently, they were sonicated for 10 minutes in acetone, followed by another round of sonication in IPA. Unless specified otherwise, the materials were then subjected to air plasma (30 W, 300 mTorr) in a Harrick Plasma PDC-001 for 10 minutes.

A.2.4 Oxidant Solution Preparation

The solutions utilized for spin-coating oxidant films were prepared in aluminum foil-covered glass vials to prevent exposure to light. The preparation process for all solutions commenced with the addition of 5 parts of 2-methoxyethanol to 1 part of Pluronic P-123 by mass into the vial.

For solutions comparing the photoactivity of iron salts, the subsequent step involved adding 1 part by mass of one of the following iron salts: iron(III) chloride, iron(III) nitrate, iron(III) bromide, iron(III) methanesulfonate, and purified iron(III) tosylate.

To investigate the importance of iron(III) reduction in the films vs. radical generation, we attempted to selectively deactivate oxidant films using “type 1” and “type 2” photoinitiators. Type 1 photoinitiators undergo unimolecular cleavage, while type 2 species undergo bimolecular reactions to generate radicals. Solutions combining PEO-PPO-PEO, Fe(OTs)3, and the photoactive compound were prepared with type 1 photoinitiators, such as Irgacure 2959, and the type 2

photoinitiator benzophenone. Despite using a high-power broad-spectrum UV source, none of these solutions demonstrated an enhancement in patterning compared to pure Fe(OTs)3. These experiments provided evidence against a mechanism that was purely radical mediated or based on hydrogen abstraction.

In the case of solutions investigating the enhancement of photopatterning through the addition of a radical initiator, the preparation included adding 1 part by mass of Fe(OTs)3 and 0.15 parts of Irgacure 2959 or 1 part benzophenone.

Solutions containing both iron(III) tosylate and iron(III) chloride were prepared by adding iron(III) p-toluenesulfonate and iron(III) chloride in such proportions that their total mass equaled 1 part in the overall oxidant solution. For instance, our standard oxidant solution consisted of 5 g of 2-methoxyethanol, 1 g of Pluronic P-123, 0.85 g of Fe(OTs)3, and 0.15 g of FeCl3.

A.2.5 Oxidant Film Preparation

Unless stated otherwise, oxidant films were prepared by spin-coating 300 μL of the oxidant solution onto 25 mm x 25 mm glass slides that were previously treated with AnPTMS. Before deposition onto the substrate using the window method, the solution underwent filtration through a 0.4 μm Teflon syringe filter.

The samples were spun at 1500 rpm for 30 seconds with a ramp rate of 1250 rpm/second. After removing them from the spin coater, the back was wiped on a clean paper towel. Subsequently, the slide was covered and placed on a hotplate at 80°C for 2 minutes to remove the majority of the solvent. The hotplate was equipped with an aluminum heat spreader to ensure uniform baking.

Following the baking step, samples were promptly transferred to the UV chamber for photopatterning. This entire process took place in an environment with minimal light to prevent undesired UV exposure.

A.2.6 UV LED Intensity Measurement

The intensity of the UV LED was measured by positioning it 10 cm away from a Newport 2936R power meter, which was equipped with a Newport 7167571580 photodiode.

A.2.7 Oxidant Film Photopatterning

Samples possessing oxidant films were moved to a custom-built UV exposure chamber. Subsequently, a custom polyethylene photomask obtained from Fineline Imaging was positioned on the samples. To ensure good contact, a 2" x 3" soda-lime glass slide was placed on top of the sample and photomask. Unless specified otherwise, samples were exposed for 10 seconds.

After exposure, the photomask was removed, and the samples were transferred to an aluminum foil-covered box. They were left in this box for no more than 20 minutes before being transferred to a vacuum oven for PEDOT polymerization.

A.2.8 X-ray Photoelectron Spectroscopy

X-Ray Photoelectron Spectroscopy (XPS) measurements were performed on a Kratos Axis Ultra DLD instrument with an aluminum anode to produce monochromatic K radiation with energy 1486.6 eV. Samples were prepared according to section (Oxidant Film Preparation) and secured onto the XPS sample holder using metal clips. Survey scans were first performed over the voltage range of 0-1200 eV followed by narrow high-resolution scans from 700-740 eV around the Fe2p peaks. High-resolution scans from the exposed and unexposed regions of a single sample were compared in Figure 3c. Tougaard's method was used for background corrections using a polymer loss function1.

A.2.9 UV/Vis Spectroscopy

The Cary 60 UV-Vis spectrophotometer from Agilent was utilized for the qualitative assessment of Fe3+ complexes within the oxidant films. All samples were prepared on quartz slides, following the standard substrate cleaning procedure detailed above. A clean bare quartz slide was employed to collect baseline data. The UV-VIS range settings were configured to cover 200 nm - 800 nm, and the scan controls were set to survey.

Using a standard oxidant solution as described in the Oxidant Solution Preparation Section, an oxidant film was prepared on quartz slides following the procedure outlined in the Oxidant Film Preparation Section. The first sample prepared remained unexposed and was then measured in the UV-Vis. Clear peak wavelengths at 320 nm and 360 nm were observed, indicating the presence of higher order Fe3+ complexes.

The second sample followed the same oxidant film preparation procedure but was exposed in the UV exposure chamber for 12 seconds. During this exposure procedure the sample was covered with a glass slide. After the exposure time, the sample was left to sit for 1 minute with the glass slide still covering it. Then, the sample was measured in the UV-Vis. This process was repeated, with each subsequent sample being exposed for an additional 12 seconds compared to the previous one, until a 60-second exposure was reached. For example, the third sample was exposed for 24 seconds, and the fourth for 36 seconds. As the exposure time increased, the peak wavelengths at 320 nm and 360 nm diminished and became less pronounced.

A.2.10 Vacuum Vapor Phase Polymerization

The polymerization step was conducted by placing the samples with patterned or unpatterned oxidant films into a Fisher 281A vacuum oven. The oven temperature was preheated to 35ºC. On several clean glass slides at the bottom of the oven, 24 μL of EDOT was evenly distributed. Samples were positioned on the top shelf of the oven, as close to the center as

possible. A static vacuum of -29.5 in.Hg was then applied. The samples were left in the oven for 30 minutes. After removal, they were immersed in a bath of clean isopropanol to eliminate the excess oxidant.

A.2.11 N-[3-(trimethoxysilyl)propyl]aniline CVD on Glass

25 mm x 25 mm glass slides were cleaned using the standard procedure. Subsequently, the slides were promptly transferred to a Fisher 281A Vacuum Oven preheated to 90º C. The samples were left under active vacuum for at least 15 minutes before introducing 20 μL of N-[3-(trimethoxysilyl)propyl]aniline to the chamber. Vacuum was then immediately applied to the oven, and the samples were left in the chamber for 1 hour. Following this, the slides were taken out from the oven and stored in a nitrogen glovebox before use.

A.2.12 N-[3-(trimethoxysilyl)propyl]aniline Deposition on PDMS

PDMS was prepared by blending 10 parts of Sylgard 184 base with one part crosslinker. The mixture was then degassed in a desiccator under active vacuum for 20 minutes. For the stickers, PDMS was either spin-coated onto laser printer tattoo paper, or drop-casted in a polystyrene petri dish for the tape test, stress vs. strain, and the stretched film images.

The PDMS was cured by placing it in an oven at 80°C for one hour. To introduce silanol groups, the PDMS was exposed to air plasma (30 W, 300 mTorr) in a Harrick Plasma PDC-001 for 3 minutes. Following this, samples were removed and immediately placed on an 80°C hotplate. They were then covered with pure N-[3-(trimethoxysilyl)propyl]aniline and left for 30 minutes. The excess N-[3-(trimethoxysilyl)propyl]aniline was subsequently washed away with isopropanol. The functionalized PDMS substrates were dried with compressed air and used immediately.

A.2.13 PEDOT on PDMS Preparation

The standard oxidant solution was spin-coated onto the PDMS samples, both with and without N-[3-(trimethoxysilyl)propyl]aniline. Subsequently, they were baked on a hotplate at 80°C for five minutes, considering the lower thermal conductivity of PDMS. For samples intended for the tape test, sticker, or stretching images, a thin layer of silicone oil was spun onto them to serve as a barrier to oxygen diffusion and aid in the release of the photomask. Following this, the samples were patterned, and the patterned ones were rinsed with hexanes to eliminate the silicone oil before polymerization. Vacuum vapor-phase polymerization was then carried out for all samples using the same procedure as before.

A.2.14 Scotch Tape Peel Off Test

Strips of Scotch magic tape were applied to samples of PEDOT on PDMS, both with and without N-[3-(trimethoxysilyl)propyl]aniline. The tape was left in place for 1 hour to ensure full adherence to the samples. Subsequently, the strips of tape were carefully peeled back from the surface of the samples. Photos were captured both before and after the peeling process.

A.2.15 Ultrasonication Abrasion Test

The abrasion tests began by preparing PEDOT:PSS films of similar thickness to the VPP PEDOT. To prepare these samples, 25 mm x 25 mm glass slides underwent the standard substrate cleaning procedure above.

Samples of PEDOT:PSS were spin-coated on these cleaned slides at 3000 rpm (with a 2000 rpm/second ramp) to form PEDOT:PSS films. The films were scored, and their thickness was measured using a Dektak Xt stylus profilometer. Following this, 25 mm x 25 mm squares were cut from a roll of 24 μm thick aluminum foil.

To perform the abrasion tests, the PEDOT:PSS samples, patterned PEDOT on glass with

N-[3-(trimethoxysilyl)propyl]aniline, and the aluminum foil squares were placed in a staining vial filled with phosphate-buffered saline and sonicated for four hours in a Branson 3510 bath sonicator. Photos were taken both before and after sonication.

A.2.16 PEDOT Film Sheet Resistance and Conductivity Measurements

The sheet resistance of unpatterned films was determined using a custom four-point probe connected to a Keithley 2400 sourcemeter. Four measurements were taken at different points in the film and subsequently averaged. To measure the thickness of the films, they were scored in four locations using the back of a razor blade, and the distance from the glass to the top of the film was measured using a Dektak XT profilometer.

The sheet resistance was calculated using the formula , where C represents the geometry correction factor2. For our samples, C was determined to be 0.94975. The conductivity was then calculated as .

A.2.17 PEDOT Film Thickness Measurements

The thickness of the PEDOT films was determined using a Dektak XT stylus profilometer. A 5 μm stylus, applying a 3 mg force, was utilized to obtain distance traces. Subsequently, the Bruker software was employed to average the trench depth and calculate the film thickness.

A.2.18 Electrochromic Display Fabrication

The fabrication of the electrochromic display commenced with the 3D printing of spacers from TPU. These spacers measured 25 x 25 millimeters, with 3 mm borders and a thickness of 2 mm. They featured a small gap along one edge. Subsequently, we cut and thoroughly cleaned both blankets and ITO-covered PET films, along with 1.5” x 1” glass slides, using the same procedure as before for the glass slides.

The next step involved preparing a 7.5% dextran solution in DI water. This was achieved by adding 0.75g of dextran to 10g of water and spin coating it at 1000 rpm for 40 seconds onto the 1" x 1.5" glass slides. It was essential to ensure the cleanliness of the spin coater and tweezers used during the spin coating process. To add additional texture and enhance the adhesion of the PEDOT film, the dextran was treated with a BD-20AC laboratory corona treater.

The process continued with PEDOT deposition. An oxidant film was deposited onto both the glass with dextran and the bottom layer of PET (no ITO) using the procedure outlined above. All samples were then exposed to EDOT vapors for 30 minutes at 35°C, followed by washing away the excess oxidant.

A polypyrrole film was then deposited onto the patterned PEDOT film.. To achieve this, the standard oxidant solution was spin-coated onto the patterned substrate. . It was then baked at 80ºC for 2 minutes and carefully patterned for pyrrole deposition.The samples were then exposed to pyrrole vapors by placing them under the lid of a desiccator with 24uL of pyrrole for 20 minutes. Subsequently, we rinsed away the oxidant layer, leaving the film patterned with both PEDOT and pyrrole. A polystyrene support layer was then spin-coated onto the film.

The polystyrene solution was created by adding 1 g of polystyrene to 10 g of cyclohexanone, mixing until the polymer was fully dissolved. This solution was then spin-coated on the PEDOT pyrrole film at 3000 rpm (1250 rpm / sec ramp). The solvent was removed by baking the samples at 120°C on a hotplate for 1 minute.

The patterned PEDOT and polypyrrole film was transferred to the ITO PET by first scoring around the edges of the slide with a razor blade. The edge of the slide was then immersed in water to start dissolving the dextran sacrificial layer. Once the film was fully removed from the slide, it was transferred to the ITO PET. The polystyrene support layer was removed by rinsing the sample with toluene.

We attached the dielectric spacer to the PET with NOA 81 optical adhesive. The top layer (patterned side of the device) was then attached to the spacer with NOA 81. The gap between

the patterned and unpatterned films was filled with the prepared electrolyte using a syringe. The electrolyte comprised 1-Ethyl-3-methylimidazolium ethyl sulfate (EMIM ES) as the ionic liquid and 2-hydroxyethyl cellulose (2-HEC) as a binder. Precautions were taken to prevent air pockets by leaving a hole in the spacer and filling the cavity with electrolyte after adhering to the top layer and slowly filling the spacer. A plug was then inserted into the spacer and glued using NOA on the outside edge.

The device was tested by applying 3 V to either the patterned or unpatterned electrode using a standard laboratory benchtop power supply.

Figure S1: Optical microscopy images showing the evolution of the oxidant film with UV exposure dose. This experiment was performed with a sample consisting of pure FeCl3 and PEO-PPO-PEO.

Figure S2: UV-vis absorbance spectra obtained from thin films on spectroscopic quartz substrates. a) UV-Vis absorbance measurement for pure Pluronic P-123 PEO-PPO-PEO block co-polymer. b) UV-vis spectrum for pure FeCl3 before and after 60 seconds of 365 nm UV exposure. The changes in absorbance at 320 and 360 nm for pure FeCl3 were much smaller than for samples containing PEO-PPO-PEO. This is expected since no photopatterning has been observed in samples of pure FeCl3 c) Uv-vis spectrum of pure Fe(OTs)3 before and after exposure to 365 nm UV light.

Figure S3: X-ray photoelectron spectroscopy data of the Fe 2p peak with fitting results for a) unexposed and b) exposed oxidant films consisting of FeCl3 and the Pluronic P-123 PEO-PPO-PEO block co-polymer.

Figure S4: X-ray photoelectron spectroscopy data of the Fe 2p peak with fitting results for a) unexposed and b) exposed oxidant films prepared with our ‘standard’ oxidant solution.

Appendix B

Additional Figures and Data for Photography-Inspired Patterned Vapor Phase Polymerization of Conductive PEDOT on Rigid and Stretchable Substrates

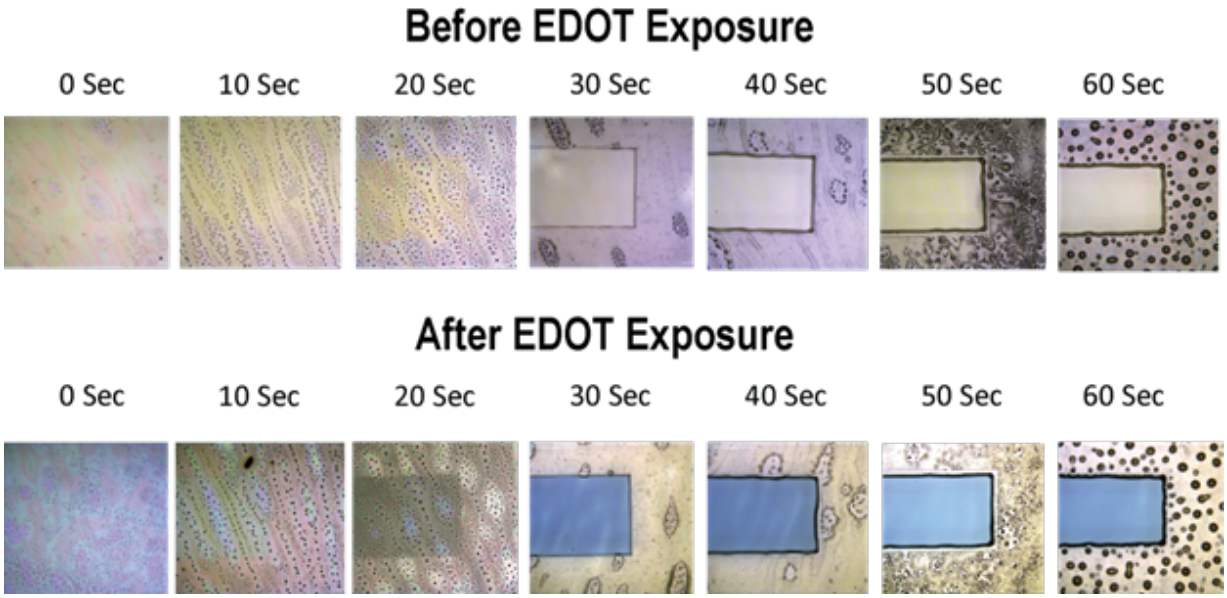

Figure B.1: Optical microscopy images showing the evolution of the oxidant film with UV exposure dose. This experiment was performed with a sample consisting of pure FeCl3 and PEO-PPO-PEO.

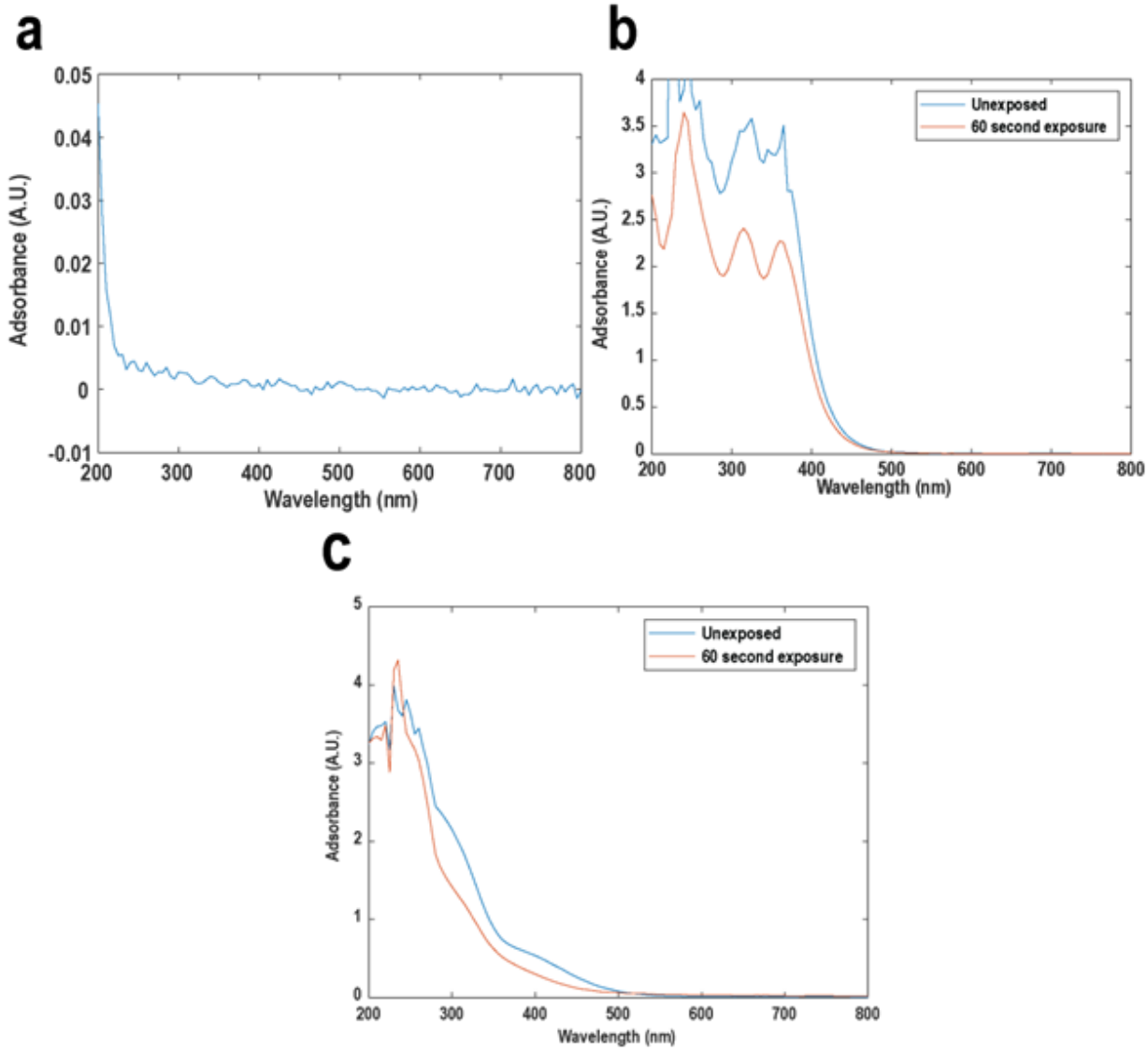

Figure B.2: UV-vis absorbance spectra obtained from thin films on spectroscopic quartz substrates. a) UV-Vis absorbance measurement for pure Pluronic P-123 PEO-PPO-PEO block co-polymer. b) UV-vis spectrum for pure FeCl3 before and after 60 seconds of 365 nm UV exposure. The changes in absorbance at 320 and 360 nm for pure FeCl3 were much smaller than for samples containing PEO-PPO-PEO. This is expected since no photopatterning has been observed in samples of pure FeCl3 c) Uv-vis spectrum of pure Fe(OTs)3 before and after exposure to 365 nm UV light.

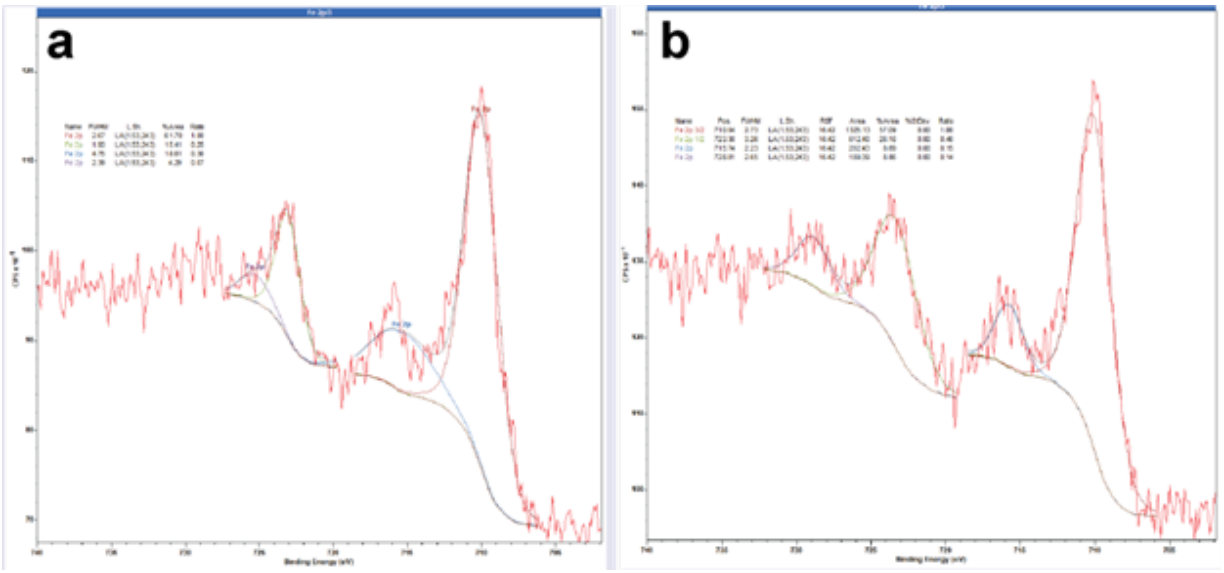

Figure B.3: X-ray photoelectron spectroscopy data of the Fe 2p peak with fitting results for a) unexposed and b) exposed oxidant films consisting of FeCl3 and the Pluronic P-123 PEO-PPO-PEO block co-polymer.

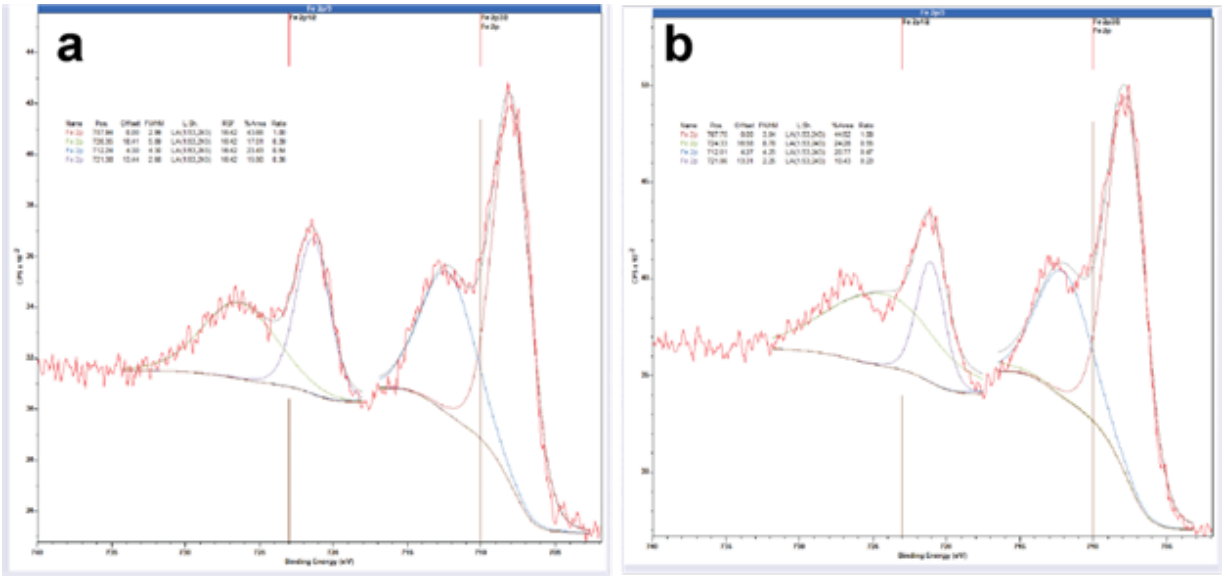

Figure B.4: X-ray photoelectron spectroscopy data of the Fe 2p peak with fitting results for a) unexposed and b) exposed oxidant films prepared with our 'standard' oxidant solution.

Appendix C

Materials and Methods for A Simple Method for Photopatterning Commercial PDMS Using an Off-the-Shelf Photodeactivated Hydrosilylation Inhibitor

C.1 Materials

C.1.1 Chemicals and Reagents

Iron(III) chloride hexahydrate ($FeCl_3$, puriss. p.a., reag. Ph. Eur., ¿99%) - Sigma-Aldrich, Methanol (MeOH) - VWR Life Science, Ethanol (EtOH) - Sigma-Aldrich, Propylene glycol methyl ether acetate (PGMEA) - Sigma-Aldrich, Dextran (Leuconostoc spp., M_n 100,000) - Sigma-Aldrich, Tetrahydrofuran (THF, unstabilized, HPLC grade) - Spectrum Chemical Mfg. Corp., Sodium chloride (NaCl, 99.0%) - Fisher Scientific, Sodium hydroxide (98.7%) - Fisher Scientific, Silver nitrate ($AgNO_3$, ¿99.9999%) - Sigma-Aldrich, Polyvinylpyrrolidone (PVP, MW 55,000) - Sigma-Aldrich, Anhydrous ethylene glycol (99.8%) - Sigma-Aldrich, Gold(III) chloride hydrate (99.995%) - Sigma-Aldrich, Anhydrous sodium sulfite (98-100%) - Alfa Aesar, L-(+)-ascorbic acid (99+%) - Alfa Aesar,

C.1.2 Silicones and Polymers

Dimethylsiloxane-(60-70% ethylene oxide) block copolymer (PEO-PDMS BCP, 20 cSt) - Gelest, Sylgard 184, Sylgard 527 - Dow Chemical Company, Ecoflex 00-30, Dragon Skin 10 Medium - Smooth-On, Poly(dimethylsiloxane), vinyl-terminated (M_n 25,000) - Sigma-Aldrich, Poly(dimethylsiloxane-co-methylhydrosiloxane), trimethylsilyl-terminated (M_n 950, methylhydrosiloxane 50 mol%) - Sigma-Aldrich, Poly(methylhydrosiloxane) (average M_n 1,700 - 3,200) - Sigma-Aldrich, Platinum(0)-1,3-divinyl-1,1,3,3-tetramethyldisiloxane complex in xylene (Pt 2%) - Sigma-Aldrich, Platinum-divinyltetramethyldisiloxane complex in vinyl silicone (Pt 3.0-3.5%) - Gelest,

C.1.3 Cell Culture Components

, Circular coverslips - Fisher Scientific or other laboratory suppliers, Isopropyl Alcohol (IPA) - Fisher Scientific or other laboratory suppliers, Poly-L-lysine (PLL) - Sigma-Aldrich, Parafilm - Bemis Company, Inc., Phosphate-buffered saline (PBS) - Thermo Fisher Scientific, Glutaraldehyde Solution (0.5%) - Sigma-Aldrich, Gelatin - Sigma-Aldrich, U2OS Cells - ATCC (American Type Culture Collection), McCoy's 5A Medium - ATCC, Fetal Bovine Serum (FBS) - Invitrogen, Penicillin-Streptomycin (PenStrep) - Thermo Fisher Scientific, TrypLE Express Enzyme - Gibco (Thermo Fisher Scientific), Paraformaldehyde Solution (4%) - Electron Microscopy Sciences, Triton X-100 - Sigma-Aldrich, Bovine Serum Albumin (BSA) - Thermo Scientific, 4,6-diamidino-2-phenylindole (DAPI) - Thermo Scientific, Alexa 594-phalloidin - Invitrogen, Fibronectin - Sigma-Aldrich, D-PBS (Dulbecco's Phosphate-Buffered Saline) - Thermo Fisher Scientific, hIPSC-Derived Cardiomyocytes - Celogics, Plating Media - Celogics, Advanced Media - Celogics, Trypan Blue Solution - Thermo Fisher Scientific or Sigma-Aldrich, Cryovials for hIPSC-Derived Cardiomyocytes - Celogics,

C.1.4 Substrates and Slides

Quartz slides (25 mm x 25 mm, 185-2500 nm, 90+% transmission) - Cuvet.co, Soda lime glass slides: 25 mm x 25 mm - Biotain, 25 mm x 75 mm - Corning and Globe Scientific, 50 mm x 75 mm - Fisher Scientific,

C.1.5 Other Materials and Equipment

Transparency Photomasks - Fineline Imaging, 306 stainless steel shim stock - Amazon, Kapton Tape Sheets with Easy-Release Backing - Addicore, Printed Circuit Boards (PCB) - OSH Park, Scotch Magic Tape - Scotch, AA-DUCT 907 Silver Conductive Epoxy - Ted Pella, Fast-Drying Silver Paint, Electrodag 1415M, and Carbon Conductive Paint DAG-T-502 - Ted

Pella, Norland Optical Adhesive 81 (NOA 81) - Norland Products,

C.2 Methods

C.2.1 Standard Soda Lime Glass / Quartz Substrate Cleaning Process

Substrates were cleaned using a Branson 3510 Ultrasonic Cleaner, undergoing 10 minutes of sonication in deionized (DI) water containing the surfactant Alconox. After this initial step, the substrates were rinsed with pure DI water. They were then sonicated sequentially in acetone followed by isopropanol. Clean substrates were stored in isopropanol until use. Just before use, they were treated with air plasma (30 W, 300 mTorr) for 10 minutes in a Harrick Plasma PDC-001.

C.2.2 Photopatterning Agent Preparation

The solutions containing the photoactive combination of $FeCl_3$ and polyethylene oxide are referred to as 'photopatterning agent' solutions. To optimize the technique, the solvent type, $FeCl_3$ concentration, and the concentration of the polyethylene oxide-co-polydimethylsiloxane copolymer (PEO-PDMS) were varied. All photopatterning agent solutions were prepared in glass vials covered with aluminum foil. The preparation process began with adding the specified mass of $FeCl_3$, followed by the required mass of PEO-PDMS. The solvent was then added to achieve the target concentration. The solution was mixed by shaking until homogeneous. The optimized formulation consisted of 4 parts methanol, 0.5 part iron(III) chloride, and 0.5 part PEO-PDMS by mass.

C.2.3 Photopatternable PDMS Preparation

Sylgard 184 Preparation

Mixtures were prepared by combining 10 parts of Sylgard 184 base with 1 part crosslinker in a cup and mixing for 30 seconds. The photopatterning agent was then added to the predetermined concentration and gently mixed to minimize splashing before high-speed mixing. The solution was then mixed for 30 seconds at high speed using a custom emulsion mixing apparatus (Supplementary Figure 1). Afterward, the mixture was degassed in a desiccator under active vacuum until all bubbles were removed, which typically took 30 seconds with our setup. The optimal photopatterning agent for Sylgard 184 consisted of 4 parts methanol, 0.5 part iron(III) chloride, and 0.5 part PEO-PDMS by mass, added at a concentration of 0.1 mL of photopatterning agent per gram of Sylgard 184.

Sylgard 527 Photopatternable PDMS Preparation

Mixtures were prepared by combining 1 part Sylgard 527 Part A with 1 part of Sylgard 527 Part B in a cup and mixing for 30 seconds. The photopatterning agent was then added to a predetermined concentration and gently mixed to minimize splashing before high-speed mixing. The solution was then mixed for 30 seconds at high speed using a custom emulsion mixing apparatus (Supplementary Figure 1). Afterward, the mixture was degassed in a desiccator under active vacuum until all bubbles were removed, which typically took 30 seconds with our setup. The optimal photopatterning agent for Sylgard 184 consisted of 4 parts methanol, 0.5 part iron(III) chloride, and 0.5 part PEO-PDMS by mass, added at a concentration of 0.025 mL of photopatterning agent per gram of Sylgard 184.

Dragon Skin 10 Medium Photopatternable PDMS Preparation

Mixtures were prepared by combining 1 part Dragon Skin 10 Medium Part A with 1 part of Dragon Skin 10 Medium Part B in a cup and mixing for 30 seconds. The photopatterning agent was then added to a predetermined concentration and gently mixed to minimize splashing before high-speed mixing. The solution was then mixed for 30 seconds at high speed using a custom emulsion mixing apparatus (Supplementary Figure 1). Afterward, the mixture was degassed in a desiccator under active vacuum until all bubbles were removed, which typically took 30 seconds with our setup. The optimal photopatterning agent for Sylgard 184 consisted of 4.5 parts tetrahydrofuran, 0.5 part iron(III) chloride, and 0.5 part PEO-PDMS by mass, added at a concentration of 0.1 mL of photopatterning agent per gram of Sylgard 184.

Ecoflex Photopatternable PDMS Preparation

Mixtures were prepared by combining 1 part Ecoflex Part A with 1 part of Ecoflex Part B in a cup and mixing for 30 seconds. The photopatterning agent was then added to a predetermined concentration and gently mixed to minimize splashing before high-speed mixing. The solution was then mixed for 30 seconds at high speed using a custom emulsion mixing apparatus (Supplementary Figure 1). Afterward, the mixture was degassed in a desiccator under active vacuum until all bubbles were removed, which typically took 30 seconds with our setup. The optimal photopatterning agent for Sylgard 184 consisted of 4.5 parts tetrahydrofuran, 0.5 part iron(III) chloride, and 0.5 part PEO-PDMS by mass, added at a concentration of 0.1 mL of photopatterning agent per gram of Sylgard 184.

C.2.4 Photopatternable PDMS Film Preparation

Unless otherwise noted, photopatternable PDMS films were prepared by spin-coating 200 µL of the PDMS mixture onto 25 mm x 25 mm glass slides that had been cleaned following the

standard procedure, using an Ossila Spin Coater. After spin-coating, the samples were promptly transferred to the photopatterning spacer apparatus (Supplementary Figure 10) and then to the UV chamber (Supplementary Figure 11) for photopatterning. To prevent unintended UV exposure, the entire process was conducted in a low-light environment. Following UV exposure, the samples were cured on a hot plate set to 90°C. To ensure uniform heating and protect the film patterns from light exposure and contamination, a small glass-bottom dish covered with aluminum foil was placed over the samples. This setup effectively shielded the films, preserving the integrity of the patterns. Various curing methods were explored, including convection oven and bath curing, but the hot plate provided the most consistent results. After curing, uncured PDMS was removed by submerging the samples in a 120 mL glass vial filled with a solution of 1 part ethyl acetate and 1 part isopropanol. After this initial development, the samples were transferred to a second vial containing the same solution for an additional 30 seconds. The samples were then rinsed with isopropanol and dried using a compressed air gun.

C.2.5 Custom Silicone Formulation

The base of the custom silicones always consisted of 1 ml of Poly(dimethylsiloxane), vinyl terminated (Mw 25,000) with 1 ml of Poly(dimethylsiloxane-co-methylhydrosiloxane), trimethylsilyl terminated (Mn 950, methylhydrosiloxane 50 mol %).

In-situ Catalyst Generation Experiments

To assess if the UV exposure of the photopatterning agent could generate an in-situ catalyst, custom silicone samples were prepared. The photopatterning agent was added at a concentration of 0.1 ml per gram of the base silicone. The samples were then exposed to UV until photobleaching was observed and heated to promote curing. The samples remained liquid under constant UV exposure and heating up to 110O C.

Custom Silicone Cure Time Experiments

Custom silicone samples without the photopatterning agent were prepared by first mixing 5 µL of platinum(0)-1,3-divinyl-1,1,3,3-tetramethyldisiloxane complex in xylene (Pt 2%) with 1 mL of poly(dimethylsiloxane), vinyl-terminated (Mw 25,000). This mixture was then combined with 1 mL of poly(dimethylsiloxane-co-methylhydrosiloxane), trimethylsilyl-terminated (Mn 950, methylhydrosiloxane 50 mol %). The solidification time was measured using a stopwatch and a wooden mixing stick. Custom silicone samples with the photopatterning agent were prepared similarly. First, 5 µL of platinum(0)-1,3-divinyl-1,1,3,3-tetramethyldisiloxane complex in xylene (Pt 2%) was mixed with 1 mL of poly(dimethylsiloxane), vinyl-terminated (Mw 25,000). Separately, 0.1 mL of the photopatterning agent was combined with 1 mL of poly(dimethylsiloxane-co-methylhydrosiloxane), trimethylsilyl-terminated (Mn 950, methylhydrosiloxane 50 mol %) using a magnetic stir bar on a hotplate set to maximum speed for 10 minutes. The platinum-vinyl mixture and the photopatterning agent-hydrosilane mixture were then combined, and the solidification time was measured with a stopwatch and a wooden mixing stick. To evaluate the effect of the photopatterning agent on film curing, a separate batch of silicone was prepared in the same manner. Films were spin-coated onto pre-cleaned 25 mm x 25 mm slides at 1,000 rpm for 30 seconds. The samples were either exposed to UV light or left unexposed. Samples that were exposed received a dose of 696 mJ. Samples were then placed on a hotplate at 90O C, and the smear-free cure time was measured.

C.2.6 Photopatterning Agent Optimization

Smear Free Cure Time Method

To evaluate the curing time of PDMS samples, a stopwatch was used to record the duration, while a cotton swab was employed to check for surface residue at regular intervals. During the initial stages of curing, the sample remained in a liquid state, transferring a noticeable

residue—often orange or yellowish—onto the cotton swab and causing reduced optical transparency on the PDMS film. As the curing advanced, the sample became tacky, leaving lighter smears on both the swab and the film. Full curing was confirmed when the PDMS developed a firm, solid surface that was entirely smear-free, with no residue transferred to the swab. The curing time was defined as the point at which this smear-free state was first observed.

FeCl3 Concentration Trend Measurement

In the FeCl3 Concentration experiment, multiple Sylgard 184 Photopatternable PDMS mixtures were prepared with different iron(III) chloride concentrations. This involved preparing multiple photopatterning agents, each consisting of 5 parts MeOH mixed with one of the following iron(III) chloride concentrations: 0.1, 0.2, 0.5, 0.75, and 1. Photopatternable PDMS films were then prepared on 25 mm x 25 mm glass slides, following the procedure outlined in the Photopatternable PDMS Film sections. All samples were cured on the hot plate at 90°C.

Photopatterning Agent Solvent Optimization

In the Photopattering Agent Solvent Experiment, multiple Sylgard 184 Photopatternable PDMS mixtures were prepared with different solvents being used to create the photopatterning agent. These solvents were MeOH, EtOH, PGMEA, THF, and H2O. Each photopatterning agent consisted of 4 parts of the particular solvent, 0.5 parts iron(III) chloride, and 0.5 parts PEO-PDMS BCP. Photopatternable PDMS films were then prepared on 25 mm x 25 mm glass slides, following the procedure outlined in the Photopatternable PDMS Film sections. For each solvent, four exposed and unexposed samples were prepared. Samples that were exposed received a dose of 696 mJ. All samples were cured on the hot plate at 90°C. The difference in cure time between the exposed and unexposed samples (contrast) was measured using the smear free cure time method.

PEO-PDMS BCP Concentration Contrast Experiment

In the PEO-PDMS BCP Concentration experiment, multiple Sylgard 184 Photopatternable PDMS mixtures were prepared with different PEO-PDMS BCP concentrations. This involved preparing multiple photopatterning agents, each consisting of 5 parts MeOH and 0.5 part iron(III) chloride mixed with one of the following PEO-PDMS BCP concentrations: 0, 0.05, 0.1, 0.2, 0.3 0.4, 0.5, 0.6, 1.0. Photopatternable PDMS films were then prepared on 25 mm x 25 mm glass slides, following the procedure outlined in the Photopatternable PDMS Film sections. For each PEO-PDMS BCP concentration, four exposed and unexposed samples were prepared. Samples that were exposed received a dose of 696 mJ. All samples were cured on the hot plate at 90°C. The difference in cure time between the exposed and unexposed samples (contrast) was measured using the smear free cure time method.

Photopatterning Agent Concentration Contrast Experiment

In the Photopatterning Agent Concentration Experiment, multiple Sylgard 184 Photopatternable PDMS mixtures were prepared with different volumes of photopatterning agent added. This involved preparing a photopatterning agent consisting of 5 parts MeOH, 0.5 part iron(III) chloride, and 0.5 PEO-PDMS BCP. The volumes in mL of photopatterning agent added to 5 parts Sylgard 184 base and 1 part curing agent were: 0, 0.1, 0.2, 0.5, 0.8. For each photopatterning agent concentration, four exposed and unexposed samples were prepared. Samples that were exposed received a dose of 696 mJ. All samples were cured on the hot plate at 90°C. The difference in cure time between the exposed and unexposed samples (contrast) was measured using the smear free cure time method.

C.2.7 Silver Nanowires Synthesis

Silver nanowires were synthesized by first preparing fresh silver chloride (AgCl) powder. Aqueous silver nitrate (0.5 M) and aqueous sodium chloride (1.0 M) were combined until the AgCl precipitate formed. Once the precipitate was fully formed, the supernatant was decanted. The product was washed with DI water and decanted three times. The AgCl product was then dried in a freezer for 2 hours and then in lyophilizer for 24 hours. A 0.34 g polyvinylpyrrolidone (PVP, 55K) ethylene glycol solution was prepared and allowed to equilibrate in a 160°C oil bath stirred at 700 rpm. Once the PVP was dissolved and equilibrium was reached, 0.025 g of AgCl was added to the flask. After 3 minutes, 0.15 g of solid $AgNO_3$ was added to the flask. The flask was then capped, and the reaction progressed until visible nanowire formation. After the reaction was complete, the flask was removed from heat and cooled to room temperature until easily handled. The product was washed with acetone and centrifuged at 2000 rpm for 20 minutes, decanted, and then washed with ethanol at least three times. The final product was dispersed in ethanol and stored under argon to prevent oxidation.

C.2.8 Gold Coated Silver Nanowires Synthesis

Gold-coated silver nanowires were synthesized by first preparing the gold-sulfite complex growth solution. 0.84 mL of 0.25 M HAuCl4·3H2O was mixed with 5.54 mL of 0.2 M sodium hydroxide in a beaker. Subsequently, 63 mL of 0.01 M sodium sulfite was added to the mixture, followed by 99 mL of Milli-Q water. The mixture was left undisturbed for 12 hours. For the preparation of the Ag nanowire solution, 190 mL of Milli-Q water was mixed with 12 mL of Ag nanowires in Milli-Q water (5 mg/mL). 42 mL of 5 wt% PVP was added, followed by 8.4 mL of 0.5 M sodium hydroxide, 8.4 mL of 0.5 M L-AA, and 2.1 mL of 0.1 M sodium sulfite. The solution was then thoroughly stirred for 10 minutes at 500 rpm. The gold-sulfite complex growth solution was slowly added to the Ag nanowire solution using a syringe pump at a rate

of 4 mL/min. The mixture was then left undisturbed for 2 hours at room temperature. The final solution was washed once with acetone and three times with ethanol, centrifuging at 2000 rpm for 20 minutes for each wash.

C.2.9 Shadow Mask Preparation

Shadow masks were created by laser cutting 0.1 mm shim stock using the FabLight Fiber Laser Cutter. After laser cutting, the masks underwent a 10-minute sonication using the Branson 3510 Ultrasonic Cleaner in isopropanol.

C.3 Characterization Techniques

C.3.1 UV/Vis Spectroscopy Characterization

The Cary 60 UV-Vis spectrophotometer from Agilent was utilized for the qualitative assessment of Fe3+ complexes within the oxidant films. All samples were prepared on quartz slides, following the standard substrate cleaning procedure detailed above. A clean bare 25 mm x 25 mm quartz slide was employed to collect baseline data. The UV-Vis range settings were configured to cover 200 nm - 800 nm, and the scan controls were set to survey. A Sylgard 184 Photopatternable PDMS film was prepared on quartz slides following the procedure outlined in the Photopatternable PDMS Film sections. The first sample prepared remained unexposed and was then measured in the UV-Vis. The second sample followed the same preparation procedure but was exposed in the UV exposure chamber for 30 seconds. Then, the adsorption of the sample was measured in the UV-Vis. This process was repeated once more, with the subsequent sample being exposed for an additional 30 seconds.

C.3.2 UV/Vis Optical Transparency

Samples of photopatternable Sylgard 184, Sylgard 527, Dragon Skin 10 Medium, and Ecoflex 00-30 were prepared according to the procedures described in supplementary section 2.3. The films were prepared on 25 mm x 25 mm quartz slides cleaned according to the standard cleaning procedure. The Cary 60 UV-Vis spectrophotometer from Agilent was utilized to characterize the optical properties of the unmodified silicone elastomers and the photopatternable silicone elastomers before and after soaking the samples in 2-propanol.

C.3.3 Nanoindentation Testing

Samples of photopatternable Sylgard 184, Sylgard 527, Dragon Skin 10 Medium, and Ecoflex 00-30 were prepared according to the procedures described in supplementary section 2.3. The films were prepared on 25 mm x 25 mm quartz slides cleaned according to the standard cleaning procedure. The local Young's modulus of samples were measured using a nanoindenter (Piuma, Optics 11 Life, Netherlands) using a spherical tipped probe with a stiffness of 4.58 N•m-1, tip radius of 58 μm, and indentation depth of 1 μm. Each sample was tested using a 4x4 matrix scan covering an area of 2000 μm2 in two locations.

C.3.4 Water-assisted Tensile Testing

Tensile testing was performed exclusively on Sylgard 184, Ecoflex, and Dragon Skin 10 Medium. Attempts to obtain data for Sylgard 527 were unsuccessful due to the film's tendency to curl onto itself, creating significant handling difficulties. Additionally, the films adhered to various surfaces, further limiting the accuracy and feasibility of the tensile tests. The tensile testing procedure began with a standard cleaning process for 50 mm x 75 mm glass slides. Subsequently, a 7.5% dextran solution in deionized water was prepared by dissolving 0.75 g of dextran in 10 g of water. This solution was spin-coated onto the cleaned glass slides at 1000 rpm for 40 seconds,

followed by baking at 90°C for 3 minutes to solidify the dextran layer. For each of the three silicone types, both modified and unmodified mixtures were prepared, maintaining identical conditions between the two sample sets. Sylgard 184 and Ecoflex mixtures were spin-coated onto the glass slides at 2000 rpm for 40 seconds, followed by an edge bead removal at 6000 rpm for 10 seconds. Dragon Skin 10 Medium mixtures were spin-coated at 6000 rpm for 60 seconds. For the modified samples, an additional UV exposure step was introduced, with the samples exposed to UV light for 1 minute. Finally, all samples were cured in a convection oven at 100°C for 10 minutes. Testing was conducted using a Mark-10 system equipped with a 0.5N force gauge. The films were carefully transferred onto the water surface, where it floats due to surface tension. Custom 3D-printed grippers were employed to pull the floating films apart during the test. By applying a controlled tension, the mechanical properties of the film can be measured. Small squares of Sylgard 184, prepared with a ratio of 20 parts base to 1 part curing agent, were attached to the films using double-sided tape. These squares were used as the contact material to interface directly with the films.

C.3.5 Film Profilometry Measurement

The thickness of the Photopatternable PDMS films were determined using a Profilm3D Profilometer based on white light interferometry. The Profilm Desktop Analysis software was employed to average the trench depth and calculate the film thickness.

C.3.6 FTIR Characterization

A Nicolet™ iS50 Fourier Transform Infrared (FTIR) spectrometer, equipped with a Smart-iTR diamond Attenuated Total Reflectance (ATR) attachment, was used to assess changes in the chemical characteristics of the custom silicone formulations under UV irradiation. 5 L droplets of the custom silicone formulation containing the photopatterning agent (see Supplementary Section

2.5.2 for formulation details) were placed on the ATR diamond observation plate. Spectra were recorded for the unexposed droplet, as well as after 30 seconds and 60 seconds of exposure to the UV LED.

C.3.7 Biocompatibility Measurements

Substrate Preparation

Biocompatibility assessment samples were prepared by spin coating Sylgard 184 (see supplementary section 2.3.1 for details) onto precleaned circular coverslips. To coat the surface for cell adhesion, coverslips were sterilized by rinsing with deionized water and then allowed to soak in pure isopropyl alcohol (IPA) for 30 minutes. After soaking the surfaces were rinsed one additional time with IPA and allowed to dry at room temperature inside a chemical fume hood. Dry substrates were UVO-treated for 10 min and incubated with 100 µg mL1 poly-L-lysine (PLL) solution. PLL was applied by inverting the substrate onto a 100 µL droplet on parafilm, with the polydimethylsiloxane (PDMS) coated surface side contacting the droplet, and incubated at room temperature for 30 min. The substrate was then washed 3 times with PBS. 0.5% glutaraldehyde solution was added for 30 min to crosslink the proteins and washed with PBS. Finally, a pre-warmed 0.1% gelatin solution was applied, and the substrate was incubated for another 30 min at 37 degrees Celsius.

Cell Culture and Seeding

U2OS cells were obtained from ATCC; U2OS cells were cultured in McCoy's 5A medium (ACC) supplemented with 10% fetal bovine serum (FBS, Invitrogen) and 1% penicillin-streptomycin (PenStrep, ThermoFisher Scientific) and cultured under humidified conditions at 37 °C and 5% CO2. To seed cells onto the PDMS coated coverslips, first have detached cells using TrypLE Express Enzyme (Gibco) and prepare a 100 µL suspension containing 40,000 cells.

The coverslips were placed in a 12-well plate and rinsed 3 times with PBS. The droplets of cells mixed thoroughly to ensure uniform distribution of cells. After 10 min of initial adhesion, 1 mL of growth media was added and the cells incubated at 37 °C and allowed to grow for 48 hours.

Fluorescent Staining and Microscopy

Cells were fixed using 4% paraformaldehyde (Electron Microscopy Sciences, USA), for a duration of 40 minutes at room temperature and washed with PBS to remove excess fixative. Cells were permeabilized with a 1% solution of Triton X-100 (Sigma-Aldrich, USA) for 10 min and blocked using a 2% w/v solution of Bovine Serum Albumin (BSA) (Thermo Scientific, USA) for one hour. Samples were washed in PBS and stained with 4,6-diamidino-2-phenylindole (DAPI) (Thermo Scientific, USA) for 10 minutes and Alexa 594-phalloidin (Invitrogen, USA) for 20 min in the dark to stain the nucleus and F-actin. Images were collected with an Echo Revolution microscope with the following objectives. 20x PLAN Fluorite LWD CC Phase Ph1 NA 0.45, 40x PLAN Fluorite LWD CC Phase Ph2 NA 0.60.

C.4 Device Fabrication Protocols.

C.4.1 Microfluidic Device Fabrication

The fabrication of the microfluidic device begins with the standard cleaning procedure for 25 mm x 75 mm glass slides. Once cleaned, 1 mL of Sylgard 184 Photopatternable PDMS mixture is spin-coated onto the slides at 1500 rpm for 40 seconds. After spin coating, the Photopatternable PDMS layer is patterned using UV exposure for 30 seconds. The patterned films are then cured on a hot plate for 2 minutes. Following the curing process, the films were then developed to reveal the patterned features. Next, a separate PDMS lid is prepared by mixing 10 parts Sylgard 184 base with 1 part curing agent. This mixture is vacuumed to remove all air bubbles. To prevent the microfluidic devices from bursting upon introducing the liquid, drops of NOA 81 are applied

to the regions on the mold where the fluids were stored. This also aided with the placement of the needles. A PDMS glue is also prepared by mixing 1 part Sylgard 184 base with 1 part curing agent. For device assembly, a 50 mm x 75 mm glass slide is spin-coated with this PDMS glue mixture. The glue is then carefully transferred to the PDMS lid by stamping, ensuring an even coating. The lid is placed onto the patterned silicone layer, with care, avoiding the blocking of the channels. Once the device is fully assembled, needles are inserted through the PDMS lid to create the necessary ports, completing the microfluidic device.

C.4.2 Cardiac Microphysiological Devices with Integrated Sensors

Device Fabrication

The fabrication process began with the standard cleaning of 25 mm x 25 mm glass slides.. Alignment marks were created by preparing a diluted silver paint and spray-coating it onto the slides using a shadow mask. Following the creation of the alignment marks, the samples were exposed to air plasma treatment at 30 W and 300 mTorr in a Harrick Plasma PDC-001 for 3 minutes. This treatment enhanced the adhesion of subsequent layers. After plasma treatment, the samples were rinsed with isopropanol and dried with the compressed air gun to remove any residual contaminants. The first layer of Photopatternable PDMS was applied by spin-coating at 2000 rpm for 20 seconds, followed by an edge bead removal step of 6000 rpm for 10 seconds. These were exposed for 20 seconds using the 1.2 mm spacer and cured on the hot plate at 90°C for minutes. After curing, the films were developed in ethyl acetate, rinsed with isopropanol, and dried with the compressed air gun. Next, a 7.5% dextran solution in DI water was prepared by dissolving 0.75 g of dextran in 10 g of water. 2 µL of the dextran solution was drop-cast into designated holes within the first Photopatternable PDMS layer and cured on the hot plate at 90°C for 3 minutes. This layer acts as a water-soluble release layer for the cantilever once the device is complete. This was followed by the application of a second, thinner layer of Photopatternable

PDMS, spin-coated at 6000 rpm for 2 minutes. These were exposed for 20 seconds using the 1.2 mm spacer and cured on the hot plate at 75°C for 2 minutes. The lower curing temperature reduced the stress in the films. After curing, the films were developed in the standard developer solution, rinsed with isopropanol, and dried with the compressed air gun. Following the creation of the second , the samples were exposed to air plasma treatment at 30 W and 300 mTorr in a Harrick Plasma PDC-001 for 10 minutes. This treatment ensured the even dispersal of the Au-AgNWs. To create the sensors, Au-AgNWs was patterned onto the sample using a spray-coating technique and a shadow mask. Silver epoxy contacts were then screen-printed onto the device using another shadow mask to define the contact points. The third layer of Photopatternable PDMS was applied by spin-coating at 2000 rpm for 40 seconds, followed by an edge bead removal step of 6000 rpm for 10 seconds. These were exposed for 20 seconds using the 1.2 mm spacer and cured on the hot plate at 75°C for 6 minutes. After curing, the films were developed in ethyl acetate, rinsed with isopropanol, and dried with the compressed air gun. To ensure biocompatibility, SU-8 was applied to coat both the PCB holes and the custom 3D-printed culture rings, providing a protective layer that prevents interaction between the raw fiberglass material of the PCB as well as the 3D printed resin with the cultured cells. The device was then glued to the PCB using NOA 81, carefully aligning the silver epoxy contacts with the corresponding contacts on the PCB. Finally, NOA 81 was used to glue the culture ring to the opposite side of the PCB, completing the fabrication of the cardiac microphysiological device with integrated sensors.

Cardiomyocyte Culture Procedure

Substrate Preparation and Fibronectin Coating: Silicone cantilevers prepared for cardiomyocyte culture were first functionalized with air plasma (30 W, 300 mTorr) for 5 minutes using a Harrick Plasma PDC-001 to enable fibronectin functionalization. The cantilevers devices were then sanitized and cleaned by fully submerging them in a large vial of 100% 2-propanol. Subsequent cell culture steps were conducted in a biosafety cabinet. A fibronectin coating solution

was prepared at a working concentration of 50 µg/mL by diluting fibronectin in D-PBS, and 20 µL of this solution was carefully pipetted onto each cantilever to coat the designated cell-seeding area. To prevent drying during incubation, 6-8 mL of D-PBS was added around the cantilevers, and the coated cantilevers were incubated at 37°C for 1 hour. Cell Thawing and Preparation: Cell plating media was equilibrated at room temperature (25°C) for at least 30 minutes before use. A vial of hIPSC-derived cardiomyocytes was retrieved from liquid nitrogen storage, thawed in a 37°C bath until approximately 80% thawed (around 3 minutes), and then sprayed with 70% ethanol and transferred to the biosafety cabinet. The vial contents were transferred dropwise into 8 mL of pre-warmed plating media with gentle swirling to minimize osmotic shock. The empty cryovial was rinsed with an additional 1 mL of plating media, also added dropwise to the cell suspension. Cells were then centrifuged at 180 x g for 3 minutes at room temperature, the supernatant was discarded, and the cell pellet was gently resuspended in 1 mL of plating media for counting. Cell viability was assessed using Trypan blue, and viable cell counts were used to calculate the required seeding volume. Cell Seeding on Cantilevers: Based on the calculated cell concentration, a suspension of 50,000 cells in 5 µL of plating media was prepared for each cantilever. The fibronectin solution was removed from each cantilever before 5 µL of the prepared cell suspension was carefully added, ensuring the droplet remained within the coated area. To maintain humidity and prevent drying during the 1-hour room temperature incubation, 3 mL of D-PBS was added around each cantilever. Initial Media Replacement: Following the 1-hour incubation, 300 µL of pre-warmed plating media was added to each cantilever. Twenty-four hours post-seeding, the media was replaced with pre-warmed advanced media by gently aspirating the old media and adding 300 µL of fresh advanced media along the well wall to avoid disturbing the cell layer. Ongoing Media Maintenance: After the initial media change, fresh advanced media was added to the cantilevers every 48 hours to support ongoing cell culture.

Data acquisition and Analysis

Two days after culture, resistance versus time data from a moving cantilever was collected using a Keithley DAQ 6510 digital data acquisition system. The device was removed from the incubator and connected to the data acquisition system via a ribbon cable linked to a custom switchboard. Resistance versus time data was then acquired and processed in MATLAB. An exponential decay term was removed from the data (Supplementary Figure 13), and the remaining signal was subsequently bandpass filtered with cutoff frequencies of 0.1 Hz and 2 Hz (Figure 6e).

Appendix D

Additional Figures and Data for A Simple Method for Photopatterning Commercial PDMS Using an Off-the-Shelf Photodeactivated Hydrosilylation Inhibitor

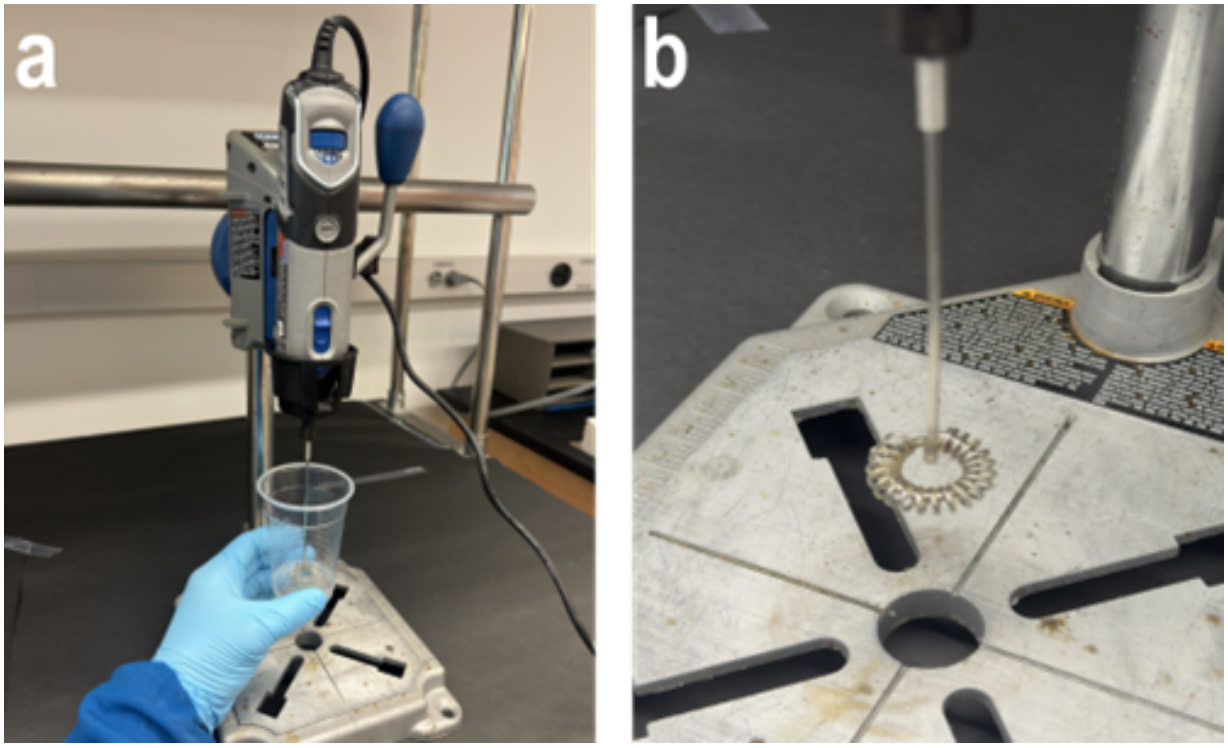

Figure D.1: A Bodum Schiuma Milk Frother, acquired from Target, was modified by detaching the whisk and attaching it to a Dremel 4000 tool, which was subsequently mounted on a Dremel drill press workstation. This custom setup allows for highly efficient mixing of solutions, utilizing the Dremel's power and precision to achieve consistent emulsions. Operating at a speed of 10,000 rpm, this system has proven far superior to traditional hot plate mixing. Traditional hot plate mixing methods were insufficient for thicker viscosity mixtures, such as Dragon Skin 10 Medium, often failing to achieve a proper mix. In contrast, this enhanced system not only handles these challenging materials but also delivers more consistent and reliable results, making it an ideal choice for applications requiring precise and controlled mixing. All Photopatternable PDMS mixtures were mixed using this setup. a) The mixing setup used for Photopatternable PDMS mixtures, featuring the modified Dremel tool mounted on a drill press workstation. b) Close-up view of the whisk attachment, originally taken from a milk frother.

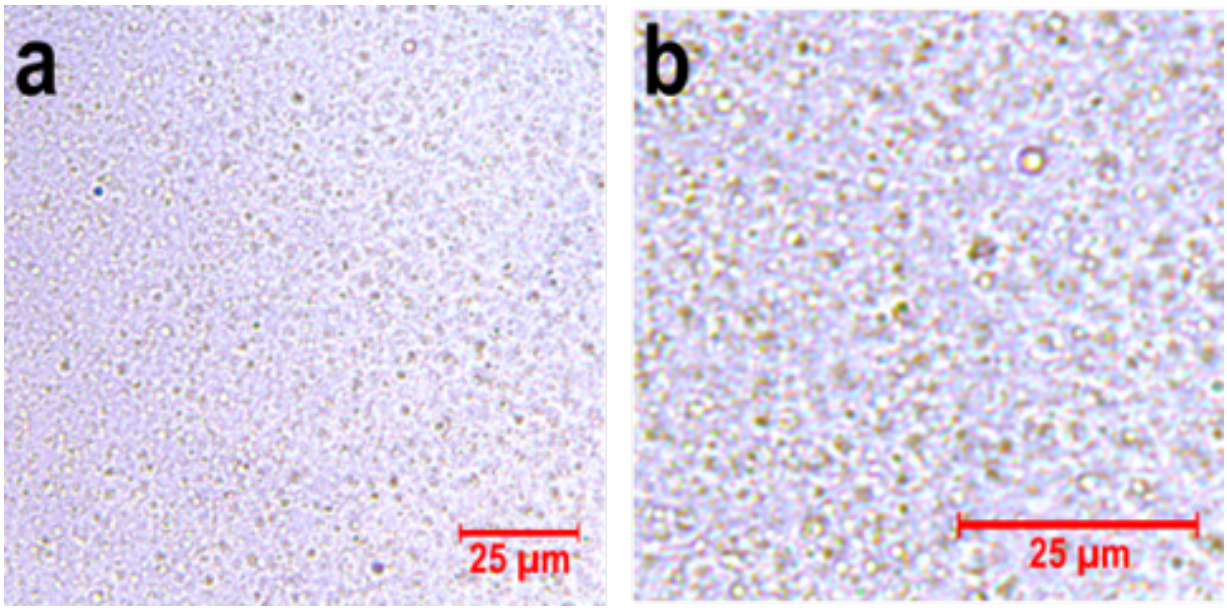

Figure D.2: Images of Sylgard 184 Photopatternable PDMS mixtures taken at a) 50x and b) 100x magnification. The droplets were too small to quantify in their size or uniformity.

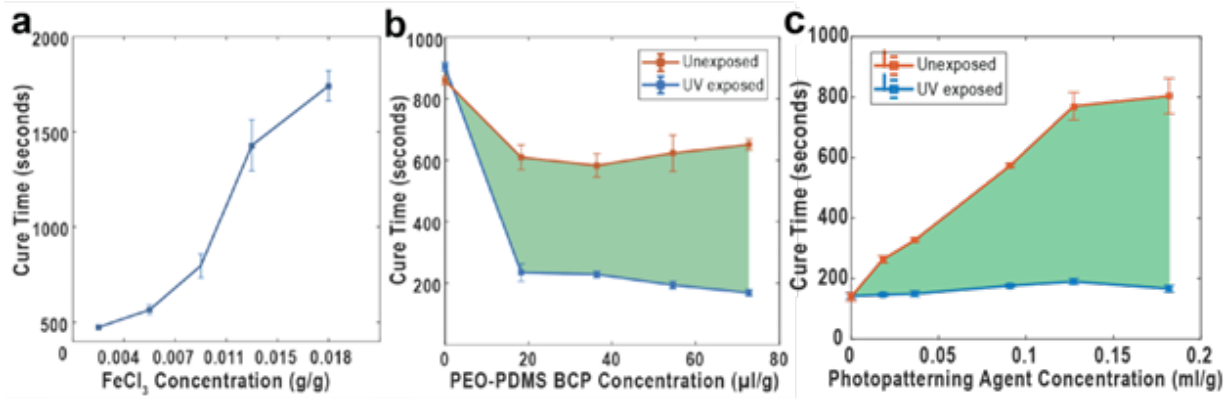

Figure D.3: Characteristics of the Photopatterning Process Using Sylgard 184. All ratios are measured relative to the mass of silicone liquid used in the elastomer preparation. Tetrahydrofuran (THF) was used as the solvent for this batch of samples; however, THF resulted in lower contrast compared to other solvents including methanol. (a) Increasing the amounts of THF and $FeCl_3$ in the silicone extended the curing time. (b) A difference in cure time between exposed and unexposed samples was observed only when a fixed amount of $FeCl_3$ was used along with a variable amount of polyethylene oxide (PEO)-polydimethylsiloxane (PDMS) copolymer (BCP). (c) Contrast improved with increasing concentrations of the photopatterning agent. However, at concentrations above 0.15 ml/g, the silicone mixture thickened, hindering uniform mixing of additional photopatterning agent.

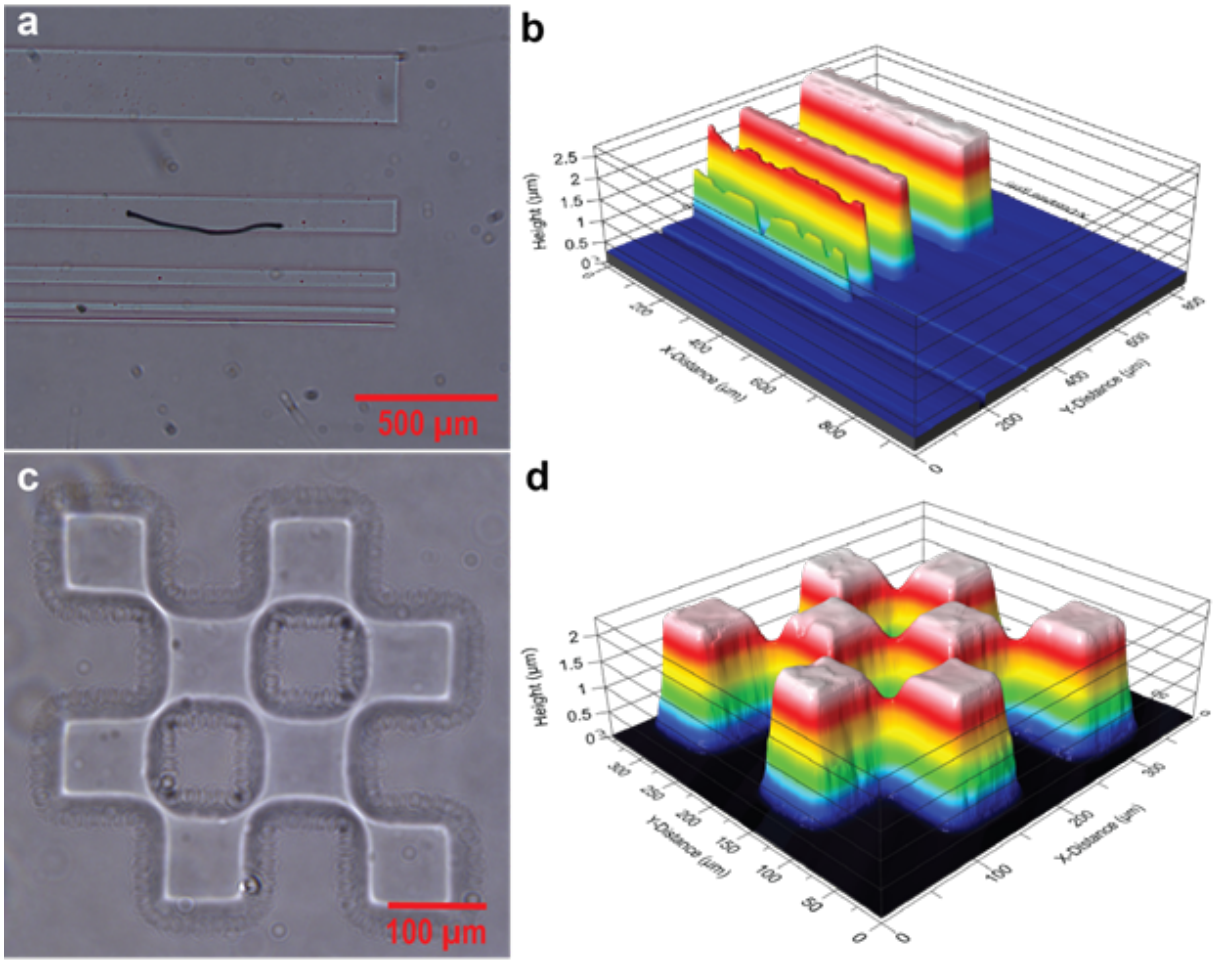

Figure D.4: Patterned Sylgard 184. Conditions: Standard photopatterning agent (4:0.5:0.5), spin-coated at 6000 rpm for 180 seconds, 10-second exposure (11.7 mW/cm^2), 60-second post-exposure bake, 30-second development in 50% ethyl acetate and 50% 2-propanol, followed by a 2-propanol rinse. (a) Optical microscope image of patterned lines. (b) 3D profile of the lines obtained using white light interferometry. (c) Optical microscope image of a checkerboard pattern. (d) 3D profile of the checkerboard pattern obtained using white light interferometry.

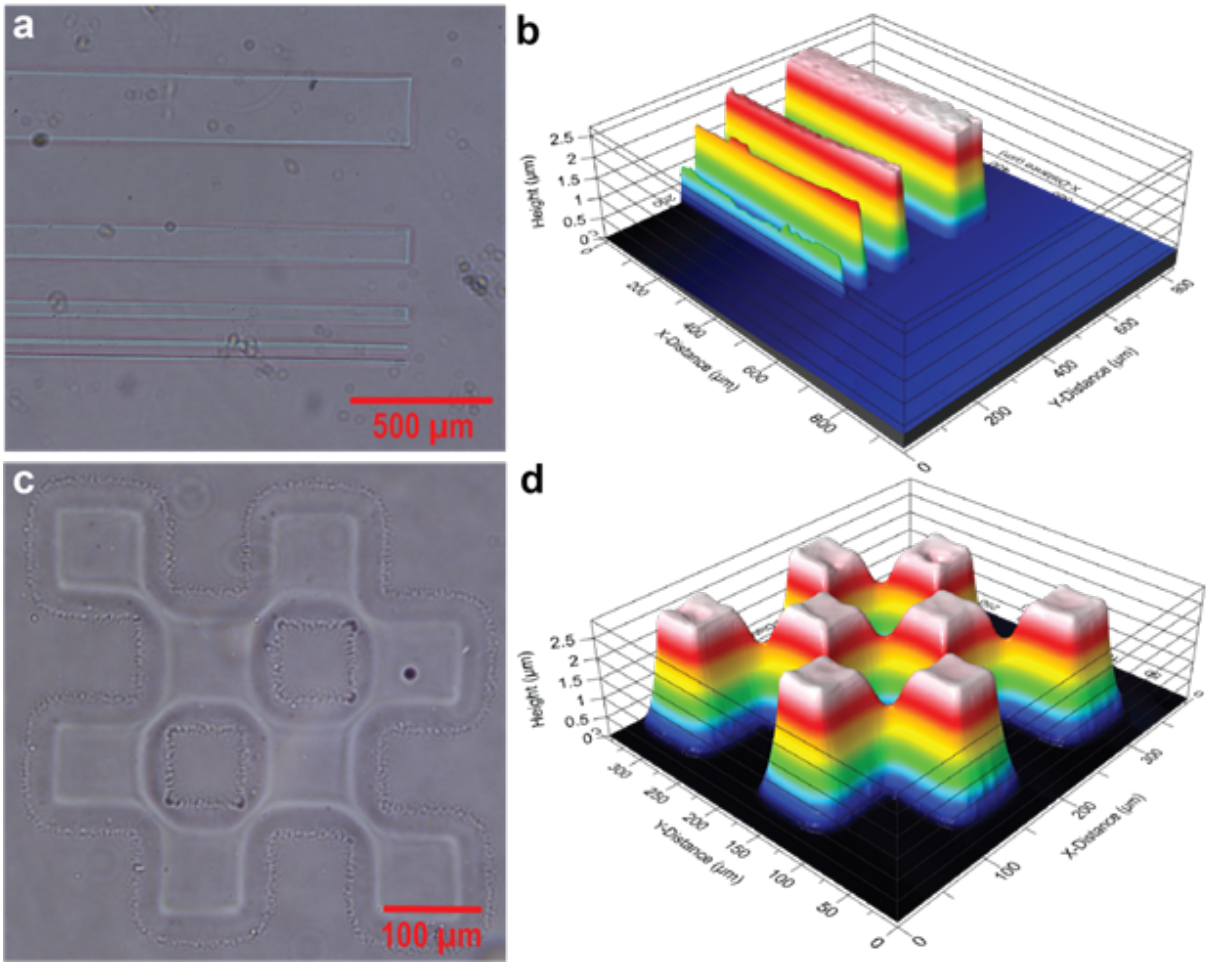

Figure D.5: Patterned Sylgard 184. Conditions: Standard photopatterning agent (4:0.5:0.5), spin-coated at 6000 rpm for 120 seconds, 10-second exposure (11.7 mW/cm^2), 70-second post-exposure bake, 30-second development in 50% ethyl acetate and 50% 2-propanol, followed by a 2-propanol rinse. (a) Optical microscope image of patterned lines. (b) 3D profile of the lines obtained using white light interferometry. (c) Optical microscope image of a checkerboard pattern. (d) 3D profile of the checkerboard pattern obtained using white light interferometry.

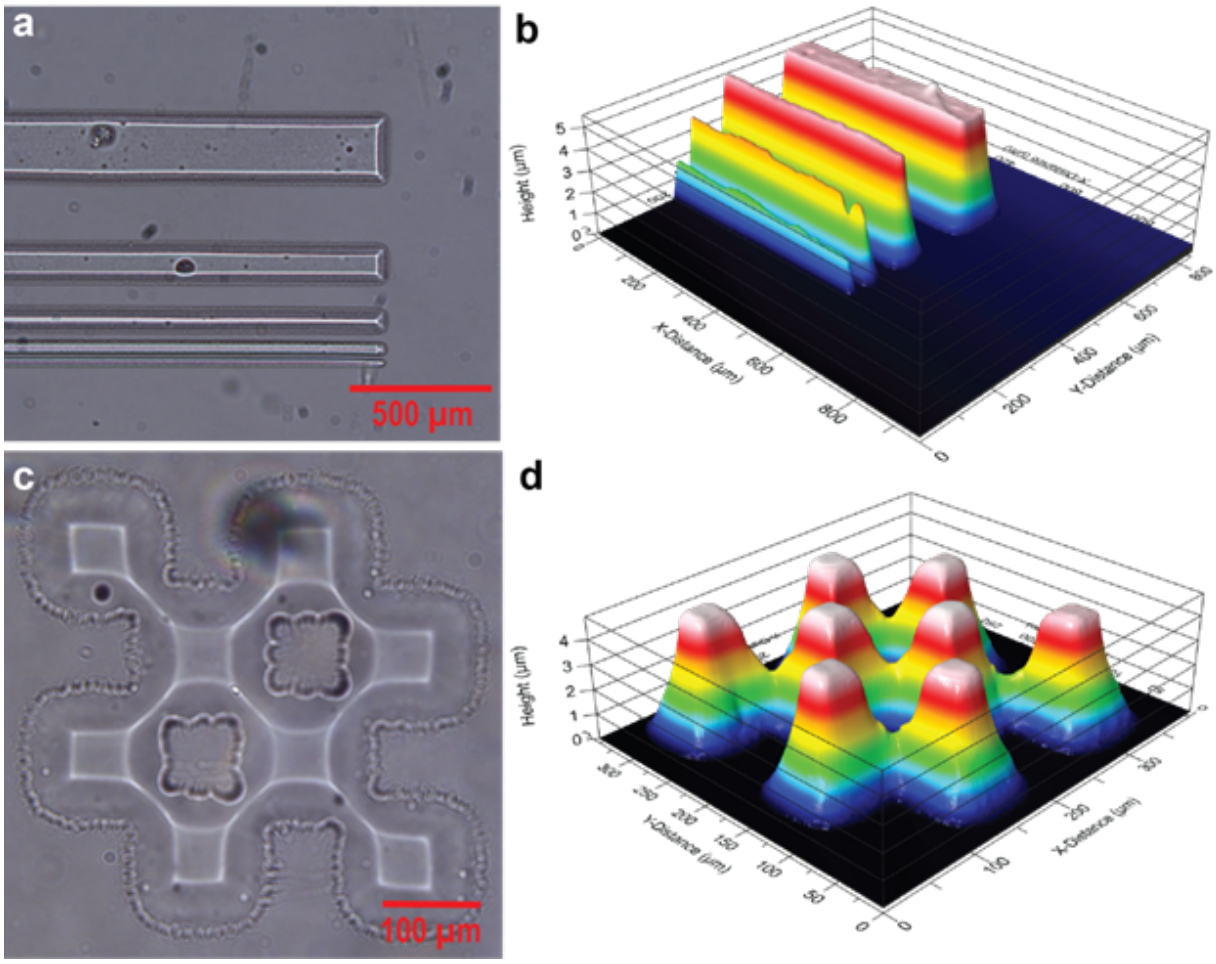

Figure D.6: Patterned Sylgard 184. Conditions: Standard photopatterning agent (4:0.5:0.5), spin-coated at 6000 rpm for 60 seconds, 10-second exposure (11.7 mW/cm^2), 90-second post-exposure bake, 30-second development in 50% ethyl acetate and 50% 2-propanol, followed by a 2-propanol rinse. (a) Optical microscope image of patterned lines. (b) 3D profile of the lines obtained using white light interferometry. (c) Optical microscope image of a checkerboard pattern. (d) 3D profile of the checkerboard pattern obtained using white light interferometry.

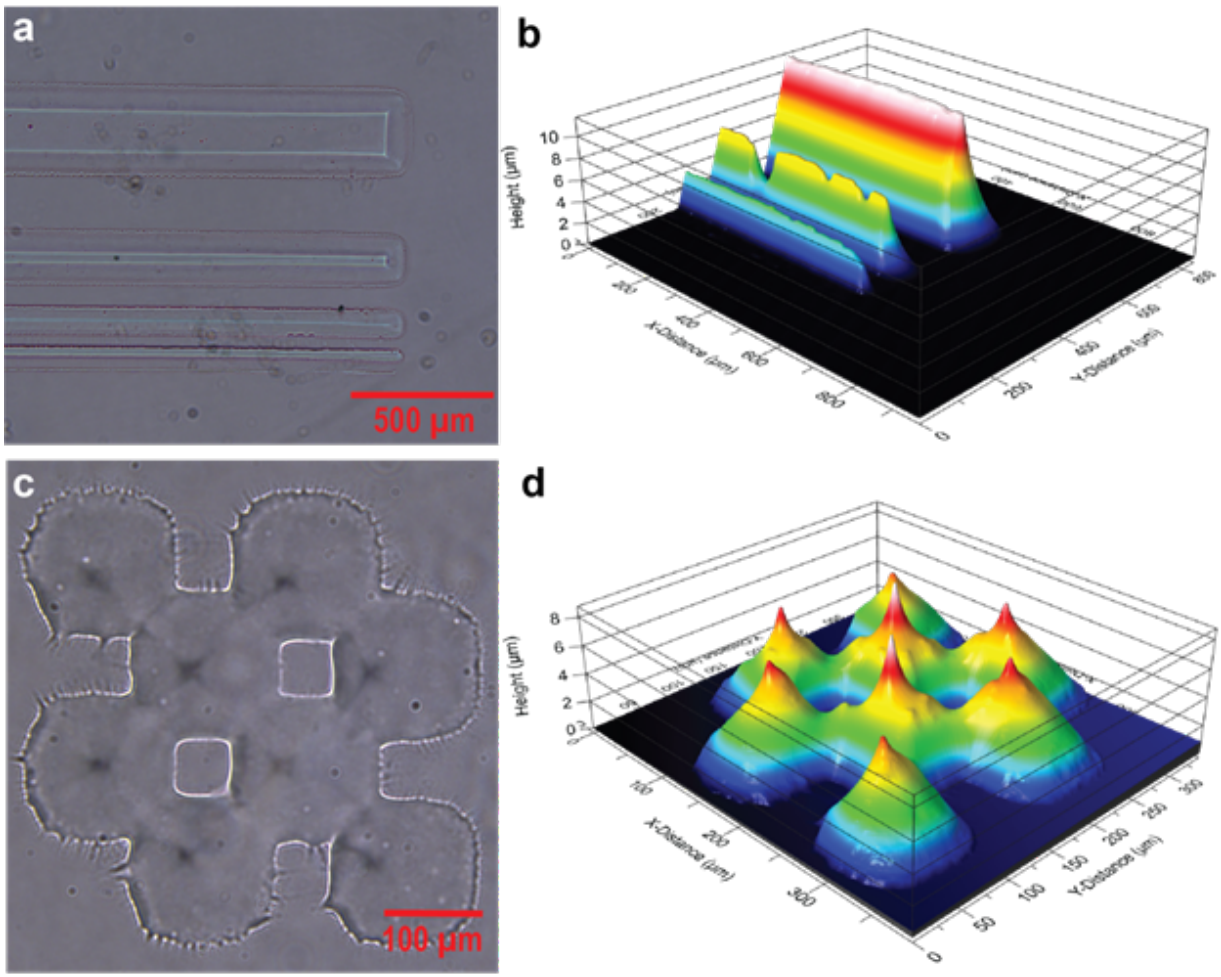

Figure D.7: Patterned Sylgard 184. Conditions: Standard photopatterning agent (4:0.5:0.5), spin-coated at 6000 rpm for 30 seconds, 10-second exposure (11.7 mW/cm²), 100-second post-exposure bake, 30-second development in 50% ethyl acetate and 50% 2-propanol, followed by a 2-propanol rinse. (a) Optical microscope image of patterned lines. (b) 3D profile of the lines obtained using white light interferometry. (c) Optical microscope image of a checkerboard pattern. (d) 3D profile of the checkerboard pattern obtained using white light interferometry.

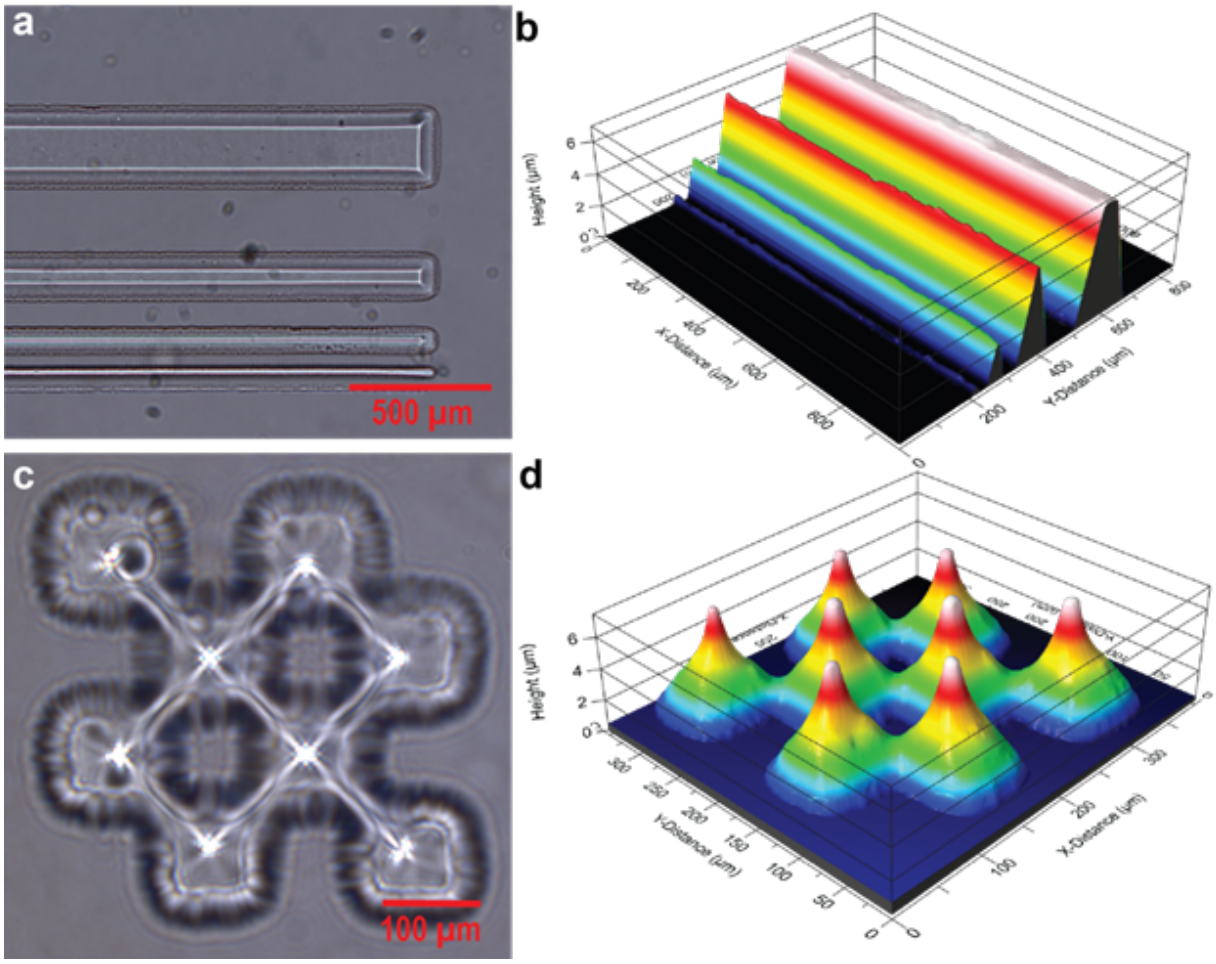

Figure D.8: Patterned Sylgard 184. Conditions: Standard photopatterning agent (4:0.5:0.5), spin-coated at 2000 rpm for 40 seconds, 6000 rpm for 10 seconds, 10-second exposure (11.7 mW/cm^2), 120-second post-exposure bake, 30-second development in 50% ethyl acetate and 50% 2-propanol, followed by a 2-propanol rinse. (a) Optical microscope image of patterned lines. (b) 3D profile of the lines obtained using white light interferometry. (c) Optical microscope image of a checkerboard pattern. (d) 3D profile of the checkerboard pattern obtained using white light interferometry.

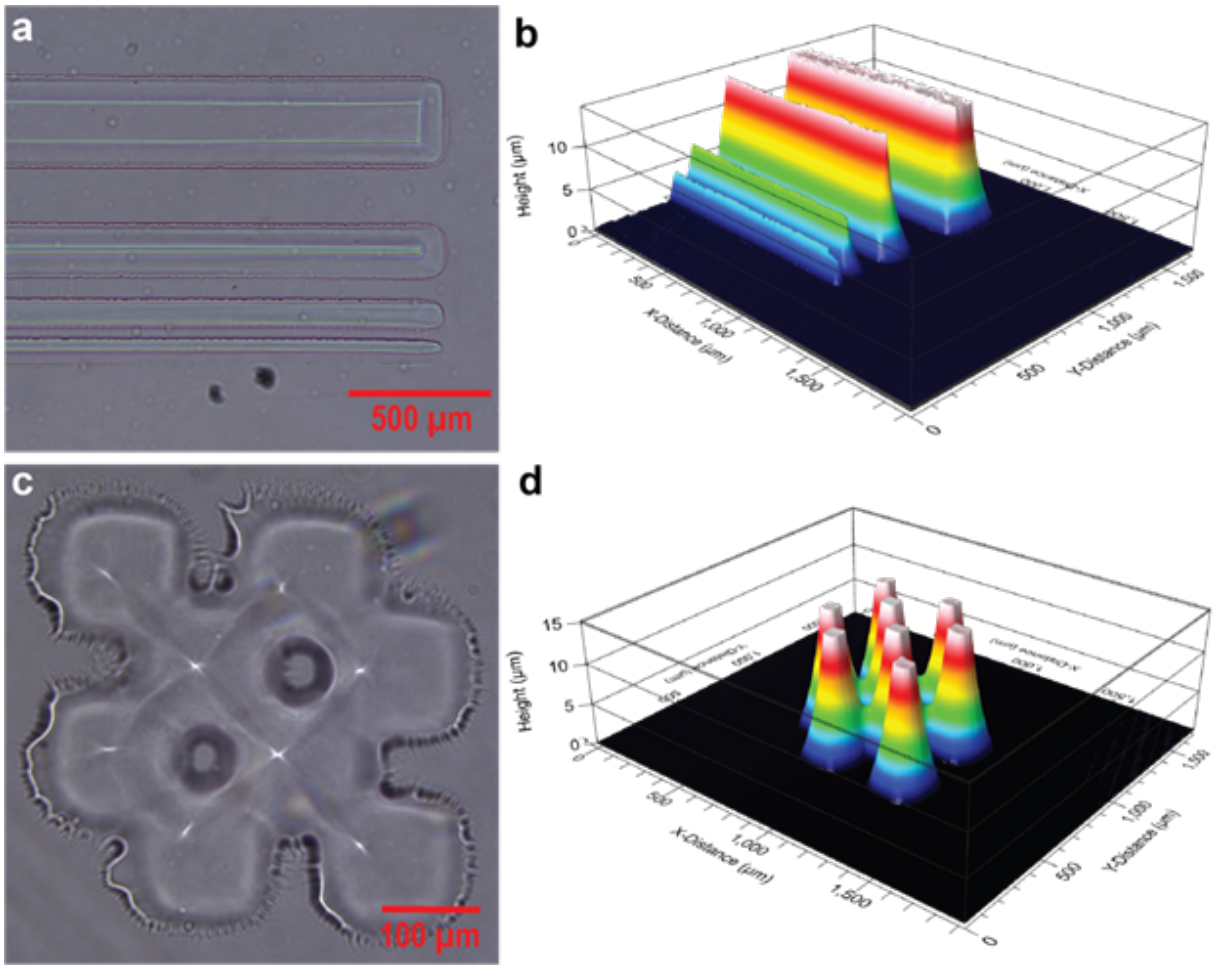

Figure D.9: Patterned Sylgard 184. Conditions: Standard photopatterning agent (4:0.5:0.5), spin-coated at 2000 rpm for 20 seconds, 6000 rpm for 10 seconds, 10-second exposure (11.7 mW/cm²), 140-second post-exposure bake, 30-second development in 50% ethyl acetate and 50% 2-propanol, followed by a 2-propanol rinse. (a) Optical microscope image of patterned lines. (b) 3D profile of the lines obtained using white light interferometry. (c) Optical microscope image of a checkerboard pattern. (d) 3D profile of the checkerboard pattern obtained using white light interferometry.

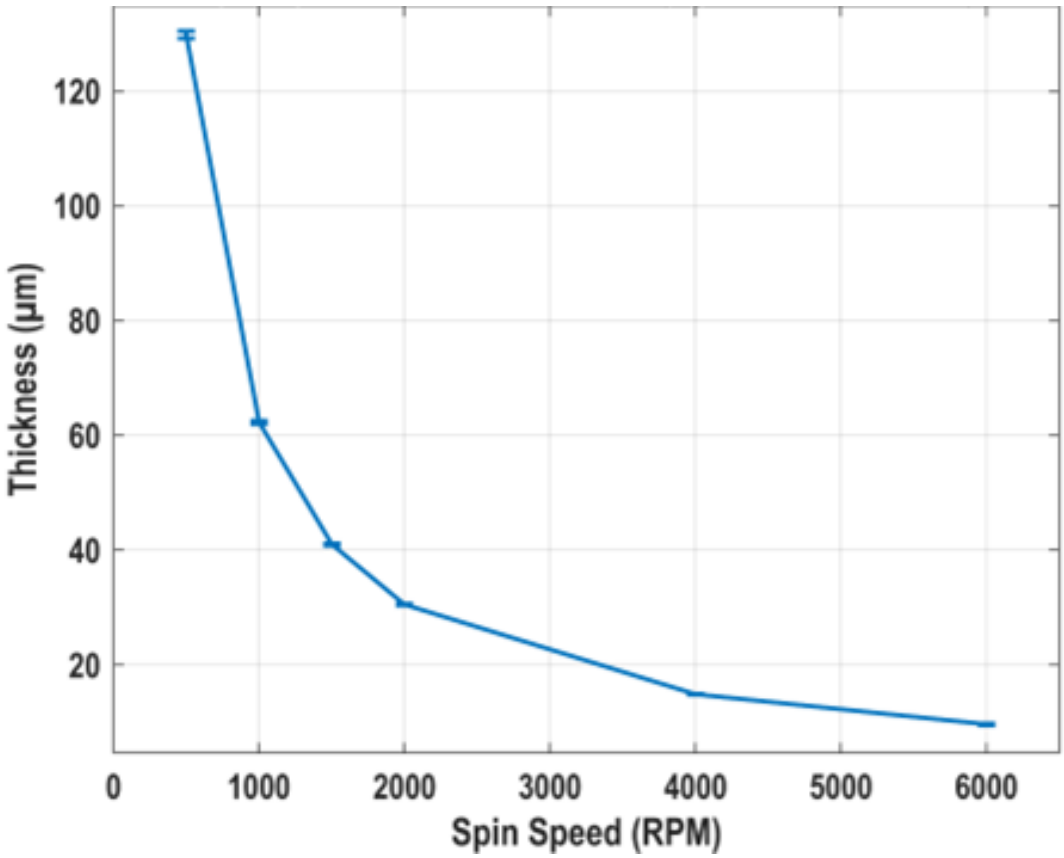

Figure D.10: Film thickness of Sylgard 184 mixed the 0.1 ml/g of the photopatterning agent. Thickness plotted as a function of spin speed for a duration of 40 seconds.

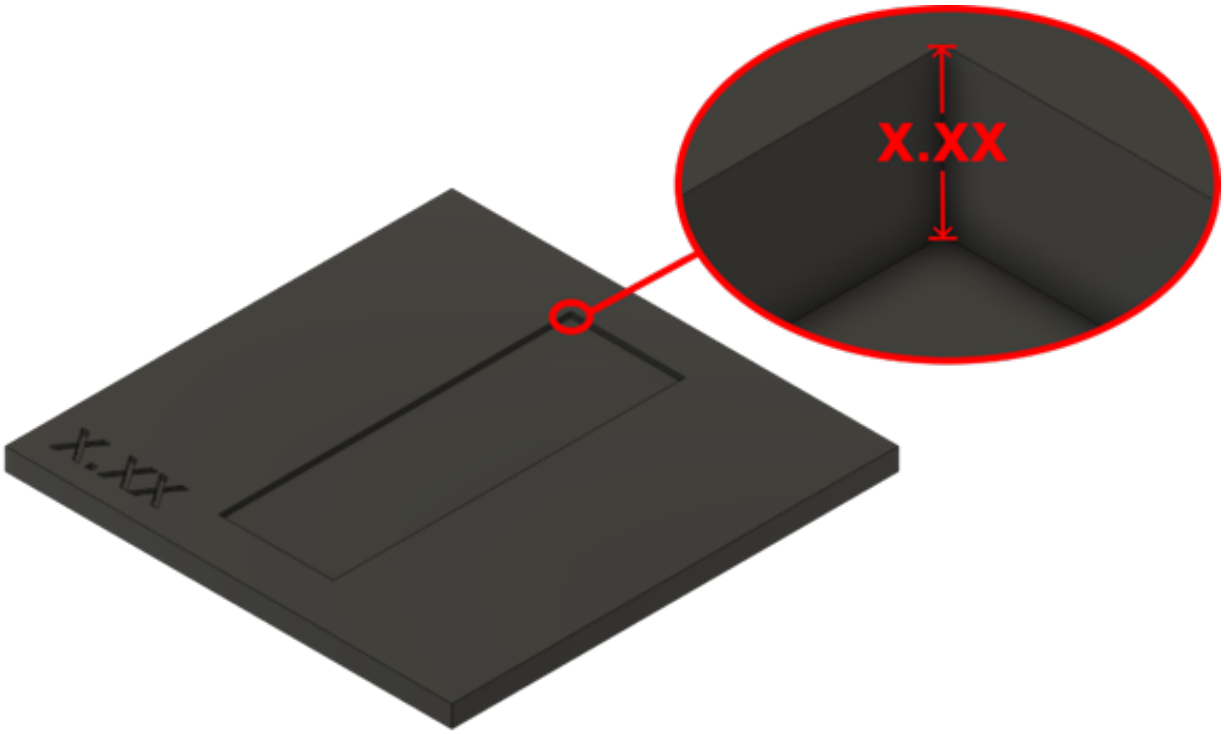

Figure D.11: Model of custom 3D-printed spacers featuring varying depths (X.XX), including 1.1, 1.15, 1.2, 1.25, 1.3, and 1.4 mm.

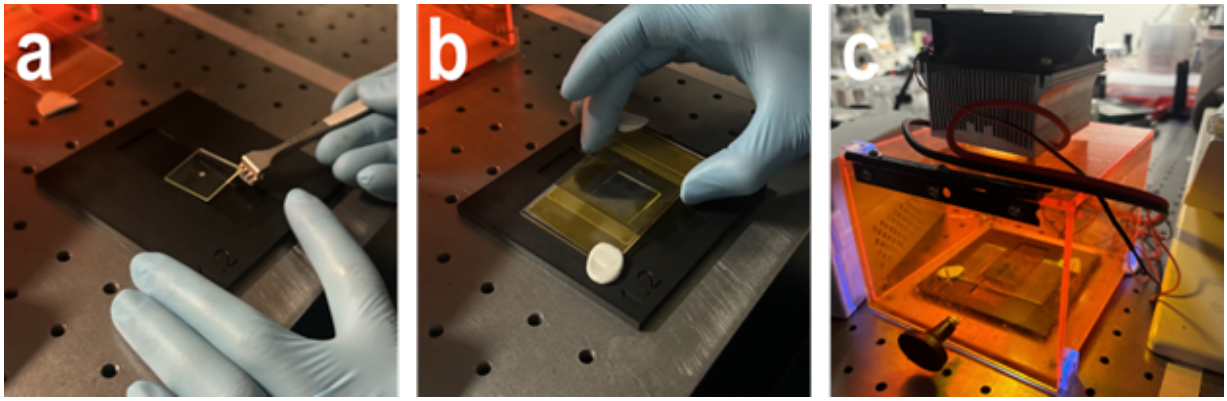

Figure D.12: A photomask from Fineline Imaging is taped to a 50 mm x 75 mm glass slide, ensuring that the mask is positioned closest to the film during patterning. The setup is layered with the photomask on the bottom, followed by the glass slide, and then the Kapton film on top. The Kapton film is cut to cover the regions outside the area of interest, leaving only the desired pattern exposed. a) Samples are placed onto the spacers. b) Mask is placed on top of the spacer. c) Samples undergoing UV exposure inside the custom-built UV exposure chamber.

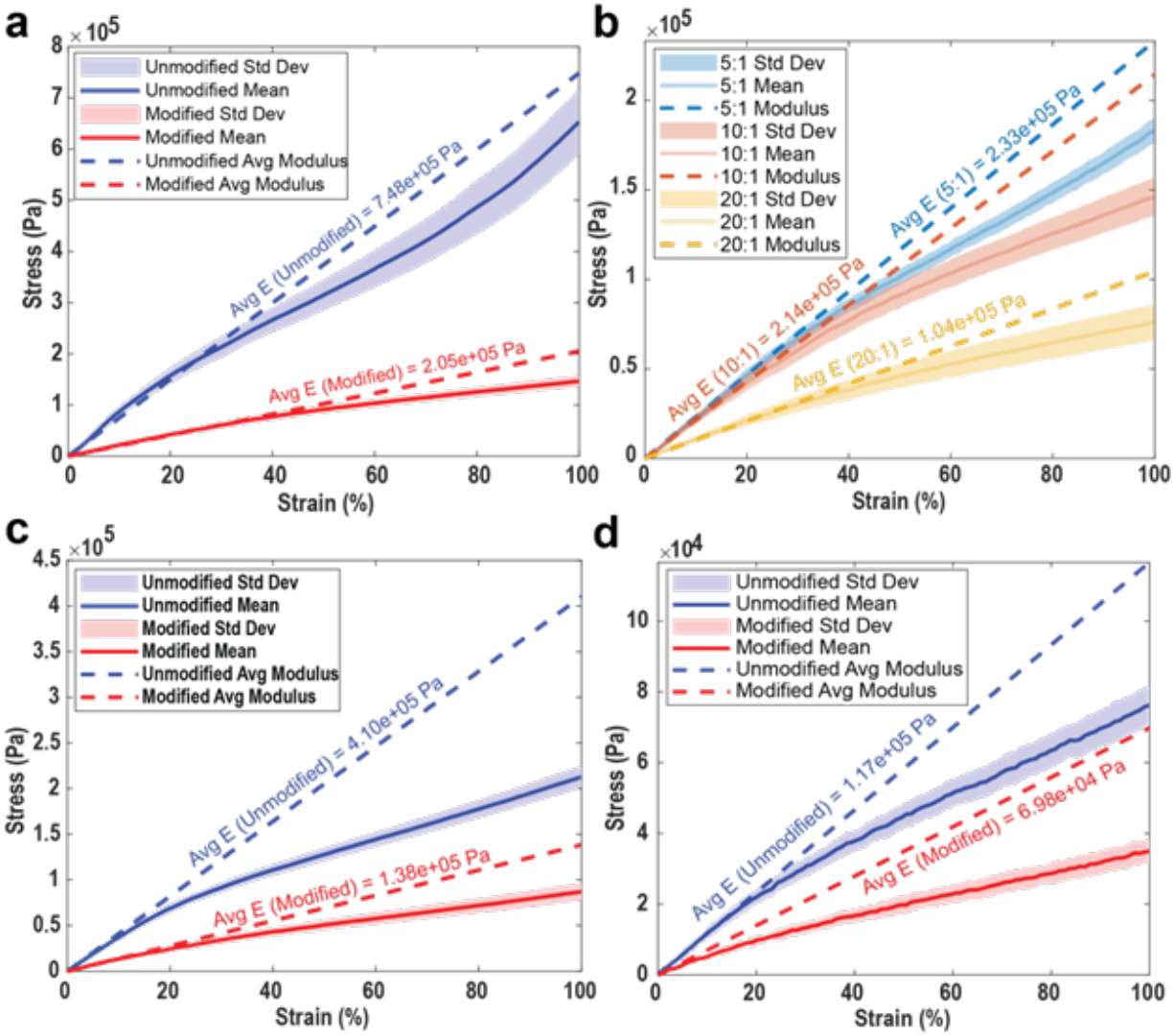

Figure D.13: Stress vs. strain data obtained through water-assisted tensile testing. Modified samples refer to those containing the photopatterning agent, while unmodified samples do not include the agent. (a) Stress vs. strain curves for Sylgard 184, comparing modified and unmodified samples to illustrate the effect of the photopatterning agent on mechanical properties. (b) Stress vs. strain curves for modified Sylgard 184 samples, showing the effect of varying base-to-crosslinker ratios on mechanical behavior and elasticity. (c) Stress vs. strain data for Dragon Skin 10 Medium, comparing modified and unmodified samples to assess the impact of the photopatterning agent on this silica-heavy formulation. (d) Stress vs. strain data for Ecoflex, highlighting the differences in mechanical performance between modified and unmodified samples, particularly in this softer silicone formulation.

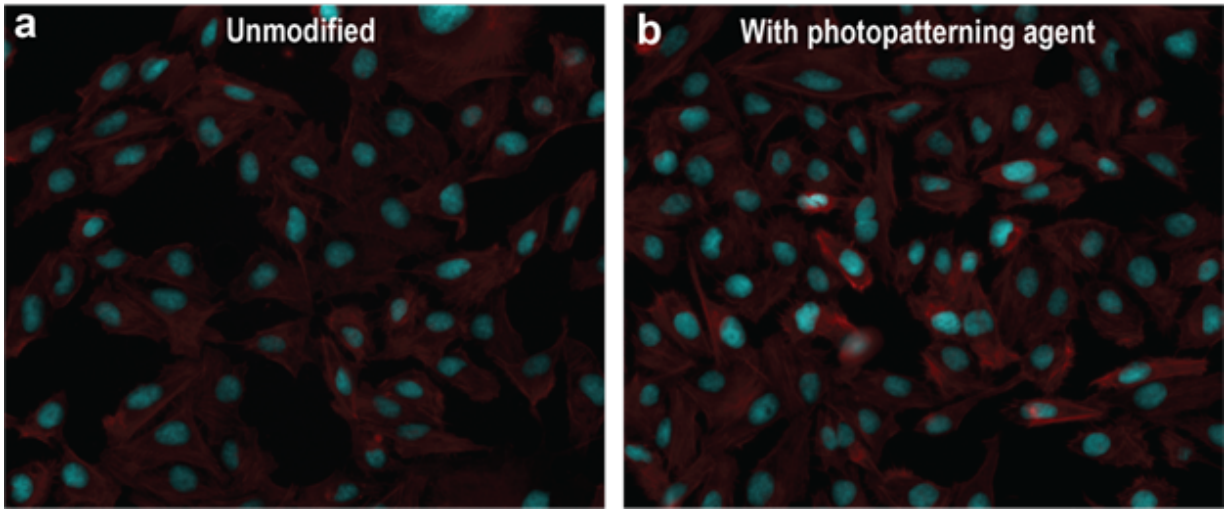

Figure D.14: Fluorescence images of stained U2OS cells grown on Sylgard 184 substrates to evaluate the biocompatibility of the photopatternable silicone formulation. Cells were fixed, permeabilized, and stained with DAPI to visualize nuclei (blue) and Alexa 594-phalloidin to highlight F-actin (red), indicating cell health and adherence. No significant differences in cell morphology, adhesion, or confluence were observed between the two substrates, supporting the biocompatibility of the photopatternable formulation. Images were acquired using an Echo Revolution microscope, with 20x PLAN Fluorite LWD CC Phase Ph1 NA 0.45 and 40x PLAN Fluorite LWD CC Phase Ph2 NA 0.60 objectives. (a) U2OS cells cultured on unmodified Sylgard 184 substrate; (b) U2OS cells cultured on photopatternable Sylgard 184 substrate.

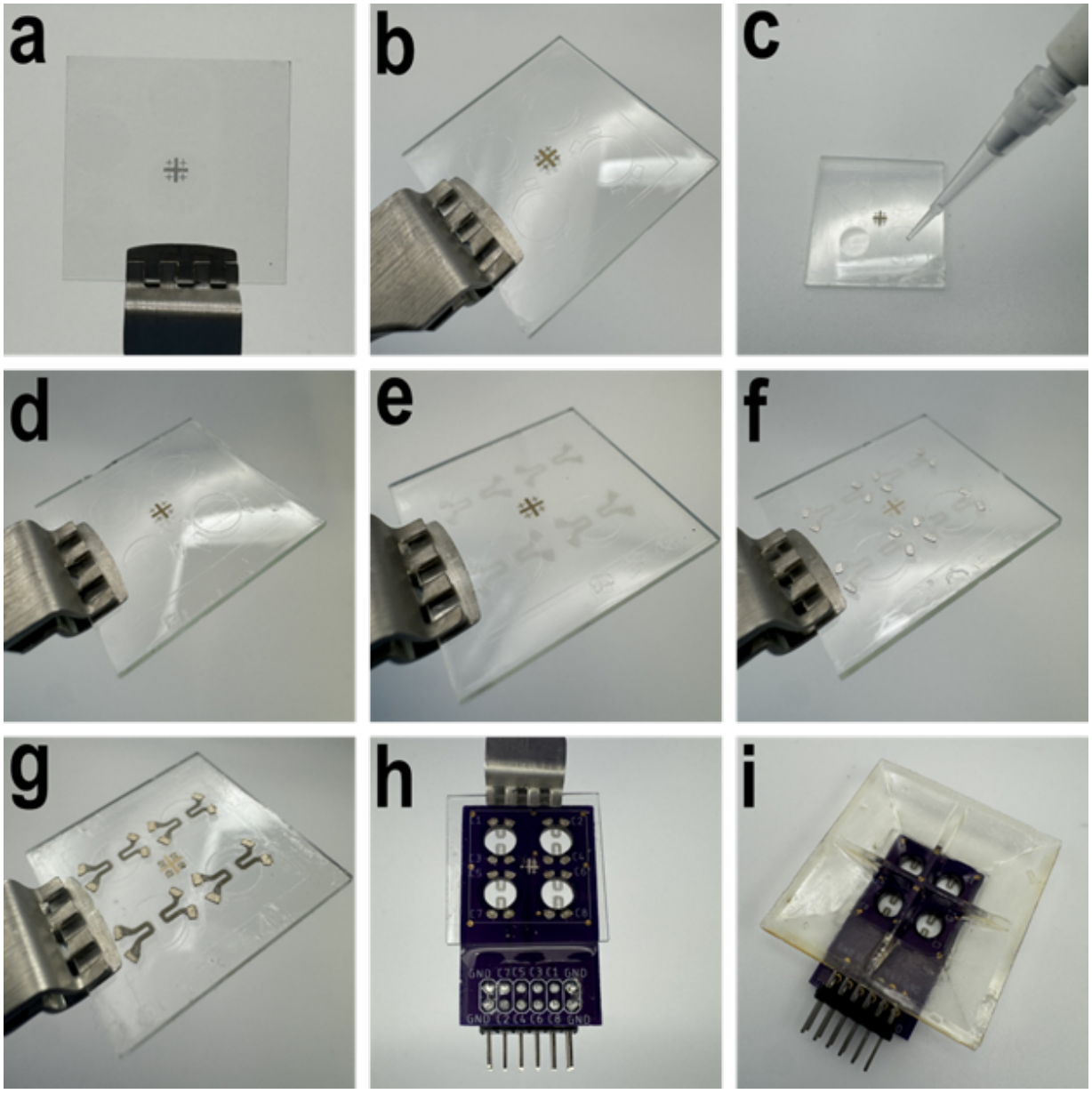

Figure D.15: Steps for fabrication of Cardiac Microphysiological Devices with Integrated Sensors. (a) Alignment marks created by spray-coating diluted silver paint onto glass slides with a shadow mask. (b) First photopatternable PDMS layer with patterned holes. (c) Dextran solution drop-cast into holes for release layer. (d) First cantilever layer applied. (e) Au-Ag nanowires spray-coated for sensor patterning. (f) Silver epoxy contacts added. (g) Second cantilever layer applied over sensors. This sample was different from the previous steps. (h) PCB attached for electronic integration. (i) Culture well secured to complete device.

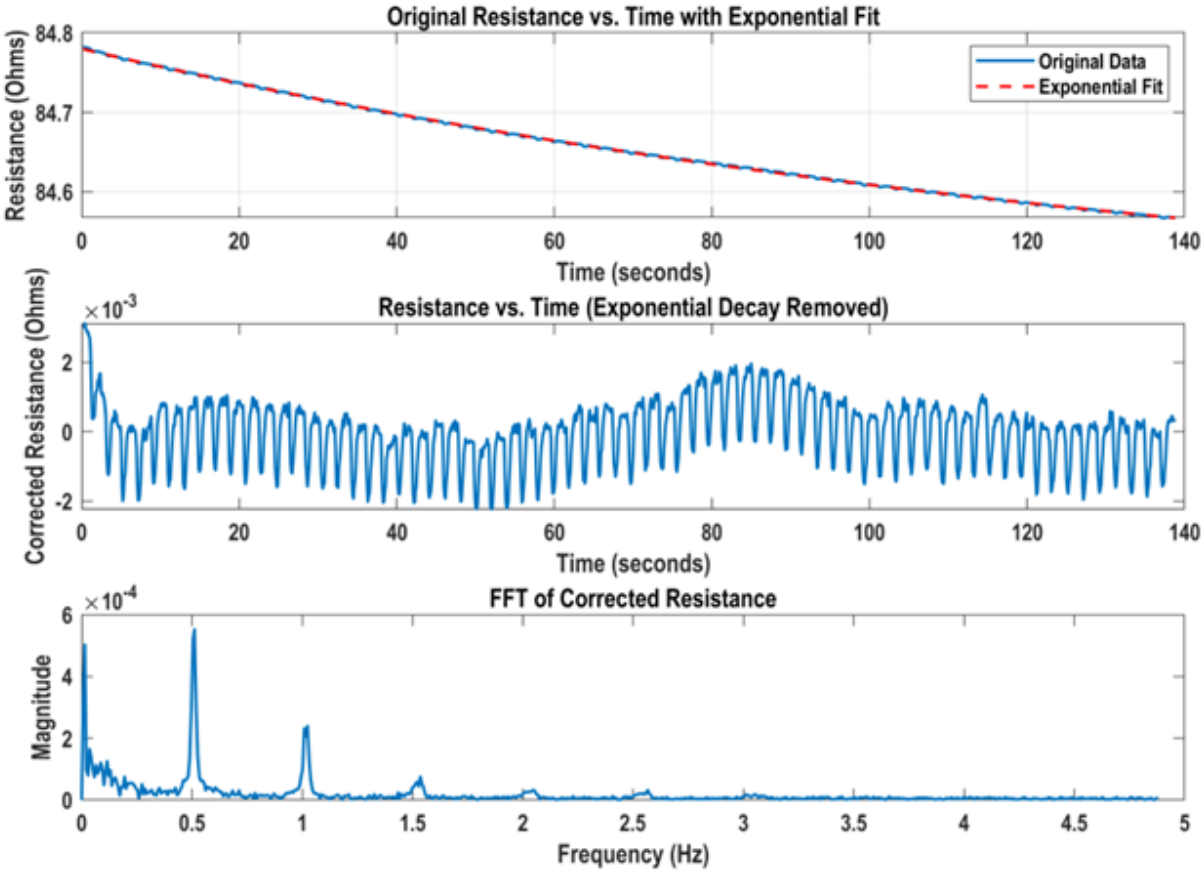

Figure D.16: Exponential decay removal and fast fourier transform of data before a bandpass filter from 0.2 Hz to 2 hz was applied.

Bibliography

[1] Wei Teng Neo, Qun Ye, Soo-Jin Chua, and Jianwei Xu. Conjugated polymer-based electrochromics: materials, device fabrication and application prospects. *Journal of Materials Chemistry C*, 4(31):7364–7376, 2016. Publisher: Royal Society of Chemistry.

[2] Jianjun Liao, Hewei Si, Xidong Zhang, and Shiwei Lin. Functional Sensing Interfaces of PEDOT:PSS Organic Electrochemical Transistors for Chemical and Biological Sensors: A Mini Review. *Sensors*, 19(2):218, January 2019. Number: 2 Publisher: Multidisciplinary Digital Publishing Institute.

[3] Yuanying Liang, Andreas Offenhäusser, Sven Ingebrandt, and Dirk Mayer. PEDOT:PSS-Based Bioelectronic Devices for Recording and Modulation of Electrophysiological and Biochemical Cell Signals. *Advanced Healthcare Materials*, 10(11):2100061, 2021. _eprint: https://onlinelibrary.wiley.com/doi/pdf/10.1002/adhm.202100061.

[4] Laure V. Kayser and Darren J. Lipomi. Stretchable Conductive Polymers and Composites Based on PEDOT and PEDOT:PSS. *Advanced Materials*, 31(10):1806133, 2019. _eprint: https://onlinelibrary.wiley.com/doi/pdf/10.1002/adma.201806133.

[5] Leon S. Van Dyke, Charles J. Brumlik, Charles R. Martin, Zengi Yu, and George J. Collins. UV laser ablation of electronically conductive polymers. *Synthetic Metals*, 52(3):299–304, October 1992.

[6] Masashi Nitani, Kengo Nakayama, Kazuki Maeda, Mariko Omori, and Mayumi Uno. Organic temperature sensors based on conductive polymers patterned by a selective-wetting method. *Organic Electronics*, 71:164–168, August 2019.

[7] Jong Seob Choi, Kuk Young Cho, and Jin-Heong Yim. Micro-patterning of vapor-phase polymerized poly(3,4-ethylenedioxythiophene) (PEDOT) using ink-jet printing/soft lithography. *European Polymer Journal*, 46(3):389–396, March 2010.

[8] Dabum Kim, Jeonghun Kim, Youngsang Ko, Kyubin Shim, Jung Ho Kim, and Jungmok You. A Facile Approach for Constructing Conductive Polymer Patterns for Application in Electrochromic Devices and Flexible Microelectrodes. *ACS Applied Materials & Interfaces*, 8(48):33175–33182, December 2016. Publisher: American Chemical Society.

[9] Shiming Zhang, Elizabeth Hubis, Gaia Tomasello, Guido Soliveri, Prajwal Kumar, and Fabio Cicoira. Patterning of Stretchable Organic Electrochemical Transistors. *Chemistry of Materials*, 29(7):3126–3132, April 2017. Publisher: American Chemical Society.

[10] Benoît Charlot, Gilbert Sassine, Alexandra Garraud, Brice Sorli, Alain Giani, and Philippe Combette. Micropatterning PEDOT:PSS layers. *Microsystem Technologies*, 19(6):895–903, June 2013.

[11] Steven A. Rutledge and Amr S. Helmy. Etch-Free Patterning of Poly(3,4-ethylenedioxythiophene)–Poly(styrenesulfonate) for Optoelectronics. *ACS Applied Materials & Interfaces*, 7(7):3940–3948, February 2015. Publisher: American Chemical Society.

[12] Jeonghun Kim, Jungmok You, and Eunkyoung Kim. Flexible Conductive Polymer Patterns from Vapor Polymerizable and Photo-Cross-Linkable EDOT. *Macromolecules*, 43(5):2322–2327, March 2010. Publisher: American Chemical Society.

[13] Jeonghun Kim, Yuna Kim, and Eunkyoung Kim. Electrochromic pattern formation by photo cross-linking reaction of PEDOT side chains. *Macromolecular Research*, 17(10):791–796, October 2009.

[14] Yevgeniya Kalachyova, Olga Guselnikova, Vladimir Hnatowicz, Pavel Postnikov, Vaclav Švorčík, and Oleksiy Lyutakov. Flexible Conductive Polymer Film Grafted with Azo-Moieties and Patterned by Light Illumination with Anisotropic Conductivity. *Polymers*, 11(11):1856, November 2019. Number: 11 Publisher: Multidisciplinary Digital Publishing Institute.

[15] Dan My Nguyen, Chun-Yuan Lo, Tianzheng Guo, Taewook Choi, Shalini Sundar, Zachary Swain, Yuhang Wu, Charles Dhong, and Laure V. Kayser. One Pot Photomediated Formation of Electrically Conductive Hydrogels. *ACS Polymers Au*, 4(1):34–44, February 2024. Publisher: American Chemical Society.

[16] Tokihiko Shimura, Shun Sato, Taizo Tominaga, Shuma Abe, Kaoru Yamashita, Minoru Ashizawa, Takeo Kato, Hiroki Ishikuro, and Naoji Matsuhisa. A High-Resolution, Transparent, and Stretchable Polymer Conductor for Wearable Sensor Arrays. *Advanced Materials Technologies*, 8(12):2201992, 2023. _eprint: https://onlinelibrary.wiley.com/doi/pdf/10.1002/admt.202201992.

[17] Mahima Bansal, Yukti Vyas, Zaid Aqrawe, Brad Raos, Ernest Cheah, Johanna Montgomery, Zimei Wu, and Darren Svirskis. Patternable Gelatin Methacrylate/PEDOT/Polystyrene Sulfonate Microelectrode Coatings for Neuronal Recording. *ACS Biomaterials Science & Engineering*, 8(9):3933–3943, September 2022. Publisher: American Chemical Society.

[18] Tae Geun Kim, Su Ryong Ha, Hyosung Choi, Kyungchan Uh, Umesha Kundapur, Sumin Park, Chan Woo Lee, Sang-hwa Lee, Jaeyong Kim, and Jong-Man Kim. Polymerizable

Supramolecular Approach to Highly Conductive PEDOT:PSS Patterns. *ACS Applied Materials & Interfaces*, 9(22):19231–19237, June 2017. Publisher: American Chemical Society.

[19] Zijie Zhu, Gaomai Yang, Ruya Li, and Tingrui Pan. Photopatternable PEDOT:PSS/PEG hybrid thin film with moisture stability and sensitivity. *Microsystems & Nanoengineering*, 3(1):1–9, April 2017. Number: 1 Publisher: Nature Publishing Group.

[20] Yuanwen Jiang, Zhitao Zhang, Yi-Xuan Wang, Deling Li, Charles-Théophile Coen, Ernie Hwaun, Gan Chen, Hung-Chin Wu, Donglai Zhong, Simiao Niu, Weichen Wang, Aref Saberi, Jian-Cheng Lai, Yilei Wu, Yang Wang, Artem A. Trotsyuk, Kang Yong Loh, Chien-Chung Shih, Wenhui Xu, Kui Liang, Kailiang Zhang, Yihong Bai, Gurupranav Gurusankar, Wenping Hu, Wang Jia, Zhen Cheng, Reinhold H. Dauskardt, Geoffrey C. Gurtner, Jeffrey B.-H. Tok, Karl Deisseroth, Ivan Soltesz, and Zhenan Bao. Topological supramolecular network enabled high-conductivity, stretchable organic bioelectronics. *Science*, 375(6587):1411–1417, March 2022. Publisher: American Association for the Advancement of Science.

[21] Bjørn Winther-Jensen and Keld West. Vapor-Phase Polymerization of 3,4-Ethylenedioxythiophene: A Route to Highly Conducting Polymer Surface Layers. *Macromolecules*, 37(12):4538–4543, June 2004. Publisher: American Chemical Society.

[22] Robert Brooke, Drew Evans, Maik Dienel, Pejman Hojati-Talemi, Peter Murphy, and Manrico Fabretto. Inkjet printing and vapor phase polymerization: patterned conductive PEDOT for electronic applications. *Journal of Materials Chemistry C*, 1(20):3353–3358, May 2013. Publisher: The Royal Society of Chemistry.

[23] Cathal D. O'Connell, Michael J. Higgins, Hiroshi Nakashima, Simon E. Moulton, and Gordon G. Wallace. Vapor Phase Polymerization of EDOT from Submicrometer Scale Oxidant Patterned by Dip-Pen Nanolithography. *Langmuir*, 28(26):9953–9960, July 2012. Publisher: American Chemical Society.

[24] Jesper Edberg, Donata Iandolo, Robert Brooke, Xianjie Liu, Chiara Musumeci, Jens Wenzel Andreasen, Daniel T. Simon, Drew Evans, Isak Engquist, and Magnus Berggren. Patterning and Conductivity Modulation of Conductive Polymers by UV Light Exposure. *Advanced Functional Materials*, 26(38):6950–6960, 2016. _eprint: https://onlinelibrary.wiley.com/doi/pdf/10.1002/adfm.201601794.

[25] Juan Chen and Wesley R. Browne. Photochemistry of iron complexes. *Coordination Chemistry Reviews*, 374:15–35, November 2018.

[26] Jozef Šima and Juliana Makáňová. Photochemistry of iron (III) complexes. *Coordination Chemistry Reviews*, 160:161–189, April 1997.

[27] Miguel I. Gonzalez, David Gygi, Yangzhong Qin, Qilei Zhu, Elizabeth J. Johnson, Yu-Sheng Chen, and Daniel G. Nocera. Taming the Chlorine Radical: Enforcing Steric Control

over Chlorine-Radical-Mediated C–H Activation. *Journal of the American Chemical Society*, 144(3):1464–1472, January 2022. Publisher: American Chemical Society.

[28] M. Lim, K. Chiang, and R. Amal. Photochemical synthesis of chlorine gas from iron(III) and chloride solution. *Journal of Photochemistry and Photobiology A: Chemistry*, 183(1):126–132, September 2006.

[29] Yabo Qi, Sha Luo, Wei Li, Shujun Li, Zhijun Chen, Bing Tian, and Shouxin Liu. Visible-light-initiated air-oxygenation of 5-hydroxymethylfurfural to maleic acid by iron(III) chloride. *Chemical Engineering Journal*, 487:150580, May 2024.

[30] Guoqiang Gao, Yi Deng, and Lowell D. Kispert. Photoactivated Ferric Chloride Oxidation of Carotenoids by Near-UV to Visible Light. *The Journal of Physical Chemistry B*, 101(39):7844–7849, September 1997. Publisher: American Chemical Society.

[31] Ken Takaki, Jun Yamamoto, Yuka Matsushita, Hirokazu Morii, Tetsuya Shishido, and Katsuomi Takehira. Oxidation of Alkanes with Dioxygen Induced by Visible Light and Cu(II) and Fe(III) Chlorides. *Bulletin of the Chemical Society of Japan*, 76(2):393–398, February 2003.

[32] Andrea Rogolino, José B. G. Filho, Lorena Fritsch, José D. Ardisson, Marcos A. R. da Silva, Gabriel Ali Atta Diab, Ingrid Fernandes Silva, Carlos André Ferreira Moraes, Moacir Rossi Forim, Matthias Bauer, Thomas D. Kühne, Markus Antonietti, and Ivo F. Teixeira. Direct Synthesis of Acetone by Aerobic Propane Oxidation Promoted by Photoactive Iron(III) Chloride under Mild Conditions. *ACS Catalysis*, 13(13):8662–8669, July 2023. Publisher: American Chemical Society.

[33] Zongnan Zhang, Guoxiang Zhang, Ni Xiong, Ting Xue, Junjie Zhang, Lu Bai, Qinyue Guo, and Rong Zeng. Oxidative -C–C Bond Cleavage of 2° and 3° Alcohols to Aromatic Acids with O2 at Room Temperature via Iron Photocatalysis. *Organic Letters*, 23(8):2915–2920, April 2021. Publisher: American Chemical Society.

[34] Yunhe Jin, Qingqing Zhang, Lifang Wang, Xinyao Wang, Changgong Meng, and Chunying Duan. Convenient C(sp 3)–H bond functionalisation of light alkanes and other compounds by iron photocatalysis. *Green Chemistry*, 23(18):6984–6989, 2021. Publisher: Royal Society of Chemistry.

[35] J. F. Rabek, L. Å Lindén, H. Kaczmarek, B. J. Qu, and W. F. Shi. Photodegradation of poly(ethylene oxide) and its coordination complexes with iron(III)chloride. *Polymer Degradation and Stability*, 37(1):33–40, January 1992.

[36] Mary J. Donahue, Ana Sanchez-Sanchez, Sahika Inal, Jing Qu, Roisin M. Owens, David Mecerreyes, George G. Malliaras, and David C. Martin. Tailoring PEDOT properties for applications in bioelectronics. *Materials Science and Engineering: R: Reports*, 140:100546, April 2020.

[37] Miriam Seiti, Antonella Giuri, Carola Esposito Corcione, and Eleonora Ferraris. Advancements in tailoring PEDOT: PSS properties for bioelectronic applications: A comprehensive review. *Biomaterials Advances*, 154:213655, November 2023.

[38] Christian Boehler, Felix Oberueber, Sabine Schlabach, Thomas Stieglitz, and Maria Asplund. Long-Term Stable Adhesion for Conducting Polymers in Biomedical Applications: IrOx and Nanostructured Platinum Solve the Chronic Challenge. *ACS Applied Materials & Interfaces*, 9(1):189–197, January 2017. Publisher: American Chemical Society.

[39] Bjorn Winther-Jensen, Orawan Winther-Jensen, Maria Forsyth, and Douglas R. MacFarlane. High Rates of Oxygen Reduction over a Vapor Phase–Polymerized PEDOT Electrode. *Science*, 321(5889):671–674, August 2008. Publisher: American Association for the Advancement of Science.

[40] Sonia Guzzo, Stefano Carli, Barbara Pavan, Alice Lunghi, Mauro Murgia, and Michele Bianchi. Evaluation of the In Vitro Biocompatibility of PEDOT:Nafion Coatings. *Nanomaterials*, 11(8):2022, August 2021. Number: 8 Publisher: Multidisciplinary Digital Publishing Institute.

[41] Joseph L. Carter, Catherine A. Kelly, and Mike J. Jenkins. Enhanced adhesion of PEDOT:PSS to substrates using polydopamine as a primer. *Polymer Journal*, 56(2):115–120, February 2024. Publisher: Nature Publishing Group.

[42] Liangqi Ouyang, Bin Wei, Chin-chen Kuo, Sheevangi Pathak, Brendan Farrell, and David C. Martin. Enhanced PEDOT adhesion on solid substrates with electrografted P(EDOT-NH2). *Science Advances*, 3(3):e1600448, March 2017. Publisher: American Association for the Advancement of Science.

[43] Bin Wei, Jinglin Liu, Liangqi Ouyang, Chin-Chen Kuo, and David C. Martin. Significant Enhancement of PEDOT Thin Film Adhesion to Inorganic Solid Substrates with EDOT-Acid. *ACS Applied Materials & Interfaces*, 7(28):15388–15394, July 2015. Publisher: American Chemical Society.

[44] Stefano Carli, Laura Casarin, Giacomo Bergamini, Stefano Caramori, and Carlo Alberto Bignozzi. Conductive PEDOT Covalently Bound to Transparent FTO Electrodes. *The Journal of Physical Chemistry C*, 118(30):16782–16790, July 2014. Publisher: American Chemical Society.

[45] Boxiao Li, Kenneth H. Skorenko, Haian Qiu, Jeffrey M. Mativetsky, Derek B. Dwyer, William E. Bernier, and Wayne E. Jones. Effects of interfacial modification for vapor phase polymerized PEDOT on glass substrate. *Synthetic Metals*, 260:116293, February 2020.

[46] S. G. Im, P. J. Yoo, P. T. Hammond, and K. K. Gleason. Grafted Conducting Polymer Films for Nano-patterning onto Various Organic and Inorganic Substrates by Oxidative Chemical Vapor Deposition. *Advanced Materials*, 19(19):2863–2867, 2007. _eprint: https://onlinelibrary.wiley.com/doi/pdf/10.1002/adma.200701170.

[47] Drew Evans, Manrico Fabretto, Mischa Mueller, Kamil Zuber, Robert Short, and Peter Murphy. Structure-directed growth of high conductivity PEDOT from liquid-like oxidant layers during vacuum vapor phase polymerization. *Journal of Materials Chemistry*, 22(30):14889–14895, 2012. Publisher: Royal Society of Chemistry.

[48] Fabio Juliá. Ligand-to-Metal Charge Transfer (LMCT) Photochemistry at 3d-Metal Complexes: An Emerging Tool for Sustainable Organic Synthesis. *ChemCatChem*, 14(19):e202200916, 2022. _eprint: https://onlinelibrary.wiley.com/doi/pdf/10.1002/cctc.202200916.

[49] Zongnan Zhang, Xinyang Li, Dezhong Zhou, Shujiang Ding, Minyan Wang, and Rong Zeng. Controllable C–H Alkylation of Polyethers via Iron Photocatalysis. *Journal of the American Chemical Society*, 145(13):7612–7620, April 2023. Publisher: American Chemical Society.

[50] Michael Mueller, Manrico Fabretto, Drew Evans, Pejman Hojati-Talemi, Cynthia Gruber, and Peter Murphy. Vacuum vapour phase polymerization of high conductivity PEDOT: Role of PEG-PPG-PEG, the origin of water, and choice of oxidant. *Polymer*, 53(11):2146–2151, May 2012.

[51] Dhiman Bhattacharyya, Rachel M. Howden, David C. Borrelli, and Karen K. Gleason. Vapor phase oxidative synthesis of conjugated polymers and applications. *Journal of Polymer Science Part B: Polymer Physics*, 50(19):1329–1351, 2012. _eprint: https://onlinelibrary.wiley.com/doi/pdf/10.1002/polb.23138.

[52] Rachel M. Howden, Elaine D. McVay, and Karen K. Gleason. oCVD poly(3,4-ethylenedioxythiophene) conductivity and lifetime enhancement via acid rinse dopant exchange. *Journal of Materials Chemistry A*, 1(4):1334–1340, 2013. Publisher: Royal Society of Chemistry.

[53] H. Kaczmarek and J. F. Rabek. Photoinitiated degradation of polymers by metal salts-recent developments. *Die Angewandte Makromolekulare Chemie*, 247(1):111–130, 1997. _eprint: https://onlinelibrary.wiley.com/doi/pdf/10.1002/apmc.1997.052470108.

[54] E. D. Owen and S. R. Brooks. A reversible photoreaction of iron(III) chloride in poly(vinyl chloride) film. *Polymer Photochemistry*, 6(1):21–30, January 1985.

[55] Jan F. Rabek, J. Lucki, B. J. Qu, and W. F. Shi. Coordination complexes between iron(III) chloride and polyether, polyester, and poly(ether ester). *Macromolecules*, 24(4):836–843, February 1991.

[56] Weihua Liu, Barbara Etschmann, Joël Brugger, Leone Spiccia, Garry Foran, and Brent McInnes. UV–Vis spectrophotometric and XAFS studies of ferric chloride complexes in hyper-saline LiCl solutions at 25–90 °C. *Chemical Geology*, 231(4):326–349, August 2006.

[57] T. V. Pokholok, N. I. Zaitseva, G. B. Pariiskii, and D. Ya. Toptygin. A comparative kinetic description of the photoreduction of ferric chloride and tetraethyl ammonium tetrachloroferrate additives in solid polymethylmethacrylate. *Polymer Science U.S.S.R.*, 24(2):378–387, January 1982.

[58] Sandrine Morlat and Jean-Luc Gardette. Phototransformation of water-soluble polymers. I: photo- and thermooxidation of poly(ethylene oxide) in solid state. *Polymer*, 42(14):6071–6079, June 2001.

[59] Maria Teresa Caccamo and Salvatore Magazù. Ethylene Glycol – Polyethylene Glycol (EG-PEG) Mixtures: Infrared Spectra Wavelet Cross-Correlation Analysis. *Applied Spectroscopy*, 71(3):401–409, March 2017. Publisher: SAGE Publications Ltd STM.

[60] T. V. Pokholok, N. I. Zaitseva, G. B. Pariysky, and D. Ya. Toptygin. Kinetics of processes accompanying photoreduction of chloride complexes of Fe3+ in solid polymers. *Polymer Photochemistry*, 2(6):429–445, November 1982.

[61] Dunbar P. Birnie. Rational solvent selection strategies to combat striation formation during spin coating of thin films. *Journal of Materials Research*, 16(4):1145–1154, April 2001.

[62] Shangzhi Chen, Stefano Rossi, Ravi Shanker, Giancarlo Cincotti, Sampath Gamage, Philipp Kühne, Vallery Stanishev, Isak Engquist, Magnus Berggren, Jesper Edberg, Vanya Darakchieva, and Magnus P. Jonsson. Tunable Structural Color Images by UV-Patterned Conducting Polymer Nanofilms on Metal Surfaces. *Advanced Materials*, 33(33):2102451, 2021. _eprint: https://onlinelibrary.wiley.com/doi/pdf/10.1002/adma.202102451.

[63] Kamil Zuber, Henry Shere, Junaiz Rehmen, Vivienne Wheaton, Manrico Fabretto, Peter J. Murphy, and Drew R. Evans. Influence of Postsynthesis Heat Treatment on Vapor-Phase-Polymerized Conductive Polymers. *ACS Omega*, 3(10):12679–12687, October 2018. Publisher: American Chemical Society.

[64] Yajie Yang, Luning Zhang, Shibin Li, Zhiming Wang, Jianhua Xu, Wenyao Yang, and Yadong Jiang. Vapor Phase Polymerization Deposition Conducting Polymer Nanocomposites on Porous Dielectric Surface as High Performance Electrode Materials. *Nano-Micro Letters*, 5(1):40–46, March 2013.

[65] Robert Brooke, Ioannis Petsagkourakis, Kosala Wijeratne, and Peter Andersson Ersman. Electrochromic Displays Manufactured by a Combination of Vapor Phase Polymerization and Screen Printing. *Advanced Materials Technologies*, 7(9):2200054, 2022. _eprint: https://onlinelibrary.wiley.com/doi/pdf/10.1002/admt.202200054.

[66] Robert Brooke, Jesper Edberg, Donata Iandolo, Magnus Berggren, Xavier Crispin, and Isak Engquist. Controlling the electrochromic properties of conductive polymers using UV-light. *Journal of Materials Chemistry C*, 6(17):4663–4670, May 2018. Publisher: The Royal Society of Chemistry.

[67] So-Yeon Lee, Kyung Ryoul Park, Sung-gyu Kang, Ji-Hoon Lee, Eun-chae Jeon, Cheol-Hwee Shim, Jae-Pyoung Ahn, Dong-Ik Kim, Heung Nam Han, Young-Chang Joo, Chang-soon Kim, and In-Suk Choi. Selective crack suppression during deformation in metal films on polymer substrates using electron beam irradiation. *Nature Communications*, 10(1):4454, October 2019. Number: 1 Publisher: Nature Publishing Group.

[68] Seungwan Kim, Joohyuk Kang, Injun Lee, Jinhyeong Jang, Chan Beum Park, Wonryung Lee, and Byeong-Soo Bae. An intrinsically stretchable multi-biochemical sensor for sweat analysis using photo-patternable ecoflex. *npj Flexible Electronics*, 7(1):1–9, July 2023. Publisher: Nature Publishing Group.

[69] Shuwen Chen, Zheng Qiao, Yan Niu, Joo Chuan Yeo, Yuanchao Liu, Jiaming Qi, Shicheng Fan, Xiaoyan Liu, Jee Yeon Lee, and Chwee Teck Lim. Wearable flexible microfluidic sensing technologies. *Nature Reviews Bioengineering*, 1(12):950–971, December 2023. Publisher: Nature Publishing Group.

[70] Jeffrey T. Borenstein, Gerard Cummins, Abhishek Dutta, Eyad Hamad, Michael Pycraft Hughes, Xingyu Jiang, Hyowon (Hugh) Lee, Kin Fong Lei, Xiaowu (Shirley) Tang, Yuanjin Zheng, and Jie Chen. Bionanotechnology and bioMEMS (BNM): state-of-the-art applications, opportunities, and challenges. *Lab on a Chip*, 23(23):4928–4949, 2023. Publisher: Royal Society of Chemistry.

[71] Congyi Wu, Jun Xu, Tian Zhang, Guoqiang Xin, Min Li, Youmin Rong, Guojun Zhang, and Yu Huang. Precision cutting of PDMS film with UV-nanosecond laser based on heat generation-diffusion regulation. *Optics & Laser Technology*, 145:107462, January 2022.

[72] Rick Helgason, Jino Fathy, and Yongjun Lai. The effect of laser cutting on the Young's modulus of Polydimethylsiloxane. *Journal of Micromanufacturing*, 6(1):60–65, May 2023. Publisher: SAGE Publications India.

[73] Younan Xia and George M. Whitesides. Soft Lithography. *Angewandte Chemie International Edition*, 37(5):550–575, 1998. _eprint: https://onlinelibrary.wiley.com/doi/pdf/10.1002/%28SICI%291521-3773%2819980316%2937%3A5%3C550%3A%3AAID-ANIE550%3E3.0.CO%3B2-G.

[74] Rebecca J. Jackman, David C. Duffy, Oksana Cherniavskaya, and George M. Whitesides. Using Elastomeric Membranes as Dry Resists and for Dry Lift-Off. *Langmuir*, 15(8):2973–2984, April 1999. Publisher: American Chemical Society.

[75] Michael A. Brook. Functional silicone oils and elastomers: new routes lead to new properties. *Chemical Communications*, 59(86):12813–12829, 2023. Publisher: Royal Society of Chemistry.

[76] Shaorui Gao, Wing-Tai Tung, Dexter Siu-Hong Wong, Liming Bian, and A. Ping Zhang. Direct optical micropatterning of poly(dimethylsiloxane) for microfluidic devices. *Journal of Micromechanics and Microengineering*, 28(9):095011, June 2018. Publisher: IOP Publishing.

[77] Uwe Müller, Annett Kunze, Christian Herzig, and Johann Weis. Photocrosslinking of Silicones. Part 13. Photoinduced Thiol-Ene Crosslinking of Modified Silicones. *Journal of Macromolecular Science, Part A*, 33(4):439–457, April 1996. Publisher: Taylor & Francis _eprint: https://doi.org/10.1080/10601329608010869.

[78] Yufei Wu, Jiangling Liu, Xiaojiao Jiao, Fei Cheng, Guoqiao Lai, and Xiongfa Yang. UV-Cured Transparent Flexible Silicone Materials with High Tensile Strength. *ACS Omega*, 5(11):6199–6206, March 2020. Publisher: American Chemical Society.

[79] Hongping Xiang, Xiaowei Wang, Zhirong Ou, Guanghong Lin, Jingfeng Yin, Zhu Liu, Lanyue Zhang, and Xiaoxuan Liu. UV-curable, 3D printable and biocompatible silicone elastomers. *Progress in Organic Coatings*, 137:105372, December 2019.

[80] Khai D. Q. Nguyen, William V. Megone, Dexu Kong, and Julien E. Gautrot. Ultrafast diffusion-controlled thiol–ene based crosslinking of silicone elastomers with tailored mechanical properties for biomedical applications. *Polymer Chemistry*, 7(33):5281–5293, 2016. Publisher: Royal Society of Chemistry.

[81] Bo Jiang, Xiangrong Shi, Tong Zhang, and Yudong Huang. Recent advances in UV/thermal curing silicone polymers. *Chemical Engineering Journal*, 435:134843, May 2022.

[82] Ruslan Yu Lukin, Aidar M. Kuchkaev, Aleksandr V. Sukhov, Giyjaz E. Bekmukhamedov, and Dmitry G. Yakhvarov. Platinum-Catalyzed Hydrosilylation in Polymer Chemistry. *Polymers*, 12(10):2174, October 2020. Number: 10 Publisher: Multidisciplinary Digital Publishing Institute.

[83] Ali Asgar S. Bhagat, Preetha Jothimuthu, and Ian Papautsky. Photodefinable polydimethylsiloxane (PDMS) for rapid lab-on-a-chip prototyping. *Lab on a Chip*, 7(9):1192–1197, 2007. Publisher: Royal Society of Chemistry.

[84] Arthur Stricher, Renaud G. Rinaldi, Guilherme Machado, Gregory Chagnon, Denis Favier, Laurent Chazeau, and François Ganachaud. Light-Induced Bulk Architecturation of PDMS Membranes. *Macromolecular Materials and Engineering*, 301(10):1151–1157, 2016. _eprint: https://onlinelibrary.wiley.com/doi/pdf/10.1002/mame.201600237.

[85] Arthur Stricher, Renaud G. Rinaldi, Laurent Chazeau, and François Ganachaud. Photopatterning of PDMS Films: Challenging the Reaction between Benzophenone and Silicone Functional Groups. *Materials*, 14(8):2027, January 2021. Number: 8 Publisher: Multidisciplinary Digital Publishing Institute.

[86] Preetha Jothimuthu, Andrew Carroll, Ali Asgar S. Bhagat, Gui Lin, James E. Mark, and Ian Papautsky. Photodefinable PDMS thin films for microfabrication applications. *Journal of Micromechanics and Microengineering*, 19(4):045024, March 2009.

[87] Timothy J. Drahnak. Radiation activated addition reaction, July 1985.

[88] Larry D. Boardman and Joel D. Oxman. Hydrosilation reaction utilizing a free radical photoinitiator, April 2000.

[89] Philipp Mueller. Highly transparent silicone mixtures that can be cross-linked by light, January 2015.

[90] Matthew David Butts. Irradiation-curable silicone compositions, photo-active platinum (IV) compounds, and method, October 2000.

[91] Andreas STEINMANN and Kim Bastian BEBENROTH. One-component, storage-stable, UV-crosslinkable organosiloxane composition, November 2021.

[92] Hironao c/o Shin-Etsu Chemical Co Ltd Fujiki and Takafumi Shin-Etsu Chemical Co Ltd Sakamoto. Photo-curable liquid silicone rubber compositions for templating mother molds, December 2002.

[93] Chad D. Mistele. Photocured silicone sealant having improved adhesion to plastic, June 2005.

[94] Alexei V. Radchenko and François Ganachaud. Photocatalyzed Hydrosilylation in Silicone Chemistry. *Industrial & Engineering Chemistry Research*, 61(23):7679–7698, June 2022. Publisher: American Chemical Society.

[95] Helena G. Lancaster, Joe C. Goodall, Samuel P. Douglas, Laura J. Ashfield, Simon B. Duckett, Robin N. Perutz, and Andrew S. Weller. Platinum(II) Phenylpyridyl Schiff Base Complexes as Latent, Photoactivated, Alkene Hydrosilylation Catalysts. *ACS Catalysis*, 14(10):7492–7505, May 2024. Publisher: American Chemical Society.

[96] Marco Sangermano, Sophie Marchi, Davide Ligorio, Patrick Meier, and Xavier Kornmann. UV-Induced Frontal Polymerization of a Pt-Catalyzed Hydrosilation Reaction. *Macromolecular Chemistry and Physics*, 214(8):943–947, 2013. _eprint: https://onlinelibrary.wiley.com/doi/pdf/10.1002/macp.201300004.

[97] T. Mayer, D. Burget, G. Mignani, and J. P. Fouassier. Photohydrosilylation reaction of silicone polymers. Platinum-based photocatalysts: Trimethyl(-dicarbonyl) platinum IV complexes. *Journal of Polymer Science Part A: Polymer Chemistry*, 34(15):3141–3146, 1996. _eprint: https://onlinelibrary.wiley.com/doi/pdf/10.1002/%28SICI%291099-0518%2819961115%2934%3A15%3C3141%3A%3AAID-POLA5%3E3.0.CO%3B2-%23.

[98] Lu Xi, Zhu Liu, Jiahui Su, Yiling Bei, Hongping Xiang, and Xiaoxuan Liu. UV-activated hydrosilylation of (Me-Cp)Pt(Me)3: Enhanced photocatalytic activity, polymerization kinetics, and photolithography. *Journal of Applied Polymer Science*, 136(47):48251, 2019. _eprint: https://onlinelibrary.wiley.com/doi/pdf/10.1002/app.48251.

[99] S. Marchi, M. Sangermano, P. Meier, and X. Kornmann. Visible light-activated hydrosilation reaction. *Journal of Photochemistry and Photobiology A: Chemistry*, 303-304:86–90, April 2015.

[100] Sophie Marchi, Marco Sangermano, Patrick Meier, and Xavier Kornmann. A Comparison of the Reactivity of Two Platinum Catalysts for Silicone Polymer Cross-Linking by UV-Activated Hydrosilation Reaction. *Macromolecular Reaction Engineering*, 9(4):360–365, 2015. _eprint: https://onlinelibrary.wiley.com/doi/pdf/10.1002/mren.201500005.

[101] Samuel J. Edmunds, Armando D. Urbina, Hannah E. Fishman, Yi Qie, Rafael A. Montalvo, Noel Sebastien D. Mallari, Marc N. Levy, Rachel Blau, Abdulhameed Abdal, Andrea M. Armani, Tse Nga Ng, Nathan A. Romero, and Darren J. Lipomi. Photography-Inspired Patterned Vapor Phase Polymerization of Conductive PEDOT on Rigid and Stretchable Substrates. *ACS Materials Letters*, 6(7):2738–2747, July 2024. Publisher: American Chemical Society.

[102] Wenfeng Wu, Xiangling He, Zaihui Fu, Yachun Liu, Yanlong Wang, Xinglang Gong, Xiaolin Deng, Haitao Wu, Yanhong Zou, Ningya Yu, and Dulin Yin. Metal chlorides-catalyzed selective oxidation of cyclohexane by molecular oxygen under visible light irradiation. *Journal of Catalysis*, 286:6–12, February 2012.

[103] Thibault Troadec, Sze-yin Tan, Christopher J. Wedge, Jonathan P. Rourke, Patrick R. Unwin, and Adrian B. Chaplin. One-Electron Oxidation of [M(PtBu3)2] (M=Pd, Pt): Isolation of Monomeric [Pd(PtBu3)2]+ and Redox-Promoted CH Bond Cyclometalation. *Angewandte Chemie International Edition*, 55(11):3754–3757, 2016. _eprint: https://onlinelibrary.wiley.com/doi/pdf/10.1002/anie.201511467.

[104] Morgan C. MacInnis, Jessica C. DeMott, Eva M. Zolnhofer, Jia Zhou, Karsten Meyer, Russell P. Hughes, and Oleg V. Ozerov. Cationic Two-Coordinate Complexes of Pd(I) and Pt(I) Have Longer Metal-Ligand Bonds Than Their Neutral Counterparts. *Chem*, 1(6):902–920, December 2016. Publisher: Elsevier.

[105] Vitaly V Pavlishchuk and Anthony W Addison. Conversion constants for redox potentials measured versus different reference electrodes in acetonitrile solutions at 25°C. *Inorganica Chimica Acta*, 298(1):97–102, January 2000.

[106] Peter B. Hitchcock, Michael F. Lappert, and Nicholas J. W. Warhurst. Synthesis and Structure of a rac-Tris(divinyldisiloxane) diplatinum(0) Complex and its Reaction with Maleic Anhydride. *Angewandte Chemie International Edition in English*, 30(4):438–440, 1991. _eprint: https://onlinelibrary.wiley.com/doi/pdf/10.1002/anie.199104381.

[107] D. A. de Vekki, V. N. Spevak, E. A. Kuchaev, and N. K. Skvortsov. Hydrosilylation of Siloxanes in the Presence of Pt(II) and Pt(IV) Complexes. *Russian Journal of General Chemistry*, 75(11):1757–1762, November 2005.

[108] Judith Stein, L. N. Lewis, Y. Gao, and R. A. Scott. In Situ Determination of the Active Catalyst in Hydrosilylation Reactions Using Highly Reactive Pt(0) Catalyst Precursors. *Journal of the American Chemical Society*, 121(15):3693–3703, April 1999. Publisher: American Chemical Society.

[109] Qiang Wu and Peng Hu. Photoinduced CO Bond Formation through CC Bond Cleavage of Alcohols by Suppressing Alcohol Oxidation. *Advanced Synthesis & Catalysis*, 366(7):1595–1605, 2024. _eprint: https://onlinelibrary.wiley.com/doi/pdf/10.1002/adsc.202301437.

[110] James C. Mitchener and Mark S. Wrighton. Photogeneration of very active homogeneous catalysts using laser light excitation of iron carbonyl precursors. *Journal of the American Chemical Society*, 103(4):975–977, February 1981.

[111] Suzanne C. Bart, Emil Lobkovsky, and Paul J. Chirik. Preparation and Molecular and Electronic Structures of Iron(0) Dinitrogen and Silane Complexes and Their Application to Catalytic Hydrogenation and Hydrosilation. *Journal of the American Chemical Society*, 126(42):13794–13807, October 2004. Publisher: American Chemical Society.

[112] Aaron M. Tondreau, Crisita Carmen Hojilla Atienza, Keith J. Weller, Susan A. Nye, Kenrick M. Lewis, Johannes G. P. Delis, and Paul J. Chirik. Iron Catalysts for Selective Anti-Markovnikov Alkene Hydrosilylation Using Tertiary Silanes. *Science*, 335(6068):567–570, February 2012. Publisher: American Association for the Advancement of Science.

[113] Jennifer V. Obligacion and Paul J. Chirik. Earth-abundant transition metal catalysts for alkene hydrosilylation and hydroboration. *Nature Reviews Chemistry*, 2(5):15–34, May 2018. Publisher: Nature Publishing Group.

[114] P. Somasundaran, Somil C. Mehta, and Parag Purohit. Silicone emulsions. *Advances in Colloid and Interface Science*, 128-130:103–109, December 2006.

[115] Fatemeh Goodarzi and Sohrab Zendehboudi. A Comprehensive Review on Emulsions and Emulsion Stability in Chemical and Energy Industries. *The Canadian Journal of Chemical Engineering*, 97(1):281–309, 2019. _eprint: https://onlinelibrary.wiley.com/doi/pdf/10.1002/cjce.23336.

[116] Chenwei Liu, Mingzhong Li, Rui Han, Jibin Li, and Chunting Liu. Rheology of Water-in-Oil Emulsions with Different Drop Sizes. *Journal of Dispersion Science and Technology*, 37(3):333–344, March 2016. Publisher: Taylor & Francis.

[117] Pingyun Chen and Thomas J. Meyer. Medium Effects on Charge Transfer in Metal Complexes. *Chemical Reviews*, 98(4):1439–1478, June 1998.

[118] Aslıhan Gökaltun, Young Bok (Abraham) Kang, Martin L. Yarmush, O. Berk Usta, and Ayse Asatekin. Simple Surface Modification of Poly(dimethylsiloxane) via Surface Segregating Smart Polymers for Biomicrofluidics. *Scientific Reports*, 9(1):7377, May 2019. Publisher: Nature Publishing Group.

[119] Carlos Matellan and Armando E. del Río Hernández. Engineering the cellular mechanical microenvironment – from bulk mechanics to the nanoscale. *Journal of Cell Science*, 132(9):jcs229013, April 2019.

[120] Robert J. Pelham and Yu-li Wang. Cell locomotion and focal adhesions are regulated by substrateflexibility. *Proceedings of the National Academy of Sciences*, 94(25):13661–13665, December 1997. Publisher: Proceedings of the National Academy of Sciences.

[121] Adam J. Engler, Shamik Sen, H. Lee Sweeney, and Dennis E. Discher. Matrix Elasticity Directs Stem Cell Lineage Specification. *Cell*, 126(4):677–689, August 2006. Publisher: Elsevier.

[122] Rachelle N. Palchesko, Ling Zhang, Yan Sun, and Adam W. Feinberg. Development of Polydimethylsiloxane Substrates with Tunable Elastic Modulus to Study Cell Mechanobiology in Muscle and Nerve. *PLOS ONE*, 7(12):e51499, December 2012. Publisher: Public Library of Science.

[123] Song Zhang, Luke A. Galuska, and Xiaodan Gu. Water-assisted mechanical testing of polymeric thin-films. *Journal of Polymer Science*, 60(7):1108–1129, 2022. _eprint: https://onlinelibrary.wiley.com/doi/pdf/10.1002/pol.20210281.

[124] Menake E. Piyasena and Steven W. Graves. The intersection of flow cytometry with microfluidics and microfabrication. *Lab on a Chip*, 14(6):1044–1059, 2014. Publisher: Royal Society of Chemistry.

[125] Wing-Fu Lai and Wing-Tak Wong. Property-Tuneable Microgels Fabricated by Using Flow-Focusing Microfluidic Geometry for Bioactive Agent Delivery. *Pharmaceutics*, 13(6):787, June 2021. Number: 6 Publisher: Multidisciplinary Digital Publishing Institute.

[126] Manu Prakash and Neil Gershenfeld. Microfluidic Bubble Logic. *Science*, 315(5813):832–835, February 2007. Publisher: American Association for the Advancement of Science.

[127] Einollah Sarikhani, Vrund Patel, Zhi Li, Dhivya Pushpa Meganathan, Keivan Rahmani, Leah Sadr, Ryan Hosseini, Diether Visda, Shivani Shukla, Hamed Naghsh-Nilchi, Adarsh Balaji, Gillian McMahon, Shaoming Chen, Johannes Schöneberg, Colleen A. McHugh, Lingyan Shi, and Zeinab Jahed. Engineered Nanotopographies Induce Transient Openings in the Nuclear Membrane. *Advanced Functional Materials*, n/a(n/a):2410035. _eprint: https://onlinelibrary.wiley.com/doi/pdf/10.1002/adfm.202410035.

[128] DR Murdoch C Berry, JJV McMurray. Economics of chronic heart failure. *Eur. J. Heart Fail*, 3:283–291, 2001.

[129] W Dou. A microdevice platform for characterizing the effect of mechanical strain magnitudes on the maturation of iPSC-Cardiomyocytes. *Biosens. Bioelectron.*, 175:112875, 2021.

[130] Juan C. del Álamo, Derek Lemons, Ricardo Serrano, Alex Savchenko, Fabio Cerignoli, Rolf Bodmer, and Mark Mercola. High throughput physiological screening of iPSC-derived cardiomyocytes for drug development. *Biochimica et Biophysica Acta - Molecular Cell Research*, 1863(7):1717–1727, July 2016. Publisher: Elsevier B.V.

[131] Gordana Vunjak-Novakovic, Kacey Ronaldson-Bouchard, and Milica Radisic. Organs-on-a-chip models for biological research. *Cell*, 184(18):4597–4611, September 2021. Publisher: Elsevier.

[132] Johan U. Lind, Moran Yadid, Ian Perkins, Blakely B. O'Connor, Feyisayo Eweje, Christophe O. Chantre, Matthew A. Hemphill, Hongyan Yuan, Patrick H. Campbell, Joost J. Vlassak, and Kevin K. Parker. Cardiac microphysiological devices with flexible thin-film sensors for higher-throughput drug screening. *Lab on a Chip*, 17(21):3692–3703, October 2017. Publisher: The Royal Society of Chemistry.

[133] JU Lind. Instrumented cardiac microphysiological devices via multimaterial three-dimensional printing. *Nat. Mater.*, 16:303–308, 2017.

[134] Wenkun Dou, Manpreet Malhi, Qili Zhao, Li Wang, Zongjie Huang, Junhui Law, Na Liu, Craig A Simmons, Jason T Maynes, and Yu Sun. Microengineered platforms for characterizing the contractile function of in vitro cardiac models. 2014.

[135] Dong Su Kim, Yong Whan Choi, Arunkumar Shanmugasundaram, Yun Jin Jeong, Jongsung Park, Nomin Erdene Oyunbaatar, Eung Sam Kim, Mansoo Choi, and Dong Weon Lee. Highly durable crack sensor integrated with silicone rubber cantilever for measuring cardiac contractility. *Nature Communications 2020 11:1*, 11(1):1–13, January 2020. Publisher: Nature Publishing Group.

[136] Adam W. Feinberg, Alex Feigel, Sergey S. Shevkoplyas, Sean Sheehy, George M. Whitesides, and Kevin Kit Parker. Muscular Thin Films for Building Actuators and Powering Devices. *Science*, 317(5843):1366–1370, September 2007. Publisher: American Association for the Advancement of Science.

[137] Anna Grosberg, Patrick W. Alford, Megan L. McCain, and Kevin Kit Parker. Ensembles of engineered cardiac tissues for physiological and pharmacological study: Heart on a chip. *Lab on a Chip*, 11(24):4165–4173, November 2011. Publisher: The Royal Society of Chemistry.

[138] Megan L. McCain, Ashutosh Agarwal, Haley W. Nesmith, Alexander P. Nesmith, and Kevin Kit Parker. Micromolded gelatin hydrogels for extended culture of engineered cardiac tissues. *Biomaterials*, 35(21):5462–5471, July 2014. Publisher: Elsevier.

[139] Y. Dai, N. E. Oyunbaatar, B. K. Lee, E. S. Kim, and D. W. Lee. Spiral-shaped SU-8 cantilevers for monitoring mechanical response of cardiomyocytes treated with cardiac drugs. *Sensors and Actuators B: Chemical*, 255:3391–3399, February 2018. Publisher: Elsevier.

[140] Matteo Parente, Max van Helvert, Ruben F. Hamans, Ruth Verbroekken, Rochan Sinha, Anja Bieberle-Hütter, and Andrea Baldi. Simple and Fast High-Yield Synthesis of Silver Nanowires. *Nano Letters*, 20(8):5759–5764, August 2020. Publisher: American Chemical Society.

[141] Miaoxin Yang, Zachary D. Hood, Xuan Yang, Miaofang Chi, and Younan Xia. Facile synthesis of Ag@Au core–sheath nanowires with greatly improved stability against oxidation. *Chemical Communications*, 53(12):1965–1968, February 2017. Publisher: The Royal Society of Chemistry.